UiO : Department of Mathematics
University of Oslo

Non-Intrusive Experimental Investigation of Flow in Complex Aneurysmal Geometries

Vetle Christoffer Frostelid

Master's Thesis, Spring 2016

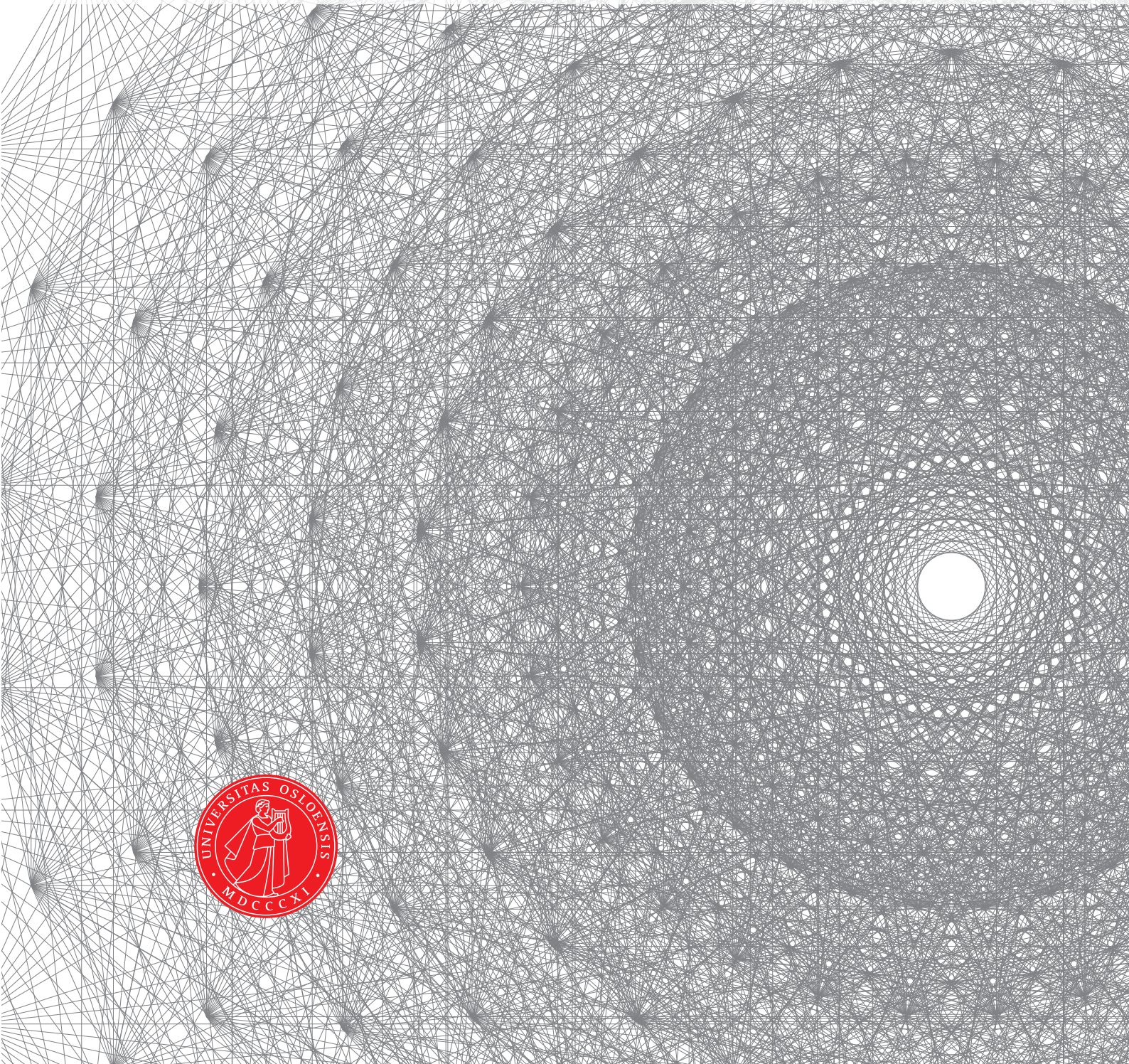

Abstract

Two non-intrusive experimental methods were applied to steady flow through two 3D-printed, physiological cerebral aneurysm geometries for the purpose of investigating inceptive transitional behaviour, and general description of flow patterns. The first method used a contact microphone to measure pressure fluctuations on the outer model walls. Power spectrum densities (PSDs) of the acquired signals were estimated using Welch's method and the magnitude of the PSDs compared for various parent artery Reynolds numbers (Re). Fluctuations clearly appeared at Re$\sim$400$\pm$10% for model A, whereas model B saw a later transition at Re$\sim$700$\pm$10%, supporting the notion that flow fluctuations may occur at physiological parent artery Reynolds numbers for cerebral aneurysms ($<$500), but are aneurysm specific. Mechanotransductional effects of fluctuating flows therefore likely need to be investigated comprehensively in order to understand how the haemodynamics within affect the pathophysiology of aneurysms, in addition to the purely mechanical effects on the vessel walls. The PSDs were also used for estimation of the Kolmogorov time and length scales, τ and η, and turbulent kinetic energy dissipation rate, ε. For model A: $\tau \approx 1 \times 10^{-3} s$, $\eta \approx 31\ \mu m$ and $\varepsilon \approx 1\ J/(s \cdot kg)$. For model B: $\tau \approx 1.3 \times 10^{-3} s$, $\eta \approx 63\ \mu m$ and $\varepsilon \approx 0.64\ J/(s \cdot kg)$. Model B therefore displayed a lower dissipation rate, despite the smaller characteristic length scale, implying a comparatively larger reduction in the fluctuation velocities within the aneurysm sac. This was supported by the second measurement method, which combined stereographic x-ray radiography with particle tracking velocimetry (XPTV) in order to determine Lagrangian velocities and accelerations of the flow. Both models displayed a significant reduction in flow velocity within the aneurysm sac, however model B displayed further deceleration prior to the aneurysm location due to a bifurcation in the parent artery, which resulted in lower velocities and a slower deceleration overall. This offered part of a possible explanation for the comparatively less chaotic flow patterns observed in model B versus model A. Model A displayed a jet like flow pattern, known to have a lower critical Reynolds number than conventional cylindrical pipe flows. Overall, using the parent artery Reynolds number in order to justify a laminar assumption in numerical simulations appears far from ideal, as it potentially omits important aspects of the flow. Vortices were observed within the aneurysms, particularly for model A, and appeared to be highly localised. Suggestions for future improvements and investigations have been outlined, along with general background theory.

Acknowledgements

Thank you to my supervisors, Atle Jensen and Kent-Andre Mardal, for providing an interesting thesis topic and their guidance. Thank you also to Olav Gundersen for all his help in the lab, and to everyone that played a part in developing the equipment used, allowing for the completion of this thesis.

Short thesis (30 ECTS credits/ 1 semester) for the degree of Master of Computational Science and Engineering (Master i anvendt matematikk og mekanikk-ANMAT5930)

Contents

List of Figures

List of Tables

Chapter 1

Introduction

Hot-wire anemometry, optical particle image/tracking velocimetry (PIV/PTV) and other common flow measurement techniques are often either intrusive, or require full, undistorted optical access. A wide variety of flows exist, such as multiphase and biomedical flows, in which either of these conditions are unobtainable or inconvenient, and traditional flow measurement methods fall short. This thesis therefore focuses on the use and continued development of two non-intrusive and lesser used measurement methods; one in which flow-generated sounds/pressure fluctuations are measured acoustically, and one in which stereographic x-ray imaging is used for the purpose of three dimensional PTV analysis (XPTV). The methods have been applied to flows within complex geometries, specifically three dimensional aneurysm models. Aneurysms are a common vascular pathology with potentially fatal consequences and significant research is therefore being performed on the topic. In particular, understanding the pathophysiology is of importance, and part of this includes an understanding of the haemodynamics within. Computational fluid dynamics (CFD) is increasingly used to model blood flow through aneurysms, with the ultimate goal being the development of risk assessment and predictive tools which will improve treatment and patient management. However, CFD results often depend on choice of numerical methods and underlying assumptions. One particular topic of controversy is that of the presence of turbulence, specifically in intracranial aneurysms, as simulations are often performed with a laminar presumption. Ultimately, experimental data is therefore necessary for improved validation of numerical solutions. One of the main purposes of the investigations reported in this thesis is therefore to determine when transitional flow behaviour emerges in the models studied, using experimental techniques. This may include inceptive flow separation and vortex formation, vortex shedding, or possibly more transitional and developed turbulent flows.

1.1 Related Research

A comparison will be made between the results obtained from the two methods, as well as with direct numerical simulations (DNS) and CFD simulations previously performed on the same models [31, 83]. The aneurysm models were 3D-printed based on real anatomical geometries obtained through medical imaging, and represent a potentially quick and cost efficient way of improving experimental measurement of flow in aneurysms, as previous experimental results have often been based on

idealised glass or silicone models or required access to real blood vessels [62, 30]. Several CFD investigations have successfully classified aneurysms according to rupture status retrospectively, however these studies have often assumed a laminar flow based on the low (<500) parent artery Reynolds number (Re). Jain et al.'s direct numerical simulations were performed in order to resolve the microscales required to pick up potential transitional behaviour, and resulted in aneurysm-specific flow fluctuations being observed as low as Re=250. Few CFD investigations have been coupled with experimental data. In one case, 2D-PIV was used on anatomically realistic silicone elastomer aneurysm models [22], however arguments are made that 3D measurements are required in order to calculate key parameters of the blood flow. A three dimensional fluorescent scanning stereoscopic particle image velocimetry method was therefore applied to a patient-specific, full-scale silicone rubber replica of a cerebral aneurysm by Yagi et al. and found evidence of fluctuating flows at low, physiological Reynolds numbers [91].

Blood flow has been measured acoustically for clinical purposes since the auscultatory method was developed as a way of measuring blood pressure in 1905 [37]. Furthermore, bruits and murmurs are known to be sounds associated with vascular diseases such as atherosclerosis, thrombosis and aneurysms, and are frequently used by physicians as a means of discovery of these ailments [10, 14, 64]. Sounds generated in the heart have been the subject of more advanced investigation, and the phonocardiogram has become a diagnostic tool based on high fidelity recording of murmurs made by the heart. Spectral analysis has been used to detect anomalous sounds, for identification of valvular disorders, and determination of pulmonary arterial pressure [13, 47, 89]. The analysis of sound is therefore a proven, non-intrusive tool, with many potential applications based on acoustical measurements of physical phenomena.

The mentioned flow-generated, biological sounds are commonly thought to be a product of turbulent blood flow, however the precise biomechanical source mechanism is not yet fully and conclusively understood. Alternate theories for sound generation have been hypothesised, most notably including pressure variations caused by periodic vortex shedding, and resonant vibrations in the viscoelastic blood vessel walls [70, 4]. The former theory was based on bruit formation in a stenosed artery, and the latter based on Korotkoff sound generation for the auscultatory method, and it is therefore important to keep in mind that although arterial sounds are generally similar, the underlying mechanics behind the sound generation may be different. Care must therefore be taken when analysing acoustic measurements, as it is difficult to determine whether the measured vibrations are a sign of flow features such as flow separation, vortex shedding, or more developed turbulence, or vibrations caused by movement of surrounding tissue, which may be more related to larger pressure differences caused by the pulsatile nature of blood flow. None the less, it is well known that non-pulsatile turbulent flows produce noise/vibrations, and amongst other findings, the sound spectrum of turbulent flow in a pipe has been investigated and compared with spectra of blood flow in narrowed arteries, in a technique referred to as phonoangiography, and found to be similar [41]. When the creation of a bruit in a stenosed artery was modelled by Seo et al., bruit creation was attributed to vortex motions as they directly affected the time-derivative of the integrated pressure force on the vessel wall, yet it was maintained that turbulence had little effect [70]. This may be seen as counter-intuitive, as vortices are an impor-

tant characteristic of turbulence. However, in this case vortices were formed due to vortex shedding behind the stenosis which occurred with a frequency and amplitude different to that of the observed turbulent parts of the flow. Accurate description of the flow within the geometry studied is therefore important in order to avoid incorrect conclusions in regards to sound/vibration generation.

Bruits and murmurs have understandably received significant attention as they lie in the audible spectrum, however this focus is potentially misleading, as the presence of flow fluctuations which are inaudible because of frequency mismatch, attenuation or other reasons may still have a significant biological effect. This is known as mechanotransduction, in which mechanical stimulation is translated into chemical signals. Turbulence has been shown to be especially important in the human body as it elicits a reaction by the vascular endothelial cells to a much greater extent than laminar flows, even at smaller magnitudes of wall shear stress, resulting in induced endothelial cell turnover, which in terms leads to effects such as atherosclerosis [17]. A theory that can help explain and model this has been put forth stating that the total dissipated energy is more important than the bulk shear energy when it comes to dictating the mechanical environment of blood cells. As the energy dissipation in fluctuating flows is greater than in laminar flows, turbulence leads to greater biological activity [55]. Nevertheless, the wall shear stress in itself is also important in many cases, and Bluestein et al. showed that wall shear stresses were decreased in recirculation zones within aneurysms, and that turbulence decreased the size of these zones, thus effectively increasing the wall shear stresses and increasing the chance of rupture [9]. Conversely, it has also been argued that stagnant flows are detrimental to vessel health, and there is some disagreement between the high-flow and low-flow effect schools of thought when it comes to the pathophysiolgy of cardiovascular diseases [71]. The uniform wall shear stress (WSS) hypothesis states that the arterial system attempts to adapt vessel radius to ensure the flow has an average uniform WSS of roughly 5 Pa [24]. This has been shown to apply to most parts of the cardiovascular system, however areas with complex geometries and lots of bifurcations may deviate, as is the case for the circle of Willis in the brain; a common site for aneurysms. Understanding the exact biological effect the flow has is therefore difficult, but the first step is necessarily identifying the nature of the flow in question, as is the focus of this thesis.

Acoustic sensors are theoretically sensitive enough to pick up on inaudible sounds, however, it is as mentioned difficult to conclusively determine the cause of the measured signal when the sensor is placed non-intrusively. This issue can be countered by the use of other measurements methods, such as the stereographic x-ray PTV technique used in this thesis, which allows for velocity measurements and flow visualisation, and a coinciding analysis of sound generation and flow patterns. X-rays have been used extensively for medical imaging in the past century, but have only recently been applied to dynamic flows. New imaging techniques, particularly for *in-vivo* imaging, are being researched actively [23]. PTV and PIV are well-established experimental techniques, however PTV was only coupled with x-ray imaging in 2001 [69]. Since then the technique has seen continued development, but has been limited by cost and resolution in space and time, which hinders the techniques ability to pick up on small fluctuations. Technological advancements have steadily improved on these limitations, which has allowed for increased application of x-ray imaging for the purpose of flow measurement. PIV and PTV analysis based on x-ray imaging

has specifically been used for investigation of multiphase flows [28, 54] and blood flow [32, 58, 3], and highlights the method's non-intrusive nature and independence from optical access.

Chapter 2

Background Theory

2.1 Aneurysms

The human cardiovascular system supplies tissues with blood, allowing for the transport and exchange of nutrients, metabolic waste, hormones, oxygen and carbon dioxide throughout the body. Alongside approximately 5 litres of blood and the heart, blood vessels are central to this system. The main blood vessels are arteries and arterioles, which carry oxygenated blood into the body, veins and venules, which return deoxygenated blood, and capillaries, which are extremely narrow and allow for exchange of nutrients for waste at the cells. As with any bodily system, blood vessels are subject to damage and failure. Aneurysms are one such pathology, and although most common in arterial vessels, may occur anywhere.

In simple terms, an aneurysm is an abnormal bulge in the wall of a blood vessel. These vascular dilations display a wide variety of shapes and sizes, and may occur anywhere in the body, but are often symptomless. Symptoms generally only materialise through rupture of the aneurysm and subsequent haemorrhaging, or through the aneurysm serving as a nidus for thrombosis and embolisation. Consequently, aneurysms located in the heart, aorta or brain are especially associated with a high risk of death or permanent damage should the aneurysm rupture. This investigation uses models of cerebral aneurysms, also known as intracranial aneurysms, in the experiments performed and are typically found in the circle of Willis.

Should an intracranial aneurysm rupture the patient will experience a haemorrhagic stroke. This most commonly manifests itself as subarachnoid haemorrhaging – bleeding into the space between the skull and brain, which may elicit severe complications, such as nerve damage or death. The 24-hour mortality rate is commonly reported as 40-50% and a further $\sim$25% of patients die due to complications within 6 months. Furthermore, roughly 1 in 4 survivors experience some form of permanent disability. There are approximately 30,000 cerebral aneurysm ruptures per year in the United States that lead to subarachnoid haemorrhaging and roughly 5% of the population is estimated to have at least one intracranial aneurysm, implying that $\sim$0.2% of cerebral aneurysms rupture yearly [65]. Although the vast majority of aneurysms may therefore remain symptomless, the severity of a rupture means effective management and risk assessment of patients is extremely important.

Larger aneurysms in the aorta or heart are frequently detected prior to rupture in regular health check-ups as bruits can be heard through a stethoscope by a general practitioner. This is unlikely in the case of intracranial aneurysms, as bruits

may not be present, and any potential sounds will also be weaker due to the smaller size of the blood vessels and noise reduction by the skull. Cerebral bruits have, however, been found using a phonocatheter on exposed intracranial aneurysm sacs, and non-invasively on the eye [21, 39]. Cerebral aneurysms are none the less usually diagnosed through medical imaging, such as Computed Tomography or Magnetic Resonance Imaging, and are therefore often discovered by chance. Once diagnosed the options are to leave the aneurysm and monitor it for any change, or surgical repair. Common surgical methods, such as clipping performed in an open craniotomy, and endovascular repair, are accompanied by risks [82]. It is thus beneficial to avoid surgery whenever possible, which necessitates an accurate risk assessment. This need is further compounded by possible waiting periods prior to receiving preventative surgery, in which complications may occur. Extensive research is therefore performed in order to attempt to quantify the chance of rupture. This includes research into the pathophysiology of aneurysms and rupture conditions, and modelling and simulation of blood flow through aneurysms, none of which is fully understood. In particular, computer simulations in conjunction with medical imaging is being looked into as a patient specific predictive tool. In order to continue to improve on these simulations, development of experimental methods and resulting data is needed for validation and verification of the various models.

2.2 Haemodynamics

A plethora of factors have been associated with the pathophysiology of aneurysms, which can all mostly be categorised as being blood-, wall-, or haemodynamics-borne. It is hypothesised that a combination of these factors is required for an aneurysm to develop and eventually rupture, and that they are often interrelated. Blood- and wall-borne factors are however largely dependent on biological conditions, in so far as they are caused by cellular or molecular faults or genetic disposition. These factors therefore generally fall beyond the scope of this thesis, although they are an important part of the puzzle. The haemodynamic factors are, however, at the core of this thesis, as flow within aneurysms was measured. Haemodynamics may further have a direct effect on biological conditions through mechanotransduction, as outlined in section 1.1. Flow features such as flow impingement, pressure, and wall shear stresses are thought to play a part in the pathophysiology, and the geometry of the aneurysm is therefore an important determinant of the observed flow [65]. A basic understanding of fundamental haemodynamic principles is therefore necessary, as it allows for improved analysis of the results obtained and their limitations. Ku (1997) presents an extensive review of blood flow in arteries, and some of the key principles are outlined in this section, supplemented by other resources where necessary [38].

As for other fluid flows, Navier-Stokes equations can be used to mathematically describe blood flow. For an incompressible, Newtonian, viscous fluid, conservation of momentum results in:

$$\frac{\partial \mathbf{u}}{\partial t} + (\mathbf{u} \cdot \nabla)\mathbf{u} = -\frac{1}{\rho}\nabla p + \nu \nabla^2 \mathbf{u} + \frac{1}{\rho}\mathbf{F} \tag{2.1}$$

and conservation of mass results in the continuity equation:

$$\nabla \cdot \mathbf{u} = 0 \tag{2.2}$$

where $\mathbf{u}$, p, ρ, ν and F are the velocity vector, pressure, density, kinematic viscosity and body forces respectively. It is important to note that already at this relatively early stage of a formulation of a mathematical model for blood flow several assumptions and simplifications have been made. In particular the incompressibility assumption common for most liquids (such as blood or water) is only partially true, as a completely incompressible liquid would not propagate sound waves.

Solution of the governing equations, with or without simplifications, as is done for CFD/DNS, requires appropriate boundary and initial conditions defined by the physics of the flow, as well as appropriate physical parameters, e.g. density and viscosity.

One of the main characteristics of blood flow is its pulsatile nature, driven by the contraction and relaxation of the heart, referred to as the systole and diastole. This leads to varying pressures, and thus velocities, and it has been shown that a flow is more likely to destabilise during deceleration, increasing the likelihood of turbulence generation [59]. Furthermore, flow may even be reversed during the diastole in some arteries. The effect of pulsatile flow is typically quantified through the dimensionless Womersley number which describes the ratio of the pulsatile flow frequency, f, to the viscous forces:

$$\alpha = R\sqrt{\frac{n}{\nu}} \tag{2.3}$$

where R is the radius of the cylindrical blood vessel, ν the kinematic viscosity, and $n = 2\pi f$. The experiments performed in this thesis used steady flow, and as such any effects associated with pulsatile flows are not taken into account, and therefore not extensively elaborated on.

Blood pressure and velocity will also vary depending on physical exertion and a wide variety of other factors. As is convention for other fluid flows, the Reynolds number is used to quantify the flow:

$$Re = \frac{UD}{\nu} \tag{2.4}$$

where U is the mean stream-wise velocity through a geometry with characteristic length D, in this case the diameter of the cylindrical parent artery. It describes the ratio of inertial and viscous forces, and when high enough, flow separation and transition to turbulence will occur. In steady pipe flow this threshold, or critical Reynolds number, is typically reported around 2000-2300, however this does not necessarily apply to flows in more complex geometries. Due to the complexity of the cardiovascular system Reynolds numbers will vary throughout the body, with values as high as 10000 observed in the aorta [75]. Outside the main arteries, Reynolds numbers of 100-1000 are more common, and flow is generally laminar with secondary flows generated at curves and branches. In short, Reynolds numbers will vary depending on the loss of blood pressure through vascular resistance, which is greatly dependent on vessel diameter and the number of bifurcations. Consequently, Reynolds numbers in the cerebral arteries are on the lower end of the spectrum, typically $<$500.

The properties of the vessels are also important to consider. The smoothness of the walls will play a significant role when it comes to the generation of turbulence, an effect which is well documented in pipe flows through the Moody Diagram [50]. The rougher the surface, the more easily turbulence is generated. Arteries are naturally very smooth, but roughness may increase due to build-up of fatty deposits.

Arterial walls are viscoelastic, and although the effect this has on the measurement of vibrations as discussed previously is debated, it is commonly seen as negligible when it comes to affecting the flow itself [66]. However, it is important to bear in mind that blood vessels are living organs which constrict and dilate depending on stimuli, an effect which can have a significant effect on blood pressure and velocity. Vessel diameters will also vary greatly as the blood passes through the body irrespective of vasoconstriction/dilation. Mathematically, a change in area, A, can be accounted for in the 1D continuity equation as:

$$uA = Q(t) \tag{2.5}$$

Which when applied to the 1D, unsteady Euler equation (a simplified version of N–S equation for inviscid flow):

$$\frac{\partial u}{\partial t} + u\frac{\partial u}{\partial x} = -\frac{1}{\rho}\frac{\partial p}{\partial x} \tag{2.6}$$

provides an estimate for the local pressure changes given by:

$$\frac{\partial p}{\partial x} = -\frac{\rho}{A}\frac{dQ}{dt} + \rho\frac{Q^2}{A^3}\frac{dA}{dx} \tag{2.7}$$

A negative pressure gradient exists when the flow accelerates ($dq/dt > 0$) and the area converges ($dA/dx < 0$), however if the flow decelerates ($dq/dt < 0$) and the area expands ($dA/dx > 0$) the pressure gradient may be positive and flow separation is possible. The latter is therefore considered an adverse gradient, and is illustrative of the case of an aneurysm, in which the vessel bulges out abnormally.

Blood flow prior to the aneurysm location may also be of importance. Curvature of the vessels will elicit a skewing effect as centrifugal forces affect the flow. This effect is quantified by the Dean number [34]:

$$De = (\delta)^{1/2} \cdot Re \tag{2.8}$$

where $\delta = \frac{radius\ of\ tube\ cross-section}{radius\ of\ curvature\ of\ the\ centreline}$.[1] Typically, the velocity will be skewed towards the outer wall in arterial flows, and sufficiently high Dean numbers may cause separation at the inner wall. Furthermore, asymmetries have been shown to cause helical flow patterns in the aorta, which help suppress transitional behaviour [51].

The properties of blood as a fluid are also an important characteristic of human blood flow. Blood consists of plasma with a wide variety of cells, proteins and ions in suspension, of which red blood cells are the most plentiful, comprising roughly 45% of blood by volume. These semisolid particles effectively increase the viscosity of blood to roughly 4 times that of water, and also give blood its non-Newtonian properties. Blood cells will clump together into larger particles, particularly at low shear rates, or in small branches and capillaries, effectively increasing the local viscosity. Conversely, at high shear rates the viscosity decreases, making blood a shear-thinning fluid. Blood can none the less be considered Newtonian in most arteries, however its non-Newtonian rheology may give rise to errors when calculating wall shear stresses, given by

$$\tau = \mu\frac{d\mathbf{u}}{dr} \tag{2.9}$$

[1] Note that there is some lack of convention for this non-dimensional parameter, see e.g. [7]

as it depends on the (dynamic) viscosity, μ, which is especially hard to determine near walls for a non-Newtonian fluid. It is also argued that the suspension of particles will affect the creation of turbulence on a fundamental level, as red blood cells are similar in size to the microscales at which viscous energy dissipation occurs [2]. Furthermore, blood has viscoelastic properties, which means considering only the viscous properties is not necessarily adequate [78].

All in all the wide variety of factors that contribute to human blood flow require careful consideration, and are hard to accurately recreate both in a simulated and experimental setting. The experiments performed for this thesis are in many ways idealised, and restricted by this, and results must be analysed with the above in mind. Combined with exact representation of patient specific anatomical and structural factors, i.e. blood, flow and wall characteristics, accurate patient specific simulations and experiments pertaining to aneurysm rupture may become increasingly possible, and the physical variables that govern aneurysm pathophysiology may be more accurately identified.

2.3 Turbulence [25, 60]

A turbulent flow regime is characterized by highly stochastic, chaotic behaviour and three dimensional vorticity, and usually occurs at high Reynolds numbers. As a result of this complexity a complete mathematical description of turbulent flow remains one of the unsolved problems in physics and applied mathematics. Physically, turbulence is briefly described as a formation of vortices of many different scales within the flow. The complexity increases as they interact with each other, and eventually this leads to energy dissipation when the cascading eddies become small enough for molecular diffusion to cause viscous dissipation of energy. In other words, mechanical energy is converted to thermal energy through friction at the molecular scales, and a small fraction of energy will also be lost through other mechanisms, such as sound generation. The non-linearity of the governing equations of fluid flow is a key feature, and cause, of turbulence and therefore cannot be neglected. Even though the governing equations are deterministic, small changes in initial conditions will lead to large changes in the outcome, and the results will seem stochastic in nature. Because of this, a statistical approach to solving turbulence has become the norm, in which the flow is decomposed into a mean component, and a fluctuating component. E.g. for the velocity:

$$\mathbf{u} = \mathbf{U} + \mathbf{u}' \tag{2.10}$$

This is commonly referred to as the Reynolds decomposition, and when applied to the governing equations results in the Reynold's Averaged Navier-Stokes equation, which includes a new term called the Reynolds stress term. It describes the fluctuating contribution to the non-linear terms, and is not a physically defined stress, but acts like one, and thus accounts for the turbulent fluctuations in fluid momentum. It arises from the flow itself which makes simplification complicated or impossible without losing the defining physics of the problem. The result is more variables that have to be dealt with in order to find a solution. The major issue with a mathematical model for turbulence therefore lies in the turbulence closure problem, meaning there are fewer equations than unknowns when an analytical solution is attempted

for any given problem. To counter this, DNS of the (unsimplified) governing equations can be performed in order to numerically calculate instantaneous solutions over sufficiently small time steps and spatial meshes. Unfortunately, even modern supercomputers are not yet powerful enough to make DNS of most engineering flows viable, however simple flows, or flows at sufficiently low Reynold's numbers may be resolved. DNS has been performed for flow through the intracranial aneurysm models used in this thesis [31].

The usefulness of typical flow measurement techniques is consequently somewhat limited by the randomness of turbulence, and further analysis is required for characterisation of the flow. To this end, an analysis in the spectral domain is commonly performed. Calculating the Power Spectrum Density (PSD) describes the flow through determining the energy distribution of the signal with respect to frequency (or equivalently, wavenumber). Further information on how this was calculated for the experiments performed in this thesis can be found in section 2.4.1.

The basic description of turbulence so far is based on the classical and conventional ideas behind turbulence, and is commonly referred to as Kolmogorov turbulence. Kolmogorov built upon the idea of turbulence consisting of a cascade of eddies, and hypothesised behaviour that would lay the foundation for turbulence theory. A mathematical description is usually given on the basis of the mean turbulent kinetic energy (TKE) per unit mass of the flow, with the energy spectrum, $E(k)$, defined as:

$$\frac{1}{2}(\overline{u_i u_i}) = \int_0^\infty E(k)dk \tag{2.11}$$

where k is the wavenumber, inversely proportional to the the size of the eddy, and $\overline{u_i u_i}$ the ensemble averaged fluctuating velocity with summation over component i. Written in similar terms, the highly important energy dissipation rate may be defined as

$$\varepsilon = 2\nu \int_0^\infty k^2 E(k)dk \tag{2.12}$$

and therefore has dimensions of energy per unit mass per second.

The largest scales, often called the integral scales, contain the majority of the turbulent kinetic energy and are governed by the geometry of the boundaries affecting the flows. Kolmogorov also postulated that even though the largest eddies were caused by geometrical and directional conditions, this information would be lost as the cascading eddies reduced enough in scale. This meant that for sufficiently high Reynolds numbers the small scale (Kolmogorov microscale) turbulent motions were statistically isotropic, and thus had to be characterised by the same parameters in all flows: the dissipation rate, ε and the kinematic viscosity, ν of the fluid. By dimensional analysis the Kolmogorov length scale, η, is therefore defined as:

$$\eta = \left(\frac{\nu^3}{\varepsilon}\right)^{1/4} \tag{2.13}$$

Similarly, a Kolmogorov time scale, τ, can be defined:

$$\tau = \left(\frac{\nu}{\varepsilon}\right)^{1/2} \tag{2.14}$$

The theory so far has a useful implication from a physical point of view. The time scale in which dissipation takes place is so rapid that the dissipation rate is

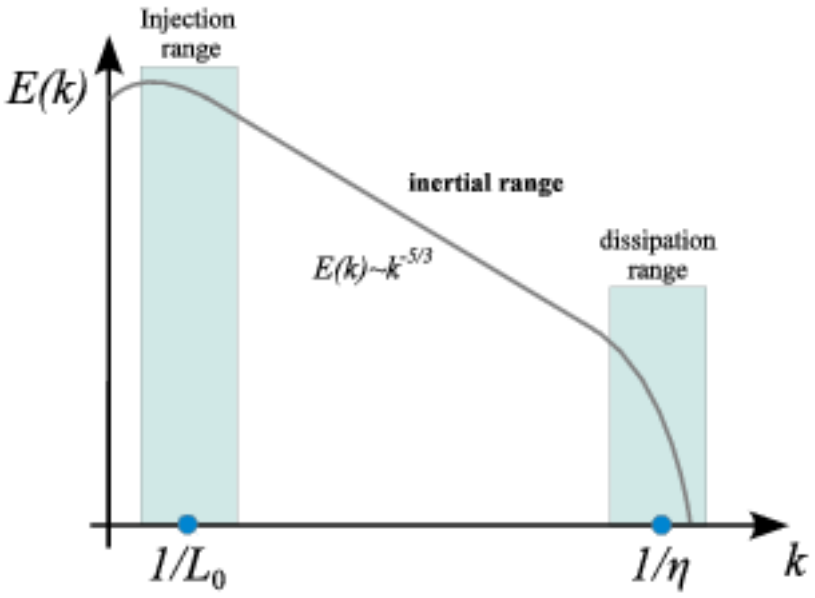

Figure 2.1: A schematic energy spectrum of Kolmogorov turbulence. Reproduced from [73]

primarily determined by the large, energy containing scales, and not the microscales. This follows from the fact that the TKE available for dissipation is dependent on the TKE storage and production in the flow, which per Kolmogorov's theory is a property of the integral scale. Consequently the dissipation rate can be *approximated* on dimensional grounds as:

$$\varepsilon \propto \frac{u^3}{L} \tag{2.15}$$

where u is a characteristic velocity, and L an integral scale length.

A model for the scales between the integral and microscales was also developed. At these scales energy is transferred down into the microscale where it is dissipated, however, Kolmogorov hypothesized that these scales were still too large for viscous effects to play a significant role, and thus there was no dissipation of energy. It is therefore commonly named the inertial range. Hence the range can be characterised purely by a length scale, r, and the energy dissipation at the microscales, ε. Through dimensional analysis the only possible solution for an energy spectrum function that satisfies Kolmogorov's hypothesis is:

$$E(k) = C\varepsilon^{2/3}k^{-5/3} \tag{2.16}$$

where C is a universal constant (typically reported as 1.5), and k the wavenumber, proportional to $1/r$ (and thus also proportional to the frequency). When the power spectrum density found from experimental data is plotted in a logarithmic scale one would therefore expect to see a linear section of slope -5/3 corresponding to the inertial range of eddies. An idealised PSD plot can be seen in figure 2.1.

The above theory is based on measurement of the (fluctuating) velocities in a flow, however the acoustic method used in this thesis measures pressure fluctua-

tions[2]. Although related to the flow velocities, observed behaviour in the calculated pressure PSDs will be different. Based on Kolmogorov's assumptions, pressure fluctuations in a turbulent flow may be similarly characterised as the velocities, and the mean-square pressure fluctuation may be mathematically described through a pressure spectrum, $\pi(k)$ [26]:

$$\overline{p^2} = \int_0^\infty \pi(k)dk \tag{2.17}$$

For isotropic turbulence the spectrum in the inertial subrange is then given by

$$\pi(k) = \alpha\rho^2\varepsilon^{-4/3}k^{-7/3} \tag{2.18}$$

where ρ is the fluid density and α a constant, reported as $1.32C^2 = 2.97$. Furthermore, a shear flow may create an additional contribution which varies with $k^{-11/3}$.

It should be noted that the above is only a basic presentation of simple turbulence theory. Significant advances and corrections have been made, based on more thorough derivations and calculations. However, as much of turbulence theory is still being developed and understood, and commonly disputed, the above is adequate for a basic investigation of unsteady flows within the aneurysms considered in this thesis. Turbulence is not a well-defined phenomenon, and will in reality display significant variations from flow to flow. In general, it is therefore often argued that limited emphasis should be put on comparison with a gradient, be it -5/3, -7/3 or -11/3, as the robustness of the theory through which these have been derived is somewhat lacking and only applicable to ideal and specific scenarios. Although flow regimes are typically classified as laminar, transitional or turbulent, describing a flow using only the regime as a descriptor may be insufficient due to the wide range of variation seen within the regimes.

By applying the above concepts to the present case, several clear discrepancies are apparent. Firstly, Kolmogorov turbulence is idealised, and fully developed. This is not the case for the flows considered, as the intention is to determine when the flow transitions away from the laminar regime, and the observed flow will be highly anisotropic and non-homogeneous. Transitional behaviour will be observed, starting with flow separation and vortex formation. Flow separation may occur when a boundary layer travels far enough against an adverse pressure gradient[3] and the flow detaches from the surface, developing into vortices which result in fluctuating velocities. At higher Reynolds numbers the non-laminar behaviour will continue to develop and typical turbulent characteristics will become more apparent. The aneurysm geometries containing the flow are complex, which may lead to localised flow separation and turbulence formation. Failure to keep this in mind could potentially result in flow separation being overlooked by the measurements. Furthermore, the theory assumes a Newtonian fluid, and although blood is non-Newtonian, water was used in the experiments performed.

A logarithmic PSD plot will serve as the main method of identification of fluctuations for the measurements acquired acoustically. Although an idealised slope of -7/3 may not be present, the presence of an energy cascade will be indicative of fluctuating flows in which energy is transferred down to the microscales. Near the

[2]See section 2.4.1

[3]See section 2.2

transitional Reynold's number initial flow separation and vortex formation may also manifest itself through increased power only at certain frequencies and an energy cascade may not be apparent. The x-ray PTV analysis will visualise the flow and allow for description of flow patterns, velocities and accelerations that may further confirm the presence of fluctuations.

2.4 Measurement Methods

Many of the experimental techniques required for measurement of (turbulent) flows are either intrusive or require full, undistorted optical access, neither of which are straight forward when measuring the flow within a complex geometry such as an aneurysm. Two non-intrusive measurement techniques used for the purpose of identifying flow patterns within a complex and opaque geometrical model have therefore been used, and are outlined in this chapter.

2.4.1 Acoustic Measurements

The equipment and experimental setup was based on one used by Xu [90] and is further described in chapter 3. In short, a standard data acquisition setup was used, in which a contact microphone was used to sense pressure differences on the outer surface of the aneurysm models.

Flow Induced Noise

Fundamentally, sound is a mechanical wave that propagates through a medium. In gases and liquids these waves are of the compression type, i.e. longitudinal waves. Typically, the vibration of an object will displace the surrounding particles in the medium, effectively creating regions of compression and rarefactions, which are manifested as pressure differences (or equivalently, density differences). Solids will also propagate sound through shear waves, i.e. transverse waves, through elastic deformation of the material perpendicular to the direction of wave travel. Pressure differences can be detected, and the present measurement method relies on this principle.

Qualitatively, flow generated sounds arise when the flow separates and leaves the laminar regime so that vortices are formed whose unstable, oscillatory behaviour results in fluctuating velocities at any given point. Following the Navier-Stokes equations, velocity fluctuations are inherently coupled with pressure fluctuations, and by extension these pressure fluctuations are also related to vorticity fluctuations [36]. As the pressure fluctuations hit the surrounding wall they will propagate out of the flow through the surrounding medium. Flow induced noise is therefore highly dependent on the medium and geometries/surfaces it interacts with. Fluid-structure interaction may not only cause fluctuations, but factors such as dampening and resonant frequencies will also affect the measured signal, depending on the sensor location. As mentioned previously, this method is therefore unable to conclusively determine the cause of the measured vibrations, since pressure fluctuations at the wall are measured, and not velocities directly. Some fluctuations may be lost depending on the materials ability to propagate pressure waves, and the resulting signal is

a combined sum of the noise produced within the aneurysm at the point of measurement. The technique is therefore Eulerian in nature. If the vibrations/pressure differences lie in the audible range (roughly 20Hz–20kHz) and have adequate power, they will be perceptible to the human ear, however signals outside of this range may still be picked up by a sensor such as a microphone, and analysed. Using measurement of flow generated pressure fluctuations in order to quantify the flow therefore differs fundamentally from most other turbulent measurement techniques. Whereas a technique such as hot wire anemometry measures a velocity at a point in the flow, allowing for determination of the mean and fluctuating component associated with turbulence, acoustic measurements only pick up on the flow fluctuations that cause vibrations/pressure differences on the wall. As such there is no need for further decomposition of the signal into a mean and fluctuating component, as is traditionally done when analysing turbulence, at least not for steady flow.

Significant effort has been dedicated to understanding flow induced vibrations and noise, as it has countless engineering applications, including aero/hydrodynamic effects on structures and vehicles, flow through valves, pipes etc., and jet noise in the aerospace industry. Noise and vibrations are inherently related, although it should be noted that sound generation can often be divided into two main mechanisms. Firstly, noise can be produced by the fluid inducing vibrations on a structure it passes, and secondly, noise can be generated purely by the (turbulent) fluid flow. Common for all noise generation is that it is driven by pressure differences, and ultimately density differences. Aeroacoustic analogies have been developed and used for more than half a century for the purpose of acoustic analysis. Typically, they are based on the (compressible) Navier-Stokes equations which are rearranged as an inhomogeneous wave equation consisting of pressure and velocity fluctuations, stresses and forces. The governing fluid dynamic equations are thus coerced into a form similar to the acoustical wave equation:

$$\nabla^2 p - \frac{1}{c^2}\frac{\partial^2 p}{\partial^2 t} = 0 \tag{2.19}$$

which gives rise to the "analogy" part of the naming convention, although the formulation remains exact. In equation 2.19 c is the speed of sound, which will vary from medium to medium, and p is the acoustic pressure, i.e. the deviation from the ambient pressure, and can be compared to the fluctuating component of a Reynolds decomposition of pressure in fluid mechanics. The solution of the aeroacoustic analogies is modelled analytically using source terms, i.e. monopoles, dipoles and quadrupoles. Usually, simplifications are made for the purpose of linearisation and the solutions represent propagation of acoustic waves caused by turbulent fluctuations in an ideal surrounding medium. Some of the most widely used aeroacoustical analogies are the Lighthill analogy, which is the foundation of aeroacoustic analysis and used for free flows such as a jet, the Curle analogy, and the Ffowcs Williams-Hawkings analogy. Improvements in the field of computational fluid dynamics have also seen the emergence of numerical solution of governing aeroacoustic equations. Much can be said about these analogies and equations, however only a simple description will be presented as part of this thesis.

Understanding the behaviour of the (fluctuating) pressure mathematically is an important starting point. By taking the divergence of the incompressible N-S equations and performing a Reynolds decomposition of the velocity and pressure, the

fluctuating pressure component can be expressed as solution of a Poisson equation. In Einstein summation notation:

$$\frac{1}{\rho}\nabla^2 p' = -2\frac{\partial \bar{U}}{\partial x_j}\frac{\partial u_j'}{\partial x_i} - \frac{\partial^2}{\partial x_i \partial x_j}\left(u_i' u_j' - \bar{u_i}' u_j'\right) \tag{2.20}$$

The right hand side of the equation represents a forcing term containing a linear contribution from the fluctuating quantities ("shear noise") and a non-linear contribution, physically interpreted as "self noise" [5, 33]. The linear and non-linear contributions are often characterised as rapid and slow fluctuations, respectively, and it has been shown that the non-linear/slow component is typically larger than the linear/rapid component in turbulent flows, except near the wall, where they are of similar magnitude [36]. An analytical solution of 2.20 can be written in terms of an appropriate Green's function, G, as a convolution product of the source term, ST:

$$p' = \rho G \times ST \tag{2.21}$$

As a simple example, in the presence of an infinite flat plate G can be chosen as the half-space Green's function:

$$G = \frac{1}{2\pi}\frac{1}{|\mathbf{x} - \mathbf{y}|} \tag{2.22}$$

and illustrates the pressure fluctuations dependency on the velocity field as a whole given its inverse dependency on the position. Pressure is therefore a non-local variable, a key reason for why statistical modelling of pressure has proved more difficult than for velocity fluctuations, and a pressure fluctuation is a sum of surrounding velocity fluctuations. Kim (1989) showed that pressure fluctuations are much more intermittent than velocity fluctuations, partly explained by the pressures high correlation with vorticity. However, Kim further showed that the wall pressure in a cylindrical pipe could be correlated to an overall footprint of the velocity structures at the dimensionless wall distance, $y^+ \sim 20$, as the contribution from the velocity field peaked at this point, although the velocity field even at the opposite wall also contributed. An interpretation of pressure fluctuations measured on the wall of a complex geometry as they relate to fluctuating velocities is therefore somewhat difficult.

Turbulent, flow-induced pressure fluctuations are further often classified as sound and pseudo-sound. Ffowcs Williams describes pseudo-sound as an essentially local field quite independent of fluid compressibility (ie. it is governed by the Poisson equation described above), while the sound field proper radiates away via compressible motion. It is the pseudo-sound field that induces vibration on structures supporting turbulent boundary layers. Furthermore, it is assumed that the turbulence is unaffected by the presence of a sound field, justified by experimental observation that only 10^{-4} of the turbulent energy in a jet flow escapes as sound [88]. Depending on the flow in question, an analysis of the pseudo-sound field, allowing for determination of pressure fluctuations on the wall of a structure, may be adequate and can be used for further analysis of vibrations and sound generation by the structure. In order to describe the acoustic part of the flow, i.e. the real sound field, compressibility effects must be taken into account. This effectively means replacing the Poisson equation described above with a wave equation in which density is the fundamental variable. This was performed by Lighthill in his pioneering work in deriving the Lighthill equation, which forms the foundation of aeroacoustic analogies [43, 44, 56].

Although the derivation will not be reproduced here, it is based on the compressible Navier-Stokes equations, and is an exact formulation, in that no simplifications have been made. Using Einstein notation it is given as:

$$\frac{\partial^2 \rho}{\partial t^2} - c^2 \nabla^2 \rho = \frac{\partial^2 T_{ij}}{\partial x_i \partial x_j} \tag{2.23}$$

where $T_{ij} = \rho v_i v_j - \sigma_{ij} + (p - c^2\rho)\delta_{ij}$ is the Lighthill turbulence stress tensor in which δ_{ij} is the Kronecker delta operator. T_{ij} contains the acoustic source terms, where $\rho v_i v_j$ describes the contribution of the Reynold's stress, or unsteady convection, of the flow, σ_{ij} describes sound generated by shear (and is often assumed negligible), and $(p - c^2\rho)\delta_{ij}$ represents non-linear acoustic generation processes. The relative contribution from each term will be dependent on the characteristics of the flow.

A common simplification to the Lighthill equation involves approximating the relationship between pressure and density as linear, so that $p - p_0 = c(\rho - \rho_0)$ where p_0 and ρ_o are the characteristic equilibrium pressure and density of the fluid, and p and ρ the total measured/calculated pressure and density at a point. Upon substitution into equation 2.23 and after some gentle rearrangement:

$$\nabla^2 p - \frac{1}{c^2}\frac{\partial^2 p}{\partial^2 t} = -\frac{\partial^2 T_{ij}}{\partial x_i \partial x_j} \tag{2.24}$$

where now $T_{ij} = \rho v_i v_j$, and the similarity to the acoustic wave equation becomes clear and the aeroacoustic analogy apparent. Analytical or numerical solution of these equations will not be further discussed, however the equations provide a foundation for physical interpretation of the measured pressure fluctuations. In particular, it is apparent that the microphone placed on the wall of the aneurysm model will likely pick up on both sound and pseudo-sound, and given the small contribution of real sound, pseudo-sound may dominate the signal. This means the measured pressure fluctuations are mostly related to the velocities of the flow through the Poisson equation defined above.

Data Acquisition and Signal Analysis

The signal acquired from the microphone was passed through an amplifier and a DAQ (Data Acquisition device, including an analogue to digital converter) before being saved to a file. The process of converting a continuous, analogue signal into a discrete, digital signal requires consideration in order to ensure accuracy and validity of the acquired data. One of the most important parameters is the sampling frequency, meaning the rate at which values of the analogue signal are quantized and recorded for the digital signal. The digital signal is acquired at discrete time intervals and the length of this is critical when it comes to how much information is obtained. The Nyquist-Shannon sampling theorem infers that a signal can be perfectly reconstructed if the sampling rate, f_s is greater than twice the highest frequency, f_{max} contained in the signal.

$$f_s > 2 \cdot f_{max} \tag{2.25}$$

If the sampling rate is lower, then the reconstruction will result in imperfections known as aliasing. Simply put, if the data points are too far apart, the reconstruction may result in a signal that is different from the original signal. A visual

representation can be seen in figure 2.2. A sine wave has been inadequately sampled, and the reconstruction yields a wave with lower frequency than that of the actual wave.

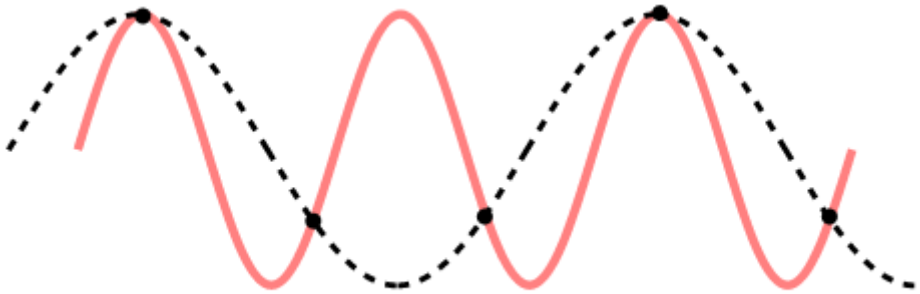

Figure 2.2: Sampling of a sine wave at a frequency lower than the Nyquist frequency results in inaccurate reconstruction: aliasing. Reproduced from [15]

The bit depth is another important parameter, as it determines the numerical accuracy of the digitised signal values. A bit depth of 16 bits, will allow for 2^{16} values within the range of the signal. If the bit depth is too small, or the signal range too large, the resolution of the discretised signal will therefore suffer, and small variations will be lost.

In a typical measurement, such as sound being recorded by a microphone, unwanted signals will also be measured, referred to as noise. The microphone will pick up acoustic noise, i.e. other sounds/vibrations in the area at the time of measurement, and electrical noise, both from other electrical equipment and power lines around, and within the microphone and amplifier. Additionally there will be quantisation noise and jitter (deviation from the precise sampling time intervals), however these effects are usually small. Limiting noise is therefore important in order to clearly single out the sound created by the flow.

Filtering of the signal can prevent noise by limiting the frequencies that are recorded. A low pass filter will set an upper limit on the frequencies that can be measured. Paired with a suitable sampling frequency this will prevent aliasing which would manifest itself as errors in lower frequencies otherwise. Filtration for this purpose must be performed on the analogue signal, as a low pass filter applied after digitalisation will not prevent aliasing. In real applications frequency filters are not perfect, and higher frequencies will be allowed through near the cut-off frequency. A sampling frequency slightly higher than the lowest possible frequency defined by the sampling theorem is therefore desirable and is known as oversampling. Further filtration can be performed after digitalisation for the purpose of signal analysis, for example by filtering out specific frequencies that are known sources of noise. However, as already mentioned, filters are not perfect, and applying one needlessly may have a detrimental effect on the data.

Much of signal analysis relies on the principle of superposition, which is extended through to Fourier Series and Transforms. In short, Fourier showed that a signal could be expressed as the sum of simpler sine or cosine components. Whereas Fourier Series are used for periodic functions and result in a discrete sum of complex exponentials that represent the original function, Fourier Transforms are generalised to non-periodic signals and result in a continuous integral of complex exponentials.

In other words a Fourier Transform converts a signal from the time domain into the frequency domain. Consequently these are linear, and reversible operations. For a vector, x, of length N, the Discrete Fourier transform results in a transformed vector, X, also with length N, and is defined mathematically as:

$$X(k) = \sum_{n=1}^{N} x(n)\omega_N^{(n-1)(k-1)} \tag{2.26}$$

where $\omega_N = e^{-2\pi i/N}$ and i the imaginary unit. The transform variable, k, and the independent variable, n, correspond to the indices of the vectors, and are related to the physical domains through the requirement that the values are separated at a constant interval; the sampling frequency. Hence, k represents frequency, and n, time.

Direct computational application of this definition is, however, inefficient. Fast Fourier Transform algorithms are therefore used to improve performance and have a computational complexity $O(nlogn)$ compared to the Discrete Fourier transform's $O(2n^2)$, whilst still computing the DFT exactly. Several algorithms have been developed, most of which are based on factorizing the DFT matrix into a product of sparse (mostly zero) factors [84]. The various algorithms are a complex topic in their own right and will not be further discussed in this thesis. It suffices to say that a FFT algorithm is implemented in Matlab through the "fft" function, and forms the foundation of the spectrum density estimation performed. Emphasis should be placed on the word "estimation", as there are several ways of computing the (power) spectrum density, and there is no universally agreed upon method. In its simplest form the Fourier transform of a signal can be computed and the power found by squaring the resulting modulus, allowing for determination of the distribution of power with respect to frequency. This is sometimes referred to as a periodogram, but is rarely considered the most accurate method when analysing non-periodic signals due to the fact that the signal which is Fourier transformed is a finite sequence out of a theoretically infinite random process (i.e. random noise components or random turbulent effects). Consequently, the method is an inconsistent estimator, dependant on the point at which the finite sequence is taken, and converges poorly even for high numbers of samples. Methods have therefore been developed which improve on this aspect of spectrum estimation, one of which is Welch's Method. First the data sequence is partitioned into segments, usually with some overlap. Each segment is then windowed. These step are fundamental to Welch's method, even though several overlapping percentages and window functions which can be used exist. The Discrete Fourier Transform is then computed (using FFT) from which the periodogram for each segment can be obtained, before being averaged to obtain Welch's estimate of the PSD. The method is therefore more statistically robust, and is considered an improvement on standard periodogram spectrum estimates due to increased consistency and reduced effect of noise, albeit by sacrificing some frequency resolution [86, 72]. Many factors in Welch's method can be tweaked, such as the overlap percentage and the windowing function, and the estimation aspect of determination of a PSD is therefore once again emphasised.

Mathematically Welch's estimate for the power, P_W of a frequency, f is given as:

$$P_W(e^{i2\pi f}) = \frac{1}{KLU}\sum_{j=1}^{K}\left|\sum_{n=1}^{L} w(n-1)x(n-1+jD)e^{-i(n-1)2\pi f}\right|^2 \tag{2.27}$$

where L is the sequence length, D the number of overlapping points, and K the number of sequences needed to cover all the data points. $U = \frac{1}{N}\sum_{n=1}^{N} \mid w(n) \mid^2$ and $w(n)$ is the window function [27].

As the main use of PSDs in this thesis was for comparison with other PSDs, the focus was on using a spectrum estimation method which could be considered consistent. Welch's method was therefore used through the Matlab implementation in the function "pwelch" and sample code can be found in appendix A.

2.4.2 3D XPTV

X-ray Imaging

X-rays are a form of electromagnetic radiation which have been used extensively for imaging in the past century. They have exceedingly high theoretical resolution owing to small wavelengths ranging from 0.01 to 10nm, which furthermore allows for excellent penetration ability. Production is typically achieved by ionizing a target source, such as tungsten, with an electron beam generated by a voltage potential between a cathode and the (tungsten) anode. The x-rays can be detected in several ways, most notably through the use of scintillators, which when struck by an x-ray re-emit energy in the form of visible light, and can be coupled with photodetectors such as CCD or CMOS cameras for imaging. Further information on x-ray production and detection can be found in [23, 28] along with information on imaging techniques based on x-rays.

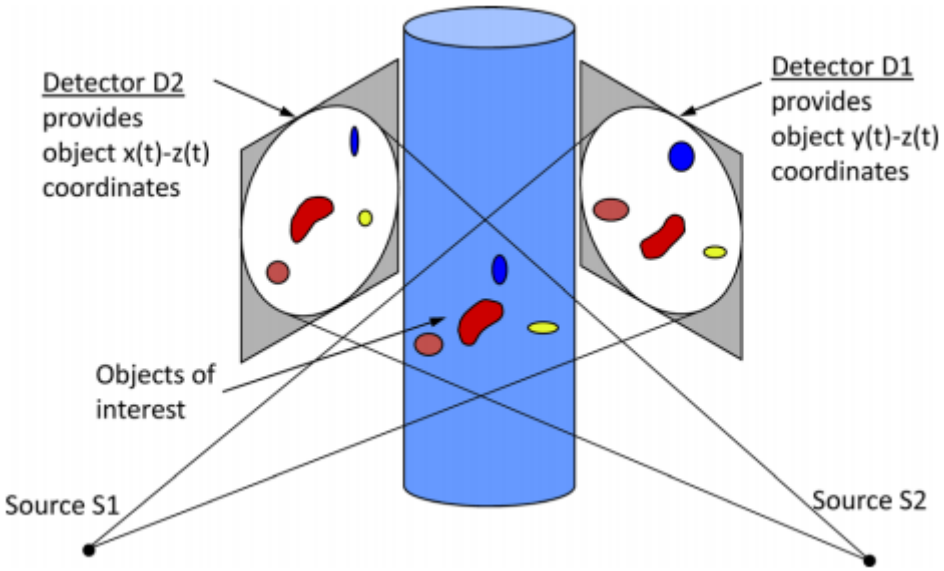

Figure 2.3: A stereographic x-ray setup. Two x-ray source-detector pairs are used to simultaneously produce a radiographic projection in both the x-z plane, and the y-z plane. Reproduced from [28]

The fundamental imaging technique is referred to as radiography. In short, x-rays are emitted as a cone beam and when detected the end result is a conical 2D projection of a 3D object, in which the intensity is dependent on the amount of attenuation experienced as the radiation passes through the medium. Out of the myriad of imaging techniques and methods which exist, stereographic radiography is most relevant for the present application to XPTV. Stereographic methods involve the use of two 2D radiographic projections in order to reconstruct a 3D image. X-rays are especially suited for this purpose due to their penetrative ability, as opposed to conventional optical imaging which is less capable of producing accurate 2D projections due to opaqueness of the subject matter. Because of the dynamic nature of flow imaging, acquiring the two image projections simultaneously is beneficial, and a schematic representation of the process can be seen in figure 2.3. Two source-detector pairs are used to concurrently produce a radiographic projection in both the x-z plane, and the y-z plane. If a particle can be identified in both planes its 3D coordinate can be determined, and subsequent image pairs can be used to analyse the temporal variations. Particle seeding of a fluid, as used in PIV/PTV analysis is therefore ideal for a stereographic x-ray setup, as local points of interest in the flow can be identified and followed over time in 3D. However, as x-ray contrast is directly linked to material density, common PIV/PTV particles cannot be used. Instead, particles with a heavy metal core and a low density outer shell, or vice versa, must be used, and achieving neutral buoyancy whilst keeping the particles small, yet resolvable has therefore been a challenge.

3D Reconstruction

Two *ideal* projections onto the $x-y$ and $x-z$ plane allow for trivial reconstruction of the three dimensional position of a particle [4]. The projections created by radiographic imaging are, however, a result of conical radiation, and the projected positions are therefore a function of the particles position in the dimension normal to the projection plane. For accuracy, this must be taken into account when reconstructing the 3D position of a particle. The reconstruction method is based in principal on one used by Doering, and can be compared to a 90 degree rotation of the sample in his experimental setup [19]. Doering's method has also been referenced for use in 3D reconstruction for other stereographic x-ray PTV set-ups [29]. It fundamentally depends on knowing the positions of the x-ray sources and detectors and requires two steps:

1. Transformation of the particle pixel coordinates from the projection image into a global coordinate system.

2. Determination of the 3D position using the global coordinates of the projected particle and the global coordinates of the x-ray source (from both source-detector pairs).

[4] By ideal projection it is meant that a point with Cartesian coordinates (x, y, z) will have projected coordinates (x, y) in the $x-y$ plane and (x, z) in the $x-z$ plane.

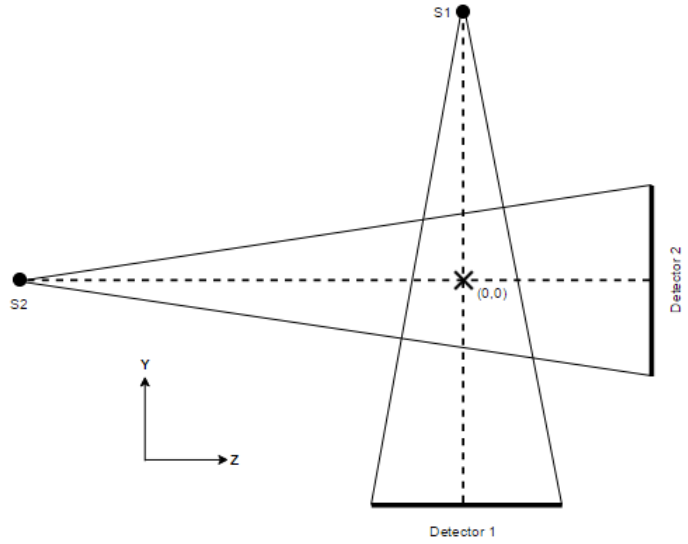

Figure 2.4: A 2D view of the plane the source-detector pairs were located in showing the conical radiation reaching the detectors and the overall geometry used for 3D reconstruction. The x-direction is out of the page and the origin of a global coordinate system defined where the centrelines from the two detectors cross.

A two dimensional diagram of the stereographic x-ray setup used for this thesis can be seen in figure 2.4 and will serve as a visualisation, although the following reconstruction will use three dimensional coordinates. The origin of the 3D, Cartesian, global coordinate system is defined at the point of intersection between the centrelines of the conical x-ray beams, therefore requiring the sources to be placed in the same plane. The coordinates of the x-ray sources, $S1$ and $S2$, are then $(0, y_{S1}, 0)$ and $(0, 0, z_{S2})$, respectively. Following the centrelines onto the projection plane gives coordinates $(0, y_{D1}, 0)$ and $(0, 0, z_{D2})$ for the $x - z$ and $x - y$ projection planes, respectively. The non-zero coordinates are dependent on the positioning of the sources and detectors in the setup, and are assumed known.

When imaged, the particle position in the projection plane will be given by a pixel coordinate. This is typically based on a pixel-origin in one of the corners of the image, and the pixel coordinates must be transformed to the global coordinate system. This can be done with reference to the points at which the centrelines hit the projection plane. These will have global coordinates $(0, 0)$ in the projection plane, but will have pixel coordinates defined as (x_0, y_0) in the projection plane. For an image with pixel-origin in the upper left corner, the transformation of a point with pixel coordinates (x, y) into the global system, (x_n, y_n) is given by:

$$x_n = x - x_0 \tag{2.28}$$

$$y_n = y_0 - y \tag{2.29}$$

Note that the transformation may differ depending on pixel-origin position in the image. The three dimensional coordinate is thus given by combining the transformed projection plane coordinates with the plane coordinate (e.g. z_{D2} for the $x-y$ plane). The transformed coordinates will be in units of pixels and can be converted by multiplying by the known pixel size.

The projected global coordinates of a particle, M_1 and M_2, can then be used to form two 3D line segments with $S1$ and $S2$, respectively. The particle position,

P, is then known to lie at any point on these line segments, and the intersection of the lines will therefore be the real three dimensional particle position. However, in reality intersection of the lines is unlikely due to small errors in determination of the exact coordinates of the particles (and the sources). The point at which the distance between the two lines is at a minimum must therefore be found. Several methods exist which can be used to determine this, but the simplest approach is perhaps to recognise that the shortest line between two skew lines is one that is orthogonal to both, and the problem can be solved from a geometric perspective. This approach differs from the one used by Doering, but the mathematical formulation is a well known method for determining the nearest points of two skew lines. Let

$$U = M_1 - S_1$$

$$V = M_2 - S_2$$

then the rays corresponding to movement from the source to the detector can be written as line segments

$$L_1 = S_1 + t_1 U$$

$$L_2 = S_2 + t_2 V$$

for $0 < t_{1,2} < 1$. The cross product of U and V is perpendicular to both lines:

$$W = U \times V$$

Then consider a plane formed by the translations of L_2 along W. It must contain the point $S2$ and be perpendicular to the vector formed by $V \times W$. The point on L_1 which intersects this plane is the point closest to L_2, and is therefore given by:

$$P_1 = S_1 + \frac{(S_2 - S_1) \cdot (V \times W)}{U \cdot (V \times W)} U$$

Similarly, the closest point on L_2 is given by:

$$P_2 = S_2 + \frac{(S_1 - S_2) \cdot (U \times W)}{V \cdot (U \times W)} V$$

By using the scalar triple product identity, $a \cdot (b \times c) = c \cdot (a \times b)$, the commutative property of dot products, and a cross product identity $a \times b = -b \times a$ these points can be simply defined as:

$$P_1 = S_1 + \frac{((S_2 - S_1) \times V) \cdot W}{W \cdot W} U \tag{2.30}$$

$$P_2 = S_2 + \frac{((S_2 - S_1) \times U) \cdot W}{W \cdot W} V \tag{2.31}$$

which is easily implemented in Matlab. The position of the particle is then estimated as the midpoint between P_1 and P_2 and an error estimate can be obtained by taking the norm of $P_2 - P_1$ and dividing by 2. Other formulations are also possible, see e.g. [48, 74, 76]

Particle Tracking Velocimetry [77]

Particle Tracking Velocimetry is one of the oldest particle based quantitative imaging methods. A fluid is seeded with small particles made out of a suitable, neutrally buoyant material, and imaging techniques can track the movement of these particles over time as the fluid moves. It relies on the simple and fundamental definition of velocity:

$$\mathbf{u} = \frac{d\mathbf{x}}{dt} = \lim_{\Delta t \to 0} \frac{\Delta \mathbf{x}}{\Delta t} \tag{2.32}$$

in which the change in position of a particle, $\Delta\mathbf{x}$, is determined through imaging at a known time interval, Δt. Individual particles are thus tracked, making the technique Lagrangian in nature, as opposed to PIV which is Eulerian and measures the velocity field at a fixed position over time. Consequently, both velocity and acceleration of the particles, and thus the flow, can be obtained through PTV analysis. The flow can then be visualised through pathlines of individual particles.

As the flow is characterised based on movement of particles suspended in the fluid, the accuracy of the method is by definition reliant on how well the particles follow the flow. In general, the smaller and closer to neutrally buoyant the particles are the less deviation there will be. This is therefore a challenge in XPTV, given the necessary properties of the particles. The equation of motion for a particle moving with a flow becomes complicated quickly, as a particle is subjected to steady and unsteady (viscous) drag, net pressure gradients, non-uniform and non-steady flow effects (see e.g. Basset history integral) as well as added mass effects [49]. The Basset-Boussinesq-Oseen equation is a special case of a general equation of motion for small particles and can be solved in order to calculate a particle's movement through a fluid. Fortunately, due to the small size of the particles, many of the smaller effects can usually be neglected. An alternative perspective is therefore often taken in order to quantify how well the particles follow the flow, namely by considering how quickly the particles adjust to changes in the flow.

The particle Reynolds number, Re_p describes, as previously, the ratio of inertial to viscous forces, but based on the characteristic length scale of the particle, d_p, and is defined as:

$$Re_p = \frac{V d_p}{\nu} \tag{2.33}$$

where $V = U - u_p$ is the velocity of the flow relative to the velocity of the particle, u_p. Using this definition of the relative velocity a simplified equation of motion for a spherical, neutrally buoyant particle can be written in terms of a general drag force based on a drag coefficient, C_D [16], as:

$$m\frac{du_p}{dt} = \frac{1}{2} C_D \pi \frac{d_p^2}{4} \rho(V)|V| \tag{2.34}$$

substituting the mass, $m = density \times volume = \rho_p \pi \frac{d_p^3}{6}$ and dividing through results in:

$$\frac{du_p}{dt} = \frac{18\mu}{\rho_p d_p^2} \frac{C_D Re_p}{24} V \tag{2.35}$$

The factor $C_D Re_p/24$ approaches unity for low Reynolds numbers, i.e. Stokes flow. The first factor has dimensions of reciprocal time and is therefore commonly used

to define the particle relaxation time:

$$\tau_p = d_p^2 \frac{\rho_p}{18\mu} \tag{2.36}$$

This allows for a definition of the Stokes number, which compares the particle response time to a characteristic time of the flow field. For a turbulent flow this is the Kolmogorov time scale, if these scales are of interest. Hence:

$$Stokes\ number = \frac{\tau_p}{\tau} \tag{2.37}$$

Other time scales can be chosen appropriately in order to quantify a particles ability to follow the flow at larger scales. A more general time scale can be defined by a characteristic velocity scale, U, and a length scale, L, so that

$$Stokes\ number = \frac{\tau_p U}{L} \tag{2.38}$$

The Stokes number circumvents the need to calculate a particle Reynolds number, as determining the relative velocity is dificult, given that the flow velocity is unknown, and is what is attempted measured using particle tracking.

Depending on the flow and particle characteristics, density differences may have a significant effect on the particles motion. The net gravitational force on a particle submerged in a fluid is given by

$$F_g = (\rho - \rho_p) V_p g \tag{2.39}$$

where V_p is the volume of the particle and g gravity. The force is thus directly dependent on the difference in density of the fluid and the particle. Throughout the literature this is sometimes used in the definition of the Stokes number [11]. A new definition of the relaxation time can be derived by considering the terminal velocity around a sphere for Stokes flow. Using Stokes' drag law, $F_D = 6\pi\mu V_p d_p/2$, [5] and balancing with the net gravitational force results in a relaxation time of

$$\tau_p = d_p^2 \frac{\rho_p - \rho}{18\mu} \tag{2.40}$$

such that the terminal velocity is $\tau_p g$. Naturally, this will affect the resulting Stokes number, and as with any non-dimensional number care must therefore be taken if comparisons are made. None the less, the definition not reliant on the fluid density appears to be more widely used, and particles are generally considered to follow the flow at the scale used for determination of the Stokes number if the value is $\ll 1$.

A PTV analysis will first require a particle detection algorithm, allowing for determination of the particle positions in a digital image, and a particle pairing algorithm, allowing for pairing of individual particles between images from time step to time step. The former is often accomplished by thresholding of the image in order to determine what is, and what is not a particle. When particles have been located, an issue that arises is that of peak-locking. The centre, or peak in terms of intensity, of the particle is locked to a single pixel which reduces accuracy. This

[5] Note that the general drag force reduces to Stokes' drag force for a spherical particle if $C_D = 24/Re$

issue is therefore commonly solved through curve fitting across the pixels covered by the particle using the relative pixel intensities. For spherical particles a Gaussian peak fit is often used and allows for determination of the displacement peak to sub-pixel accuracy. It is therefore important that the particles cover several pixels in the images.

Particle pairing may encompass a wide variety of algorithms. In the early days of PTV the main method of pairing was through sparse seeding density and pairing of the particle with the nearest position in the next time step. Computational methods have been developed which improve on this, and the low particle density requirement has been somewhat relaxed, although densities lower than in PIV are still the norm. PIV analysis may itself be used as a starting point for PTV analysis by providing a velocity field which can be used to predict an estimated particle position. Modern algorithms often depend on cost functions, which are based on individual particle factors such as size, intensity, velocity, history and shape, and pairing is performed through minimisation of this cost function from one image to another. For the 3D PTV analysis performed in this thesis, particles also had to be paired between the two radiographic projections in order to correctly determine the 3D positions.

The overall algorithm for the XPTV technique used is then as follows:

1. X-ray imaging giving projections in the $x - y$ and $x - z$ planes.
2. Determination of particle position in the resulting projection images.
3. 3D reconstruction of the 3D particle positions in a global coordinate system.
4. Particle pairing over subsequent time steps and velocity calculation in 3D.

A comprehensive walkthrough of the method used is presented in section 4.3.1. Altogether, a 3D XPTV setup introduces several potential sources of error and challenges, both through x-ray generation, detection and behaviour, as well as particle behaviour and general spatial and temporal resolution issues, and significant effort can be dedicated to investigating these issues. The results obtained from the experiments performed as part of this thesis may be used to comment on some of these topics, however an extensive validation of the setup used has not been performed, in which results are compared with a known and exact solution in order to quantify the accuracy.

Chapter 3

Experimental Setup

A modular setup was created to allow for easy exchange of components. The flow was gravity driven and consisted of a 10 litre container elevated roughly 2 metres above the aneurysm model, with a 3 litre container used to catch the water. Although other driving mechanisms were considered, i.e. pumps, gravity driven flow was chosen for its simplicity, and to avoid unnecessary noise for the acoustic measurements. Rubber tubing with an inner diameter of 6 ± 0.2 mm was used to link the various parts and an adjustable valve was fitted for control of the flow output. A minimum tube length of 200 diameters was used between the valve and the aneurysm model in case of flow disturbances through the valve, and sharp bends avoided in order to keep the Dean number sufficiently low. Flow output was measured through the use of a scale and a timer, allowing for the determination of mass flow rate, $Q = \Delta mass/\Delta time$, and consequently parent artery Reynolds number for the aneurysm models was calculated. The mass flow rate can also be written as

$$Q = \rho \cdot U \cdot A_c \tag{3.1}$$

where U is the average flow velocity through the cross-sectional area; $A_c = \pi D^2/4$ for a cylinder. Hence $U = 4Q/(\rho \cdot \pi D^2)$ and the Reynold's number of a cylindrical parent artery is given by

$$Re = \frac{4QD}{\rho\nu\pi D^2} = \frac{4Q}{\mu \cdot \pi D} = \frac{4 \cdot \Delta mass}{\mu \cdot \pi D \cdot \Delta time} \tag{3.2}$$

Water was used as the operating fluid, and standard values for the density and dynamic/kinematic viscosity were used for all calculations ($\mu = 1 \times 10^{-3} Pa\,s$, $\rho = 1000 kg/m^3$, $\nu = 1 \times 10^{-6} m^2/s$).

Two aneurysm models were used based on three dimensional imaging by CT angiography [31]. These were each 3D printed in two different materials and sizes. Material names (and specifications) were not available a the time of writing, but have been assigned based on their colour for differentiation. Images of the models can be seen in Appendix B and parent artery dimensions are presented in table 3.1. Model A was a bifurcation type cerebral aneurysm, while model B was a sidewall type. Care was taken to ensure air bubbles were not stuck inside the models before experiments were performed. Extensions were fitted to the aneurysm outlets and merged through a y-connector to guarantee an equal pressure difference over the two outlets, which ensured flow through the model was consistent and not dependent on orientation.

Name	Material	Parent Artery Diameter (mm)
A1	Yellow	7.0 ± 0.1
A2	White	7.0 ± 0.1
A3	White	7.0 ± 0.1
A4	Yellow	4.5 ± 0.1
A5	White	4.5 ± 0.1
B1	White	6.1 ± 0.1
B2	Yellow	6.1 ± 0.1
B3	White	4.0 ± 0.1
B4	Yellow	4.0 ± 0.1

Table 3.1: The naming convention of the 3D printed aneurysm models and their specifications. Two models, A and B, were made using two different materials and in two different sizes.

3.1 Acoustic Method

Data acquisition for the acoustic method was performed using a National Instruments myDAQ and an in-house built amplifier previously determined to be linear [90]. This amplifier included an analogue second order low pass filter, limiting measured frequencies to less than 4096Hz, and the sampling frequency was set to 16384Hz. Although a sampling frequency of 8192Hz was technically required per the sampling theorem, the higher frequency was used partly to prevent aliasing caused by imperfections in the filter, and partly to more quickly acquire a large enough set of data points to allow for robust post-processing. The bit depth was 16 bits, with a range of -2 to 2V. The contact microphone used remains a possible source of error due to lack of technical specifications related to its linearity. The combined set-up was controlled by a LabView programme, which can be found in appendix C.

3.2 3D XPTV Method

A schematic representation of the stereographic x-ray setup can be seen in figure 2.4. The distance from the origin to detector 1 and 2 was 110mm and 100mm, respectively. The distance from source 1 to detector 1 and source 2 to detector 2 was 636 mm and 552 mm, respectively. Two 400W x-ray sources were used, with a voltage range of 20-100kV and current range of 0.5-10mA, resulting in x-rays emitted in a cone shaped beam from a 0.5mm focal spot [12]. The x-ray generator settings were set to 40kV and 4mA in the FlowCapture software that controlled the x-ray machine. In the resulting 3D reconstruction it was assumed that the x-ray centrelines hit their corresponding detectors perfectly in the middle, and that the source/detector pairs were perfectly in plane. Furthermore the 0.5mm focal spot was estimated as a point source. The detectors had a sensitive area of 114.9mm × 64.6mm, with a 1536 × 864 pixel matrix, giving a pixel size of 74.8 μm. 1×1, 2×2, and 4×4 pixel binning was possible. 2×2 pixel binning was used for all measurements at a frame rate of 155fps with 6.5ms exposure time.

The seeding particles used for PTV analysis consisted of an outer lead shell with a hydrogen gas core to allow for neutral buoyancy. This allowed for detection of the

particles through x-ray imaging whilst near-neutral buoyancy ensured the particles followed the flow. The particles were, however, far from ideal, both in terms of size, shape and density, and the extent to which they followed the flow is therefore more closely examined in chapter 4. The particles were added to the flow through the use of a syringe pump connected to the tube immediately after the flow control valve, using a y-connector. This prevented particles from getting stuck in the valve, and particles were caught as they left the system using a sieve. Some control over the amount of particles put into the flow was therefore possible, and the low flow rate of the syringe pump did not affect the flow significantly. Any fluid added was accounted for in determination of the flow rate.

3.3 Experiments Performed

Several tests were performed in an attempt to validate the system and isolate sources of error. The flow rate reduction caused by a steady decrease of water in the container was tested by measuring the time required for 1000ml of water to pass in three subsequent trials without water refill or removal and was repeated three times. A test was also performed in which the number of data points used in the spectral analysis was steadily increased until convergence was observed, in an attempt to verify the consistency of the method. Microphone placement could then be tested by considering three different attachment points. Three trials at the same Reynolds number were performed for each position. Additionally, three different types of connections between the rubber tubing and the aneurysm model entry were tested, in case of unwanted turbulence generation at this point. The connectors were investigated both acoustically by comparing the PSDs at similar Reynolds numbers, and by use of x-rays through imaging of the flow through the transition. Finally, the flow through a long, cylindrical pipe was measured using the acoustic method in order to allow for comparison with a previously well documented case. The microphone was placed 200 diameters past the cylinder entry in order to allow adequate time for any flow disturbances to settle. The results of these tests are presented in chapter 4.1.

In order to detect when transitional flow behaviour emerged by use of the acoustic method, a high initial flow rate was measured and subsequent trials performed whilst gradually decreasing the flow rate. This process was repeated up to 3 times, with additional measurements taken at certain flow rates if necessary, particularly near the critical Reynold's number. Measurements were taken of both model types, and for the two different materials and sizes. For all acoustic measurements the background noise at zero flow rate was also recorded at regular intervals, in order to obtain adequate basis for comparison of PSDs. A separate reflection on this has been included in section 4.1.3.

A similar approach was taken for the XPTV measurements, however flow rates were chosen based on the acoustic results to allow for comparison. In particular, measurements were performed under the critical Reynolds number, Re_{crit}, found from the acoustic method for the given model, as well as near but over Re_{crit}, and significantly over Re_{crit}.

Additionally, as an alternative to the lead-hydrogen particles used, CO_2 bubbles were investigated as a possible seeding particle by using carbonated water as the fluid, allowing bubbles to form as the fluid passed through the system.

Chapter 4

Results & Discussion

4.1 Validation

4.1.1 Flow Rate and Determination of Re

The gravity driven flow system generated a maximum flow rate of roughly 20 g/s, corresponding to Reynold's numbers in excess of 3000 for all the models tested. Since the flow relied on a pressure difference directly related to the height of the water column the consistency of the flow was considered, as the relative height decreased over time as the water flowed. The results in table 4.1 indicated that for every gram of water that flowed, the next gram took 0.001 seconds longer, and the measured flow rate was an average of a slowly decelerating flow. With the caveat that such a small difference was subject to uncertainty in the manual timing, and as most measurements were on the order of a few hundred grams over the course of 60 seconds, this effect was therefore negligible compared to other error sources.

Inaccuracy was experienced in the determination of the Reynold's number caused by manual timing of the flow. The associated error was estimated as ± 2 seconds, translating into roughly $\pm 3\%$ for a 60s trial. The scale was accurate to the nearest gram, and an uncertainty of ± 1g for the trials performed at the lowest Reynolds numbers (mass flows of $\sim$50g) translated to $\pm 2\%$. For the majority of trials with higher mass flows the effect of scale inaccuracies was decreased. In most cases trials at low flow rates were performed with an increased duration to counter this. As the total mass flow increased, uncertainties caused by the scale became increasingly negligible, whereas uncertainties caused by the pressure drop became more important, and a balance between the two was therefore attempted. Finally, the uncertainty in the parent artery diameter measurements resulted in a further uncertainty of $\pm 2\%$.

Overall, the reported Reynolds numbers are therefore presented with a $\pm 10\%$ error estimate. To counter this three trials at the same Re have usually been performed and the resulting PSDs averaged. The uncertainty could be significantly reduced by using a modern scale, capable of recording the weight over time automatically, as both the exact time and mass of the flow could be recorded, or by using a flow meter.

Run	1	2	3
Average time (s)	86	87	88

Table 4.1: Time required for 1000g of water to flow through the system.

4.1.2 Consistency of PSDs using Welch's Method

Before further analysis of the acoustic measurements was performed the consistency of the power spectrum densities estimated through Welch's method was verified, with the most important variable being the number of data points in the recorded signal. 8 segments with 50% overlap and Hamming windows were used in Welch's method for all PSD estimates. Figures 4.1 and 4.2 show the development of a selection of PSD plots as more data points were added for two separate measurements. The difference between 2^{18} and 2^{19} data points was minimal for both, with any differences most noticeable at the lower frequencies, due to lower relative resolution in the logarithmic scale. 2^{18}, or 262144, data points was therefore selected as the standard. This resulted in a frequency vector of 32769 data points with values ranging from 0 to 8 192Hz at 0.25Hz intervals, in line with the sampling frequency of 16384Hz.

At a sampling frequency of 16384 Hz, 2^{18} data points was equivalent to 16 seconds of recorded data. The increased accuracy in the PSD estimate achieved by doubling this was in reality usually lost, as a 32s recording was highly likely to include significant unwanted noise, caused by random disturbances such as doors being closed in the building, or people walking above the lab. Increasing the sampling rate further could allow for more data points in the same amount of time and possibly even more accurate PSD estimates.

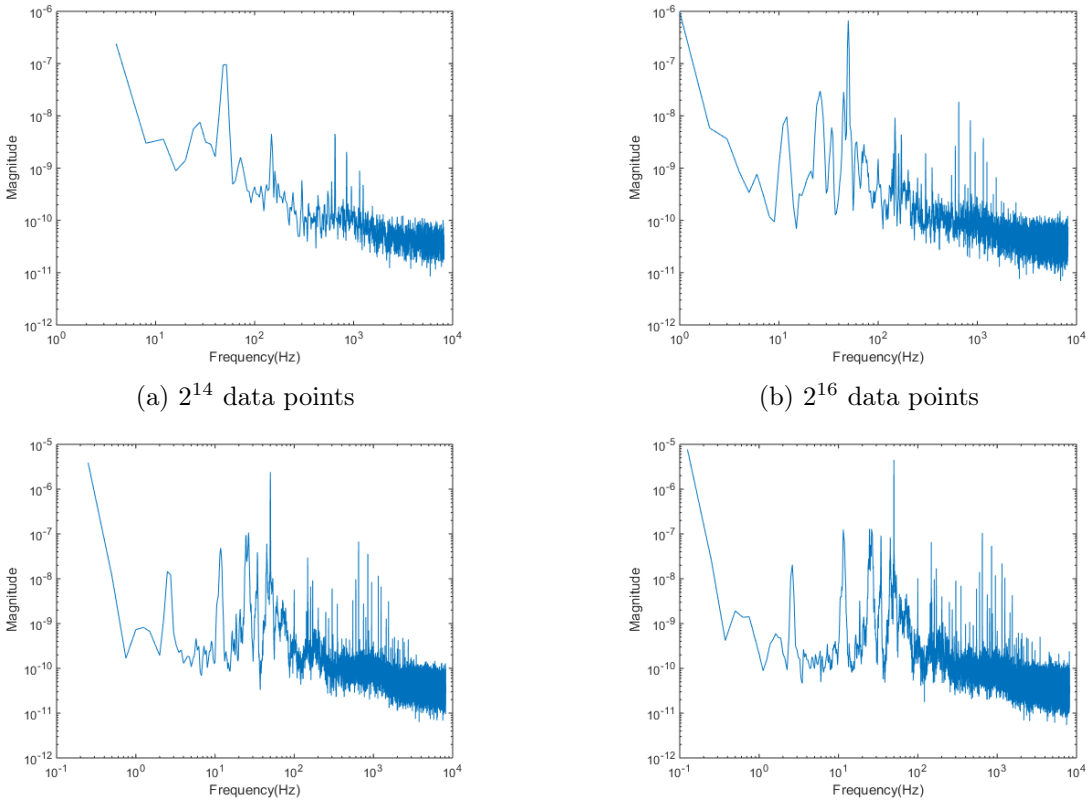

(a) 2^{14} data points

(b) 2^{16} data points

(c) 2^{18} data points

(d) 2^{19} data points

Figure 4.1: PSD estimates obtained using different signal lengths of measured noise.

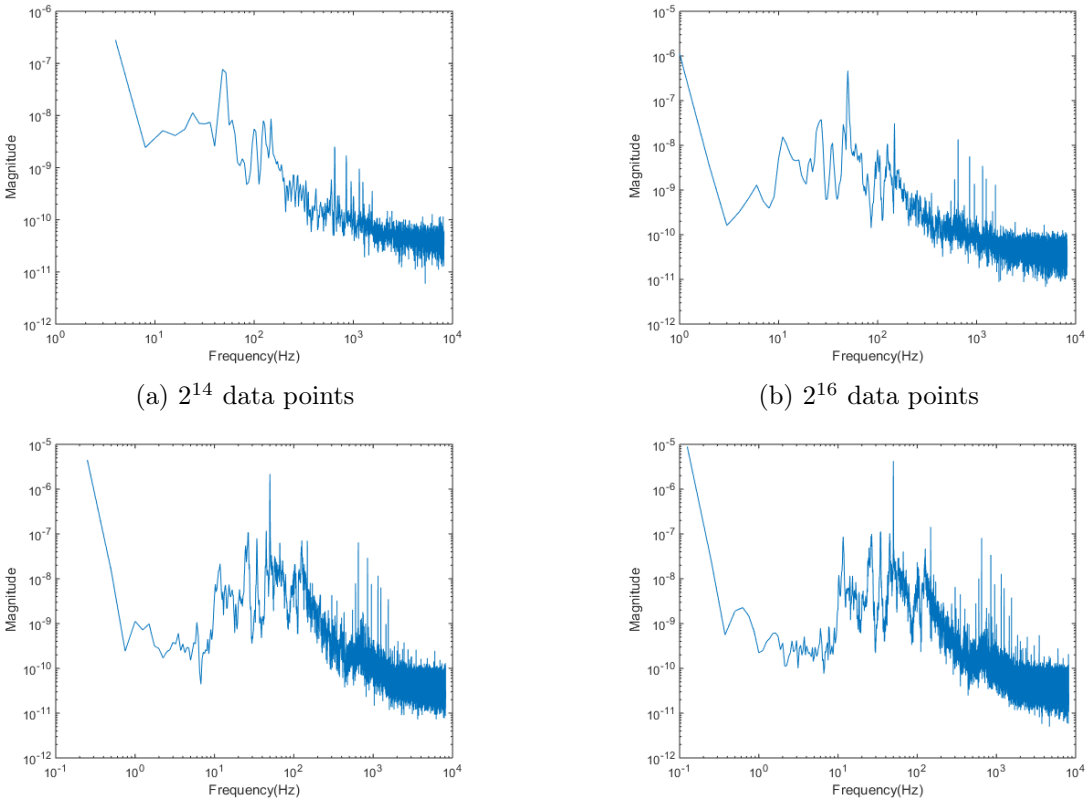

(a) 2^{14} data points

(b) 2^{16} data points

(c) 2^{18} data points

(d) 2^{19} data points

Figure 4.2: PSD estimates obtained using different signal lengths of a measured flow.

4.1.3 Background Noise

The resulting PSDs of four different noise recordings taken over the course of measurements performed on model A2 can be seen in figure 4.3. The PSDs all displayed the same general shape, and variations were minimal. The magnitude of the PSDs at frequencies greater than roughly 4000 Hz indicated the true zero level, as these frequencies were filtered by the analogue low-pass filter. Any small spikes above the cut off frequency were therefore due to imperfections in the filter, or artefacts from the PSD estimation. Small peaks can be seen around ∼1200Hz and ∼200Hz whereas the majority of the background noise lies below 100Hz. In particular, the highest peak lies at 50Hz, and corresponds to electrical noise.

This consistency therefore allowed for accurate comparison of PSDs even at low Re. Noise measurements were performed before, during and after all experimental sessions to ensure an accurate comparison based on the noise levels at the time. Excessive noise events, such as a doors closing, occurred randomly, and could usually be heard audibly. Measurements taken at the time were either discarded, or unaffected data points selected if a continuous signal of 16s length could be found. None the less, it is unlikely that all random noise events were avoided, and further improvements could be made by performing the measurements in a sound proof room, or adding noise insulation around the aneurysm models and microphone to further reduce noise. As the microphone was particularly sensitive to vibrations, using an anti-vibration table may also be beneficial. None the less, a consistent point of comparison could be made for the experiments performed, although taking steps

to decrease the noise in potential future experiments will allow for more accurate comparisons when minor fluctuations appear, which may have been drowned out by the background noise for the present experiments.

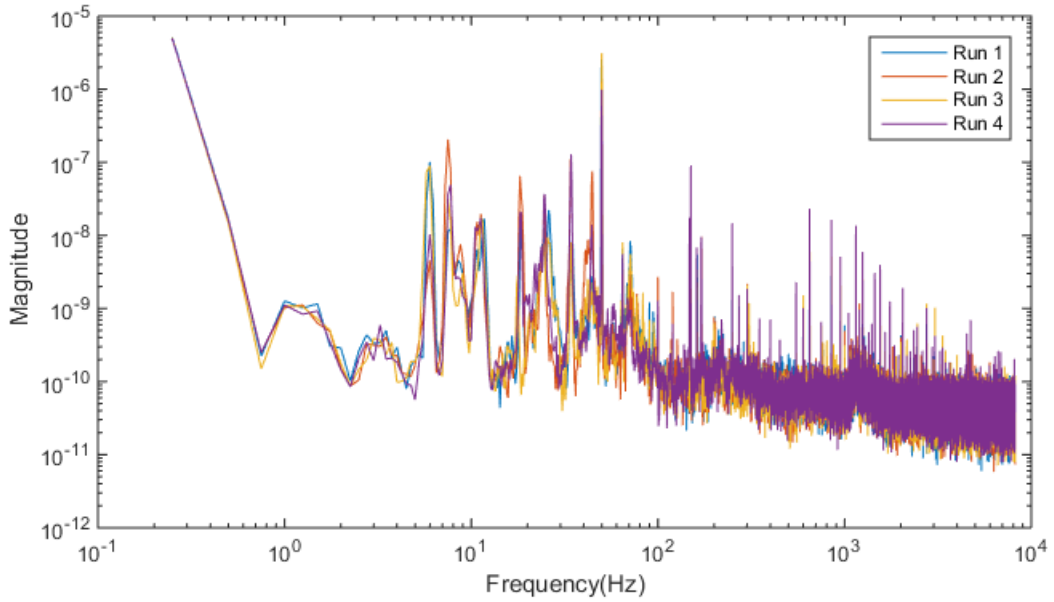

Figure 4.3: The PSD estimates from four different noise recordings show clear similarities.

4.1.4 Microphone Position

Three different microphone positions were tested with flow through model A2 at Re∼1175. An image showing the positions can be seen in appendix B. Position 1 was at the front end of the aneurysm bulge directly opposite the inlet. Position 2 was on the back side of the bulge. Position 3 was near the inlet. The mean amplitude of the signal for the three locations was found by taking the absolute value of the signal series and averaging, before averaging again over the three trials performed at each position. The results can be found in table 4.2. The detected signal from position 1 had the greatest mean amplitude and the highest signal to noise ratio (SNR). Position 2 had the lowest amplitude of noise. The PSDs averaged over three runs for the three positions can be seen in figure 4.4. Although generally similar, some discrepancies were apparent through the positions having magnitude drops or peaks at frequencies where the other positions did not. Most notably position 3 showed higher magnitudes at low frequencies and went to zero at a lower frequency than positions 1 and 2. Several factors may explain these discrepancies. Firstly, the long, rectangular shape of the microphone meant only a part of the microphone

Position	Mean Signal Amplitude (mV)	Mean Noise Amplitude (mV)	SNR
1	10.5	2.4	4.375
2	9.5	2.2	4.318
3	9.7	2.7	3.556

Table 4.2: Signal and noise properties for three different microphone positions.

was in contact with the model surface, and variations in the contact area may have resulted in a varied sensitivity to vibrations from position to position, and/or increased sensitivity to noise. Secondly, the signal picked up by the microphone was possibly related to the physics of the flow. As pressure differences are produced due to fluctuations in the flow the microphone's ability to detect them will be dependent on the amount of attenuation the pressure fluctuation has experienced before it reaches the sensor. In other words, the further away the microphone is from the origin of the pressure difference, the less likely it is to be picked up. Based on the present results, this may indicate that fluctuating flows were present near position 1 and 2, i.e. near the edge of the bulge opposite the inlet. As position 3 was further away from this point, the weakest, highest frequency fluctuations may have been attenuated to the point where they were indistinguishable from the background noise. This concept of gathering information about the flow based on altering the sensor position may be worthy of investigation in the future, and experiments could potentially be performed with several microphones attached to the aneurysm model simultaneously. In order to do so a microphone with a smaller contact area would be beneficial, and would also address any discrepancies caused by an inconsistent contact area between different positions.

Position 1 was chosen as the standard microphone placement for future measurements on model A based on the higher SNR and the possibility of fluctuations located in this part of the aneurysm. A similar position, i.e. one on the bulge, was used for model B.

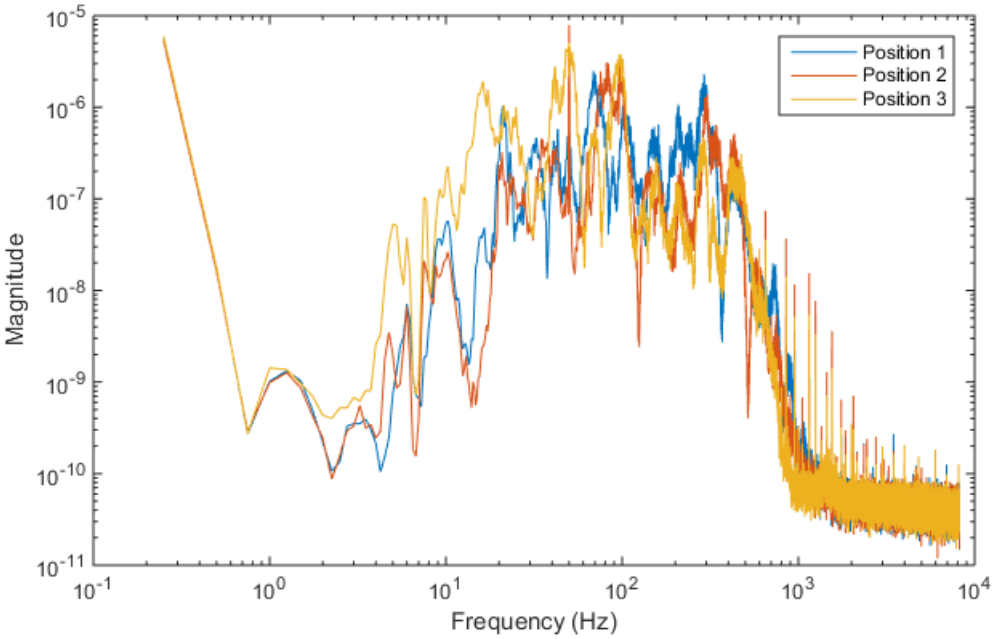

Figure 4.4: Resulting PSDs from three different microphone placements.

4.1.5 Tube to Model Connections

The connection between the plastic tubing and the aneurysm model was identified as a potential source of error, as a rough transition could disturb the flow and induce fluctuations unrelated to the aneurysm geometry. The three different connections

used to evaluate this effect are shown in appendix B. The first type used a thin, tapered 3D printed cylinder matched to the inner diameter of the aneurysm model, and required the aneurysm inlet to be expanded in order to accommodate it and allow for a smooth transition. The standard 6mm plastic tubing could then be inserted over the tapered 3D printed tube. The act of drilling into the aneurysm inlet in order to fit the tapered extension ran the risk of destroying the models, so the second type used a larger tapered 3D printed cylinder whose outer diameter was matched with the outer aneurysm inlet diameter, and therefore required attachment using a thicker plastic tube. The final connector type directly attached the 6mm plastic tubing to the aneurysm inlet, in a hope that the near match of diameters would sustain a smooth flow at the relatively low Re considered. As the inner diameter of the plastic tubing was slightly smaller than the aneurysm inlet, the flow was not affected by edges protruding into the flow, but vortex formation was conceivable due to the rapid, but small, increase in cross-sectional area.

A PSD comparison of the three connector types at Re∼850 can be seen in figure 4.5. Noise levels were consistent throughout the measurements. Similarities were clear in terms of the general magnitude of the signal and the rate and frequency at which they went to zero, but discrepancies were also observed. For connector type 2 a clear increase in magnitude was apparent at roughly 200Hz and below 10Hz. Type 1 and 3 displayed greater similarities, although type 3 had a peak near 80Hz not present for the other connector types. Similar trends remained consistent at other Reynold's numbers, and it is therefore plausible that the connection between the tube and the aneurysm may have had some effect on the flow, although minor differences may also have been caused by small variations in microphone placement when the models were exchanged. This potential source of error could be avoided in the future by 3D printing the aneurysm models with a longer parent artery inlet modified appropriately to be connected to the flow as smoothly as possible.

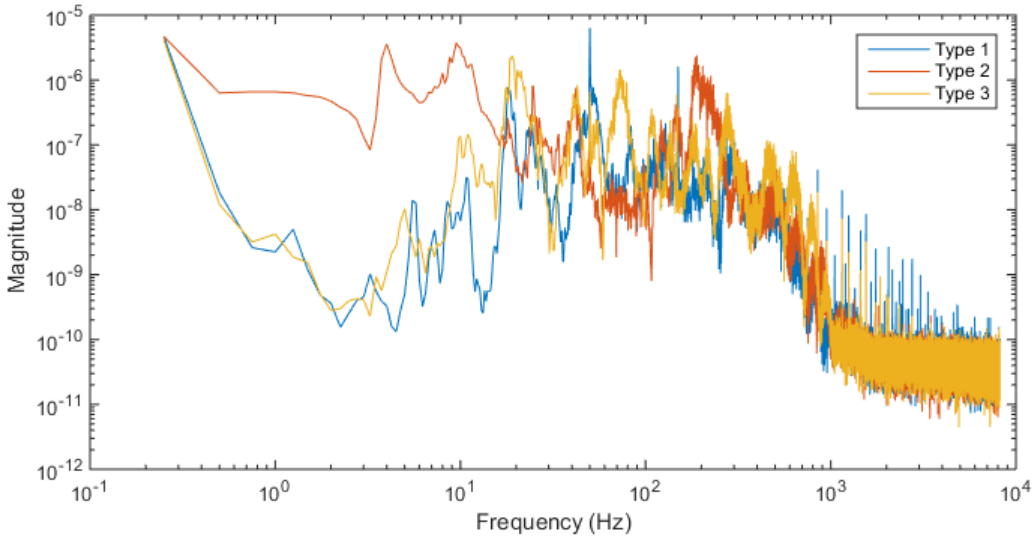

Figure 4.5: PSDs from three different connector types at Re∼850.

For the purpose of presentation a smoothing filter could be applied to the PSDs. A filtered version of figure 4.5 can be seen in figure 4.6. Filtration has been performed in order to keep as many features as possible, whilst still providing a cleaner look

for visual comparison. Features in the lower frequencies suffer most severely from filtration due to lower resolution in the logarithmic scale, and in cases where an accurate comparison is necessary PSDs are presented without filtration. A third order Savitzky-Golay method with a frame size of 31 data points was used [67].

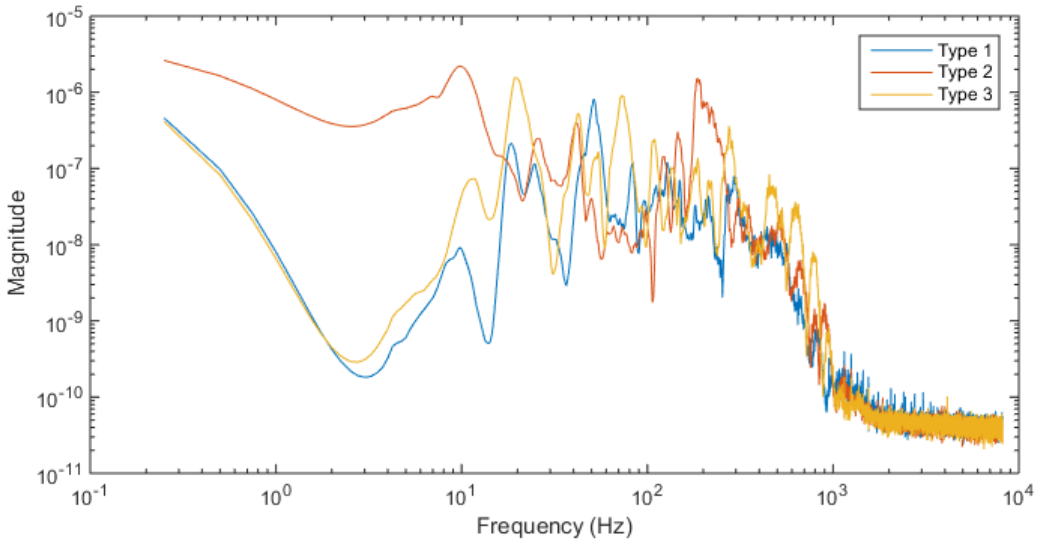

Figure 4.6: Filtered PSDs from three different connector types at Re∼850.

Based on the acoustic tests the extent to which the connection affected the flow remained unclear, and further investigation was performed using x-ray imaging. No clear indications of fluctuating flows could be seen for any of the connector types, however this may have been a result of the seeding particles used and their inability to follow small scale flow patterns, a topic which is further discussed in section 4.3.4. None, the less, x-ray imaging revealed an issue with connection type 2. Due to the larger diameter of the plastic tubing, velocities were proportionally slower in order to maintain the same mass flow rate before accelerating as the 3D printed cylinder tapered down to the inlet diameter. The lower flow velocity caused variations in the particle densities to become more important, leading to attachment of particles along the tube/cylinder wall due to excessive buoyancy or lack thereof. Figure 4.7 shows an x-ray image of particles stuck to the wall of the tube.

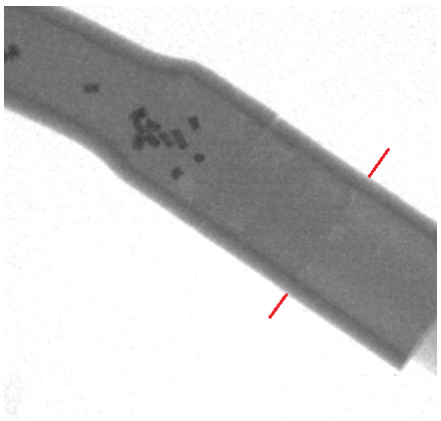

Figure 4.7: X-ray imaging of particles stuck in connector type 2. The red lines indicate the transition from the 3D printed, tapered cylinder to the aneurysm model inlet.

Because of this and the overall increase in magnitude seen in the PSDs, type 2 was discarded for further use. Type 1 and 3 appeared equally good (or bad), and were therefore used for the experiments performed. As only one sample of model B was available in each material it was decided that using connector type 1 which required drilling of the inlet was not worth the risk of destruction of the model. The inlet diameter of model B (6.1mm) was closely matched with the plastic tubing diameter (6.0mm) and it was therefore assumed that the transition would be sufficiently smooth.

4.1.6 Acoustic Measurement of Flow in a Cylindrical Pipe

The main area of ambiguity for the acoustic measurements was centred around not knowing the exact cause of the measured pressure fluctuations. Attempts to control extraneous flow disturbances by ensuring adequate distance between points of disturbance and the model, and investigating the effect of the transition from tube to model, did not satisfactorily ensure that the setup did not create unwanted fluctuations. By applying the method to a well studied case, comparisons could be made which may allow for a better understanding of the results of an unknown case. This was accomplished by measuring the flow through a cylindrical pipe. First, measurements of the flow through the rubber tubing used in the experimental setup were performed, with the microphone placed 200 diameters away from any potential disturbances to the flow. The filtered PSDs of various Reynold's numbers can be seen in figure 4.8. Transition to turbulence in cylindrical pipe flow is expected around Re$\sim$2000, however a clear energy cascade indicative of fluctuations was present even at Re$\sim$1000. The PSD was similar to the background noise level at Re$\sim$450. This apparent deviation from theory was speculated to be caused by the elasticity of the tubing and/or the fact that the tubing on which measurements were performed hung freely from the water container. Both of these factors may have contributed to an increased sensitivity to flow induced vibrations. Additional measurements were therefore performed on a hard, plastic cylindrical pipe with an inner diameter of $\sim$7mm and a wall thickness of 2.5mm. The filtered PSDs are shown in figure 4.9. The energy cascades were less prominent and the differences from the noise level less distinct. Re$\sim$2850 showed the clearest energy cascade, and Re$\sim$2300 displayed comparatively less deviation from the noise level, as expected. However, once again a lower Reynolds number flow, Re$\sim$1450, unexpectedly displayed deviation from the noise level, although not as clearly as for the rubber tube.

It should be noted that significantly more background noise was present for the hard pipe measurements, possibly affecting the accuracy of the results. The background noise was directly related to the presence of water in the long cylindrical pipe, as noise levels similar to the other measurements were observed when the pipe was empty, and the water filled pipe therefore appeared to act as an antenna for nearby noise. A comparison with the noise level was also made harder due to the weaker amplitude of the fluctuations recorded, effectively lowering the SNR. Due to the difference in materials it was also difficult to determine whether or not the weaker pressure fluctuations were representative of the flow, or if the vibrations were less able to propagate through to the microphone. In particular, several discontinuities in magnitude at specific frequencies were observed, e.g. at $\sim$80, $\sim$200 and $\sim$400 Hz. These measurements therefore only provided an indication of how the results

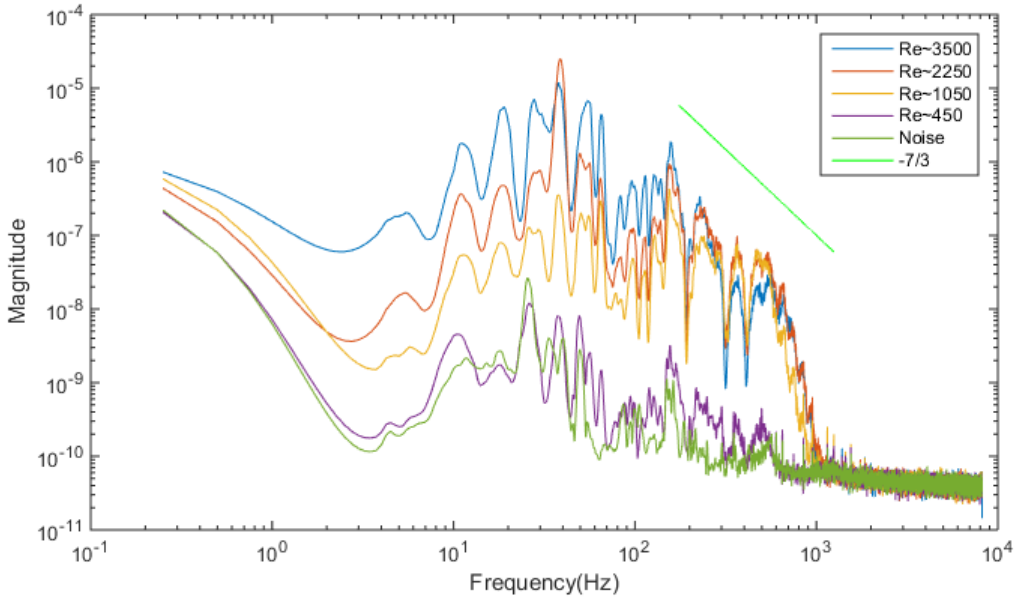

Figure 4.8: PSDs of flow through rubber tubing at various Re

obtained from the aneurysm models compared, although the general trend showed the appearance of fluctuations at a lower than expected Reynold's number. Whether this was a result of faults in the experimental setup, or physically accurate, remains unclear. Several factors come into play which have not been accounted for, such as differences in material, thickness and other physical properties. This may not only have lead to changes in the flow, but pressure-difference propagation may have been significantly altered. A cylindrical pipe made out of the same material as the aneurysm models would therefore be preferential, and allow for a more robust comparison with a known flow.

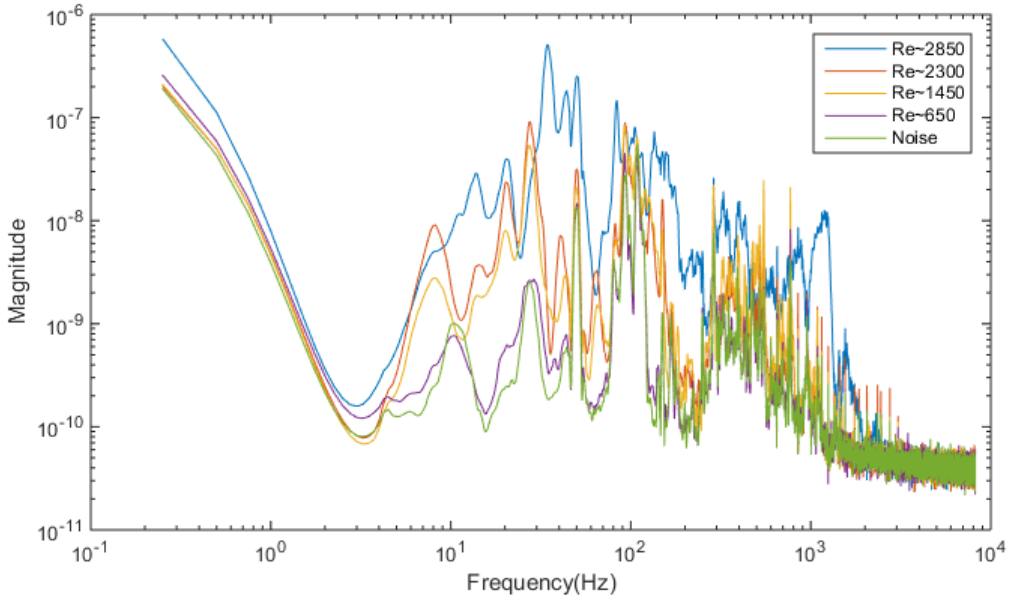

Figure 4.9: PSDs of flow through hard plastic tubing at various Re

4.1.7 Turbulence Generation and Pressure-Velocity Coupling

Based on the results presented thus far a physical interpretation of the acoustic measurements requires elaboration on the concepts of turbulence generation and the pressure-velocity relationship of a flow. Turbulence generation is complex, and a complete understanding potentially implies a complete understanding of turbulence in general, and is therefore currently out of reach. Several mechanisms have been examined throughout the literature, and generally turbulence is accepted as produced by the interaction of the fluid with geometry, by the loss of energy due to viscosity, by density variations caused by temperature, or other factors, such as changes in velocity, or all of these at once [53]. Understanding turbulence generation is therefore further complicated by the fact that it is highly individualised for different flows. As an example, some turbulent flows are characterised as "free" and are remote from solid boundaries and usually surrounded by non turbulent flow, whereas other turbulent flows may be directly related to interaction with a solid boundary. Turbulent flow in pipes has been the subject of extensive research due to wide use in real situations, and comparative simplicity. In short, the transition to turbulence is thought to originate at the walls, and in general shear flows are thought triggered into a turbulent flow regime by small perturbations to the flow which grow and develop into larger vortices and chaotic motion [1]. It is because of this that the transition to turbulence in a pipe has been delayed in pipe flows to Re much higher than the typical 2000 by careful control of flow conditions [80]. Conversely, additional disturbances in the flow may lower the critical Reynolds number, highlighting the importance of eliminating this potential source of error in the experimental setup. Although this was attempted for the present measurements, it may be an explanation for the lower than expected critical Reynolds number found for flow through the cylindrical pipe. However, assuming errors in the setup were not significant, other possible explanations must be found for the pressure fluctuations measured at the wall at lower than expected Re.

Description of flow near a wall has, and still largely is, a significant challenge, and consequently a complete understanding of what happens near the wall, particularly inside the boundary layer, has proved difficult. None the less, a combination of hot wire/film anemometry, pressure sensors, and quantitative and qualitative imaging techniques, including PIV/PTV and the use of hydrogen bubbles and dye streaks, amongst others, has resulted in a relatively consistent description of near-wall flow and associated turbulence generation. Of importance is what is commonly referred to as the "burst-sweep cycle". In simple terms, laminar boundary layer oscillations are observed (the "sweep") with intermittent ejection of fluid away from the wall (the "burst"), which disturbs the surrounding flow. Observations have further been made on the topic of "slow" and "fast" fluctuations, and different behaviour in various parts of the boundary layer. [18, 20, 35, 57, 61, 68, 80]

Laminar flows are known to suppress sufficiently small fluctuations [80], and in order for transitional behaviour to occur on a larger scale the flow disturbances must be large enough. Increasing the flow velocity reduces the disturbance size needed to trigger further transitions, and the critical Reynolds number will occur when these two factors combined represent the required conditions for transition. This further

[1] This is somewhat overlooked in classical Kolmogorov theory, as it focuses on high Re flows, and the cascade of energy from large scale to small scale.

explains why the critical Reynolds number may be delayed to much higher than typical values, or triggered earlier by factors such as increased wall roughness. It is therefore possible that the low Re fluctuations measured in the cylinder represent fluctuations near the wall whilst the majority of the flow remains laminar, although this cannot be claimed with any degree of certainty based on the present results.

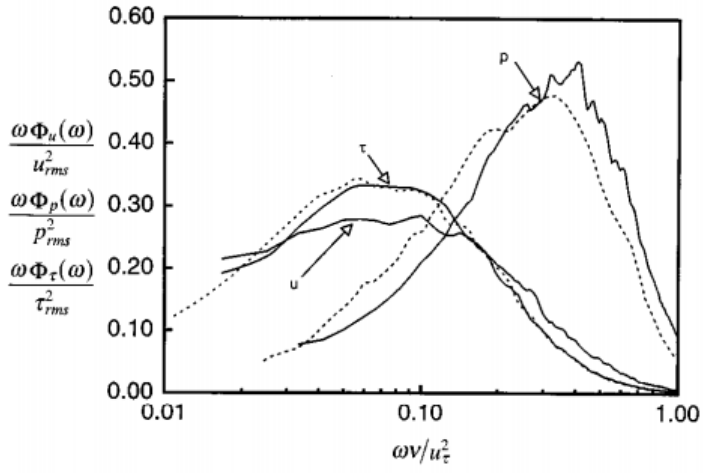

Figure 4.10: PSD comparison of pressure, velocity and WSS fluctuations. Reproduced from [57]

As mentioned in section 2.4.1, the measured wall pressure is a weighted integral of the velocity field above the wall, taking into account both the near-wall fluctuations, and fluctuations further from the wall [57]. Understanding the mechanotransductional effects of the fluctuations, i.e. understanding how the blood, vessels, and cells are affected by pressure related effects and velocity effects (e.g. WSS), and how they respond to fluctuations of different frequencies, is therefore important for the purpose of understanding aneurysm pathophysiology but is beyond the scope of this thesis. However, in order to attempt to quantify the flow further in terms of conventional Kolmogorv scales the correlation between the measured fluctuating pressure and fluctuating flow velocities must be examined. Nepomuceno et al. state that "large positive peaks in the wall pressure are related to accelerations in the streamwise velocity and negative peaks are related to decelerations in streamwise velocity." There is therefore a correlation between pressure and velocity, although the issue of the measured pressure being a combined result of a larger area of the flow remains. Furthermore, ambiguities are increased due to unknown attenuation and propagation of the signal. It is therefore difficult to determine whether the high frequency fluctuations observed represent the Kolmogorov microscales of turublent flow far from the wall, or small, near wall oscillations, or are representative of both. Ideally, the act of Fourier transforming the signal will identify the various frequencies that contribute to the measured pressure signal, so that a frequency in the pressure domain is related to the same frequency in the velocity domain, regardless of spatial origin. Figure 4.10 shows a comparison of the PSDs of measured velocity and pressure (and wall shear stress) performed by Nepomuceno et al. on the boundary layer past a cylinder. Pressure was measured using a small hearing-aid microphone placed flush with the wall, and velocities measured using a hot wire

probe. The pressure and velocity PSDs can be seen to differ in shape, as expected from Kolmogorov theory, but appear to reach their zero levels at the same frequency. For future analysis in this thesis, the maximum frequency of the measured pressure fluctuations is assumed to be directly related to the highest frequency velocity fluctuations, such that the Kolmogorov time scale can be found from the frequency at which the energy reaches the zero level. Inaccuracies caused by attenuation, or discrepancies between pressure and velocity fluctuations may therefore be present, although the assumption should provide a decent estimate of the Kolmogorov scales. Further investigation into the relationship between wall pressure fluctuations and velocity fluctuations in the flow may potentially be beneficial given the non-linear nature of the governing Poisson/wave equation.

4.2 Acoustic Results

4.2.1 Appearance of Fluctuating Flows

Model A

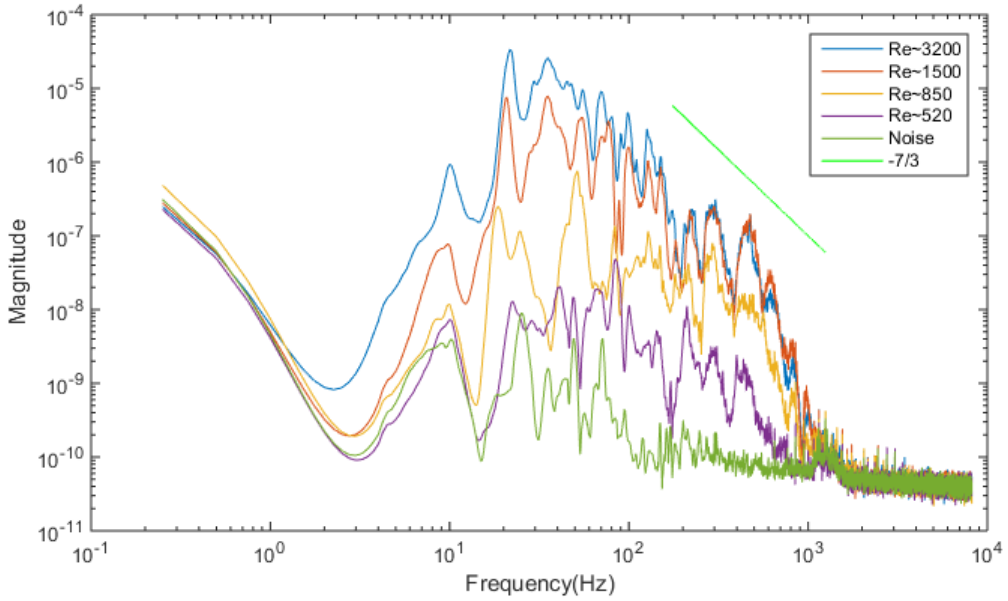

Figure 4.11: PSDs of flow through model A2 at various Re

Figure 4.11 shows the general trend of filtered PSDs as the Reynolds number was decreased for flow through model A2 and connector type 1. The magnitude of the energy cascade steadily decreased with the Reynold's number and significant deviation from the noise level was observed at Re∼520. Figure 4.12 shows a direct comparison of low Re flow PSDs and the noise level PSD. At Re∼130 meaningful deviation from the noise level was absent, as was largely the case for Re∼300, although small deviations may be discerned near 100-300Hz. At Re∼315 the magnitude of these had grown, and at Re∼400 a substantial energy cascade appeared. Based on these observations, fluctuations in the flow possibly appeared as low as Re∼300-315, and were confidently identified at Re∼400. The spectrum reached the zero level at approximately 1000Hz, although this appeared to decrease slightly for lower Re, and

thus lower velocities, and is in line with the behaviour expected from equations 2.15 and 2.14. Approximating this as a Kolmogorov time scale of 1/1000Hz = 0.001s and using equation 2.14, the dissipation rate was determined to be $\varepsilon = 1\ J/(s \cdot kg)$. Using equation 2.13 the Kolmogorov length scale was found to be $\eta = 31\ \mu m$.

The measured sounds/pressure fluctuations have thus been used to characterise the flow in terms of when it separated and began to display transitional behaviour, and the Kolmogorv scales. Further investigations could potentially be done in order to determine other properties of the aneurysm and the flow. As an example, Lees (1984) found a connection between the peak frequency found from spectral analysis of a bruit and residual lumen diameter of a stenosed artery [40], and microphone position has already been mentioned as a possible way of locating fluctuation sources.

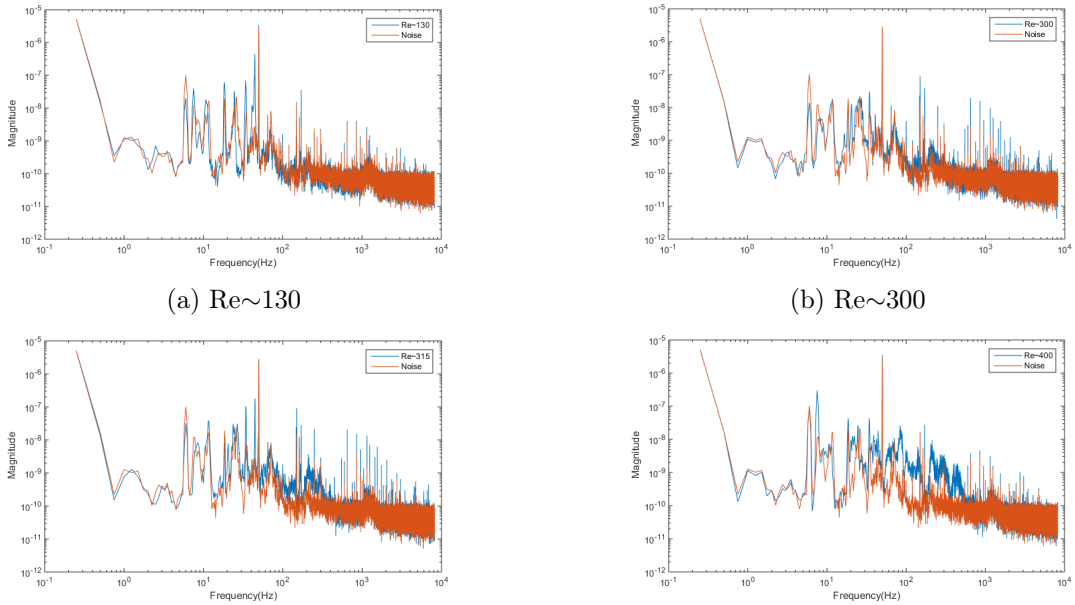

(a) Re∼130 (b) Re∼300

(c) Re∼315 (d) Re∼400

Figure 4.12: Model A: Comparison of low Re PSDs with noise.

Model B

Figure 4.13 shows the general trend of filtered PSDs as the Reynolds number was decreased for flow through model B1 and connector type 3. A decrease in magnitude as Re decreased was once again observed. Figure 4.14 shows low Re comparisons with noise. No discernible difference from the background noise was spotted at Re∼360. At Re∼550 small localised magnitude increases at ∼15Hz and ∼100Hz appeared, although these were within range of variations observed in the background noise level. However, the deviations appeared to grow as the Reynold's number increased to ∼620, and more so at Re∼700, where a somewhat pronounced energy cascade appeared. Based on these observations, fluctuations in the flow possibly appeared as low as Re∼550-620, and were confidently identified at Re∼700. Once again the point at which the spectrum reached the noise level appeared to decrease with lower Re. Generally, the Kolmogorov frequency appeared to be lower than for model A, and by approximating the Kolmogorov time scale as 1/800Hz = 0.0013s, $\varepsilon = 0.64\ J/(s \cdot kg)$ and $\eta = 63\ \mu m$.

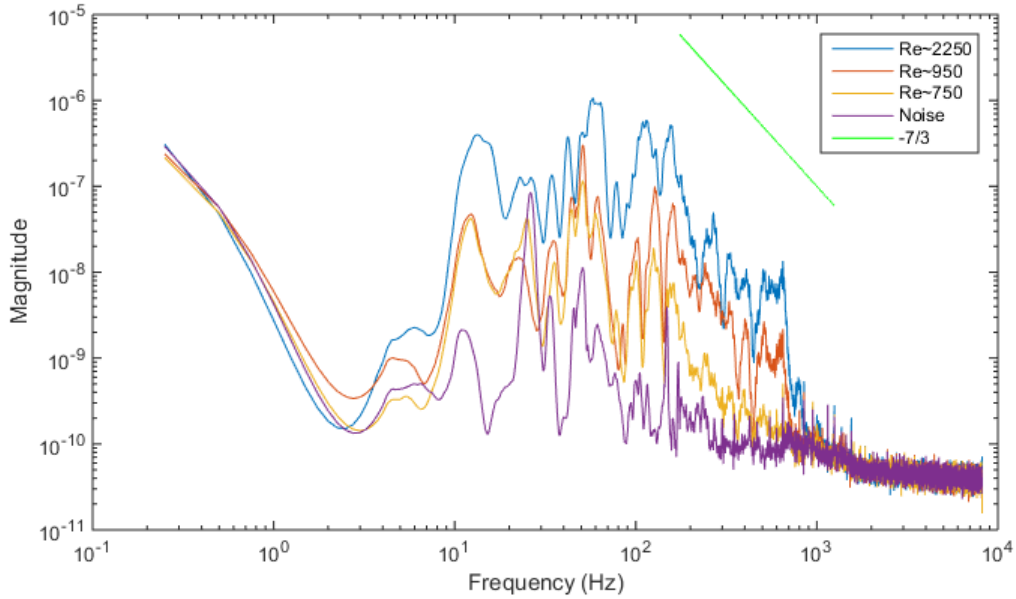

Figure 4.13: PSDs of flow through model B1 at various Re

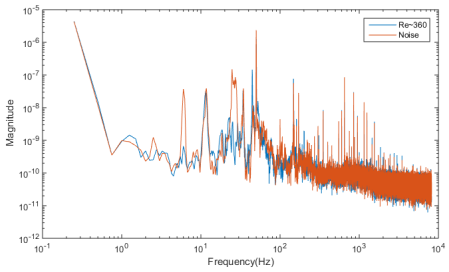

(a) Re∼360

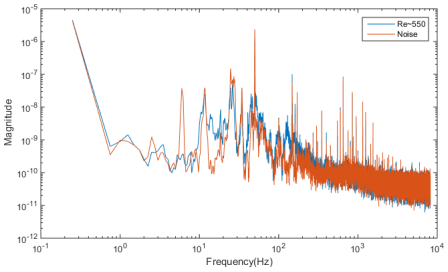

(b) Re∼550

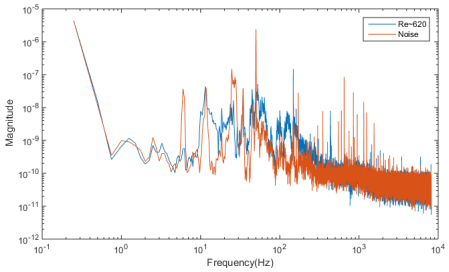

(c) Re∼620

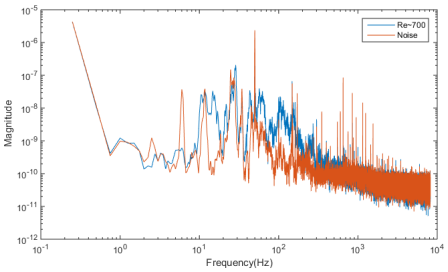

(d) Re∼700

Figure 4.14: Model B: Comparison of low Re PSDs with noise

Comparisons

Flow separation and inceptive flow fluctuations were identified at a lower Reynolds number in model A (∼ 400) compared to model B (∼ 700). Although both occurred at low Re relative to other well known flows, e.g. a cylindrical pipe/healthy blood vessel, the difference between the two was substantial from a biological point of view, as Re∼ 700 is unlikely to be experienced in the body for a cerebral aneurysm, whereas Re∼ 400 is highly plausible. This supports the notion that flow patterns are aneurysm specific, and some geometries may experience more unstable flow

than others, with potentially significant biological effects. The difference in critical Reynolds number coincides well with those obtained from direct numerical simulations performed by Jain et al. in which the critical Re was found to be 350 for model A, with fluctuations appearing as low as Re 250 [31]. No indication of fluctuations were found for model B by Valen et al., corresponding to case #5 in their naming convention [83]. Note that model A corresponds to case #12, and fluctuations were observed even though the simulation was not as highly resolved as Jain et al.'s. The differentiation between the two models and the similarity to DNS/CFD results adds to the validity of the measurements performed, indicating that the fluctuations were a result of the geometries, and not purely caused by disturbances to the flow elsewhere in the setup. However, the seemingly lower critical Reynolds number observed for flow through a cylinder warrants further investigation of potential disturbances in the experimental setup.

The Kolmogorov time and length scales were found to be larger for model B, as a result of a lower turbulent energy dissipation rate. The relative size, i.e. the characteristic length scale, of the aneurysm in model B was smaller than in model A, which per equation 2.15, $\varepsilon \propto u^3/L$, would result in a larger dissipation rate. This indicates that the local, aneurysmal flow velocity, i.e. the characteristic velocity, was lower in model B compared to model A, to allow for theoretical agreement. The dissipation rate is more sensitive to a decrease in flow velocity, explaining the lower dissipation rate even though the length scale decreased. This conclusion does, however, assume that the measured Kolmogorov timescales were physically accurate, and that they were not influenced by propagation issues or other errors. The velocities within the aneurysm sacs were therefore compared using PTV results in section 4.3.5.

Differences between a biological flow and the idealised flow used for the measurements performed also likely affected the transition to turbulence. As previously mentioned, a pulsatile flow would likely facilitate an even earlier transition, and should be examined in the future, as should using blood as the fluid. The effect of material and size is further examined in the following two subsections.

4.2.2 Material Comparison

Differences between the model material and a blood vessel may potentially have impacted the creation of fluctuations within the models, with the two most important parameters being elasticity and surface roughness. The resulting PSDs of flow through models made of two different materials were therefore compared. Material names were not available at the time of writing and as such no standardised values of the material properties have been used for quantification of the materials. However, model A1 (yellow material) was qualitatively rougher, yet softer/more elastic than model A3 (white material).

Figure 4.15 shows average PSDs of three runs at Re$\sim$1400 for model A1 and A3, using connector type 3. The PSDs were clearly similar, however model A1 displayed slightly lower magnitudes at low frequencies, and higher amplitudes at high frequencies. This may be indicative of a slight difference in flow patterns and/or a slight difference in sound propagation/attenuation. The increased roughness of model A1 may have accelerated turbulence generation, causing a comparatively enlarged presence of high frequency oscillations. However, any differences may also have been a result of changes in the way the materials propagated and attenuated the pres-

sure differences. Two significant variables were therefore affected by changing the model materials, and any changes to the flow due to altered roughness could not be accurately determined without knowledge of how the materials compared in terms of propagating the produced sounds. Models made of the same materials but with different surface roughness would be better suited for a direct comparison, or alternatively noise propagation could be investigated by producing a known frequency inside the aneurysm models of different materials. It must therefore be assumed that surface roughness had the same effect in the model aneurysms as it does for other flows, and the results obtained from the smoother material are more accurate if a comparison is to be made with a smooth blood vessel. Regardless, differences between the two materials investigated were small.

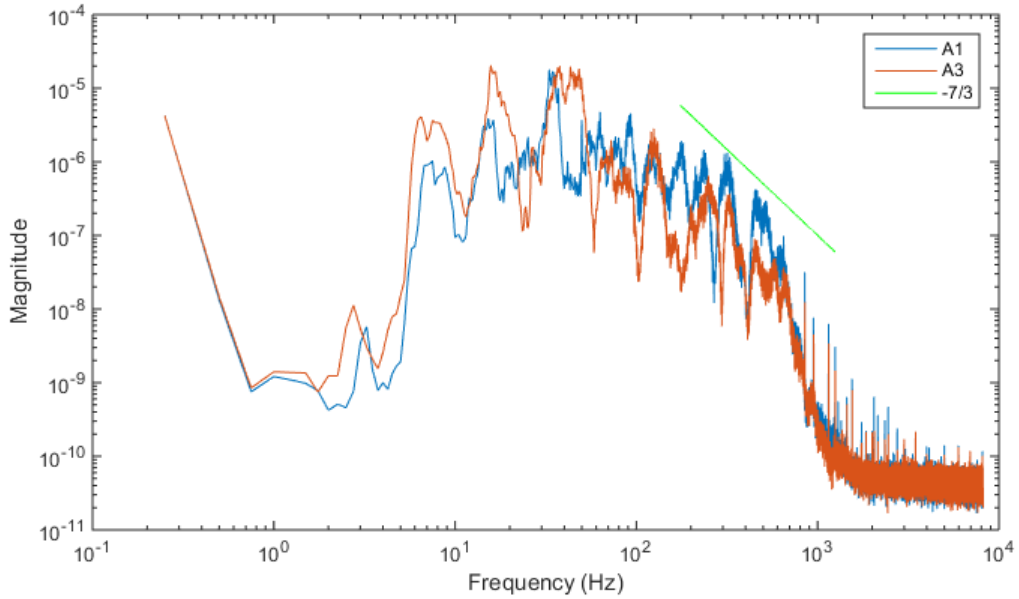

Figure 4.15: PSDs of flow through model A1 and A3 at Re∼1400

4.2.3 Size Comparison

Due to the lack of established similarity laws for fluid-structure interactions in complex geometries the effect of scaling was considered for the purpose of a more accurate comparison with physiological flows. The aneurysm replicas used for measurement thus far were scaled by a factor of 3, and the flow through a smaller model, scaled by a factor of 2, was therefore examined. Figure 4.16 shows a comparison of the averaged PSDs obtained from three trials of acoustic measurement of flow through model A3 and A5 at Re∼1370. For model A5 smaller magnitudes were seen at both low frequencies and high frequencies, whereas magnitudes were similar in the intermediate frequency range. The PSD also approached the zero level at a lower frequency relative to model A3. This observation was counter-intuitive to the basic turbulence theory presented in chapter 3. As the Reynolds number was kept constant, the decrease in characteristic length in the smaller model was accompanied by a proportionally higher characteristic velocity. Given $\varepsilon \propto u^3/L$, this should have resulted in a net increase in the turbulence dissipation rate and following equation 2.14 the Kolmogorov timescale should have decreased, i.e. the frequency at which

the energy of the signal reached the zero level should have increased. Whether the observed effect was physically correct, with a possible explanation being a larger relative decrease in velocity within the aneurysm sac for the smaller model, or caused by errors in the measurements, remains unclear. The two sizes considered were therefore not an adequate basis for extrapolation down to physiological sizes.

A significant drop in magnitude was seen around ∼2-700Hz for the smaller model, which may indicate that issues with sound propagation and attenuation played a factor, and could explain the unexpected increase in the Kolmogorov timescale. The smaller size resulted in weaker pressure fluctuations, as evidenced by the mean amplitude of the signals obtained: 14.1mV for model A3, and 7.5mV for model A5. Consequently, weaker, high frequency fluctuations were more easily lost in the background noise, resulting in the appearance of a higher Kolmogorov time scale. Measurement of flow through a 1:1 scale aneurysm model would therefore likely require proportionally greater sensitivity to pressure fluctuations, and a significantly lower background noise level.

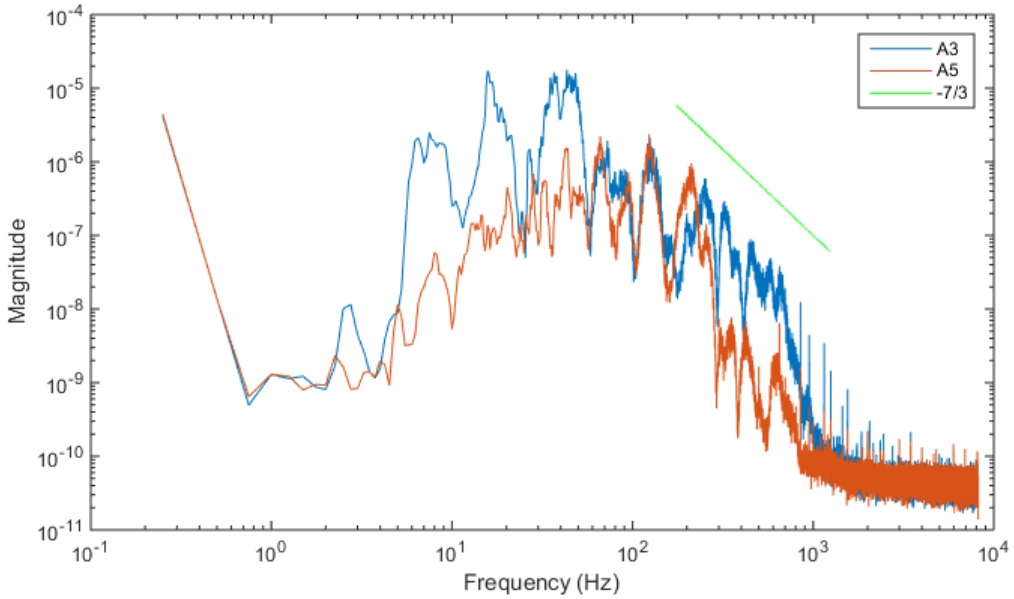

Figure 4.16: PSDs of flow through model A5 and A3 at Re∼1370

4.3 X-ray PTV Results

4.3.1 Tracking Particles: A Walkthrough of the 3D XPTV Method

A simple PTV algorithm was implemented in Matlab to allow for processing of the x-ray images and subsequent determination of the particle 3D positions, velocities and accelerations. The process is outlined in this section for a sample x-ray image taken of model A with two particles present. Matlab code can be found in appendix D.

The original x-ray image is shown in figure 4.17a. To allow for PTV analysis the image was inverted so as to have light particles on a dark background, as per convention for most PTV software and image processing tools implemented in Matlab. This can be seen in figure 4.17b, which also shows that due to the nature of the x-ray images, the resulting images displayed light particles on a slightly less light background. The x-rays were attenuated by the water and model, although not to the extent of the x-rays that passed through the particle. In order to aid in further processing a mean image was created from the whole image series, as seen in 4.17c. When subtracted from the inverted image the result was an image with light particles on a darker background, as seen in 4.17d. Note that the images have been displayed using the "imagesc" function in matlab, which scales the range of colours displayed, and makes discerning differences in contrast easier visually, although numerically the non-scaled colour differences are proportionally different and easily distinguished.

A close up of the particles can be seen in figure 4.18a. Determination of particle position could possibly have been accomplished using these grey scale images, but did not initially work with any the position determination functions attempted, possibly due to the poor contrast between particle and background. Improved image pre-processing may potentially rectify this in the future. The next step therefore involved binarisation of the image using a chosen threshold value. The resulting black and white image can be seen in figure 4.18b. Small blobs of white pixels remained throughout the image and were removed using Matlab's "bwareaopen" function. At this point Matlab's "regionprops" function could be used to find the centre of the particles, theoretically allowing for determination of the particles position to subpixel accuracy. However, as a result of the variations in particle size, shape and density, the x-ray imaging, and the binarisation procedure, many particles were displayed as irregular white shapes, and the accuracy of the regionprops function was compromised, as outlying white pixels tended to skew the determination of the centroid. A slightly more sophisticated approach was therefore attempted using Matlab scripts developed by Blair and Dufresne [8]. This involved a bandpass filtering of the binarised image using bpass.m, and a comparison of the binarised and bandpass filtered particles is shown in figure 4.18c and d. The key effect was a smoothening of the edges and an intensity decrease of outlying pixels. The particle centre to pixel accuracy was then found using pkfnd.m and subpixel accuracy achieved using cntrd.m.

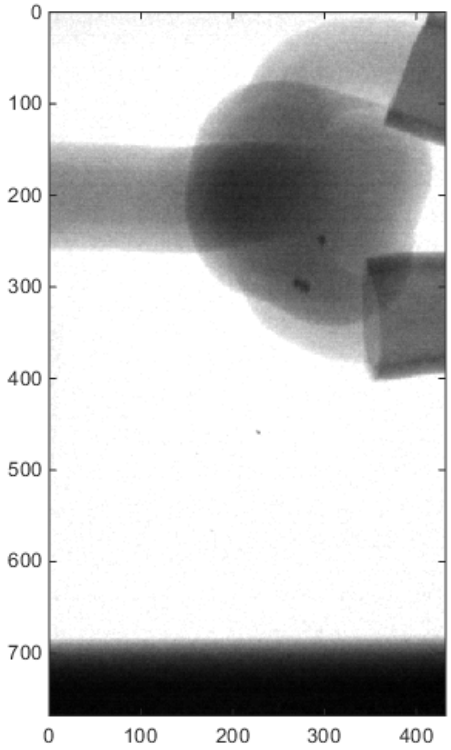

(a) Original x-ray image

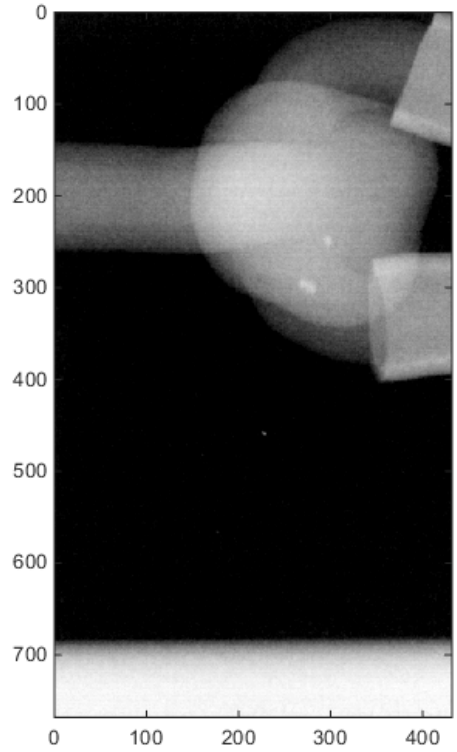

(b) Inverted x-ray image

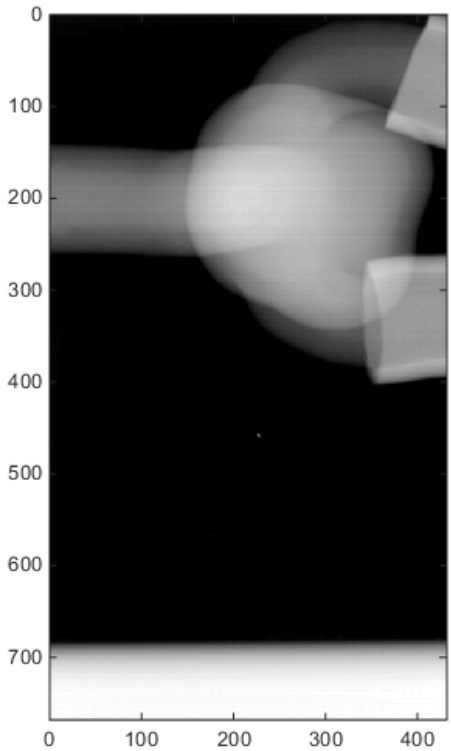

(c) Mean x-ray image

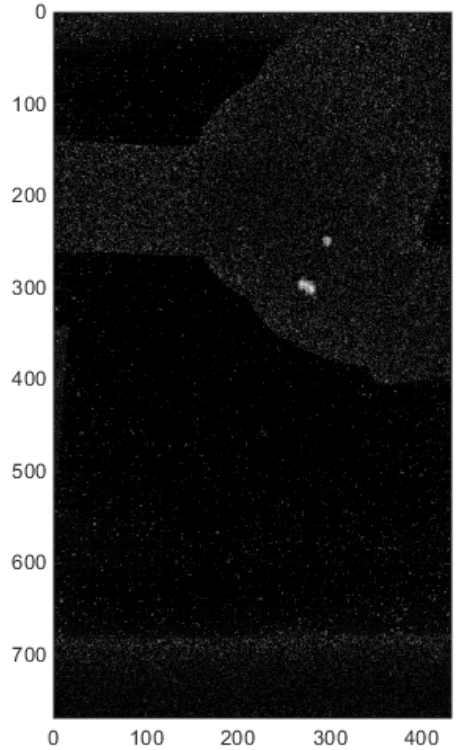

(d) Mean image subtracted

Figure 4.17: Image Processing

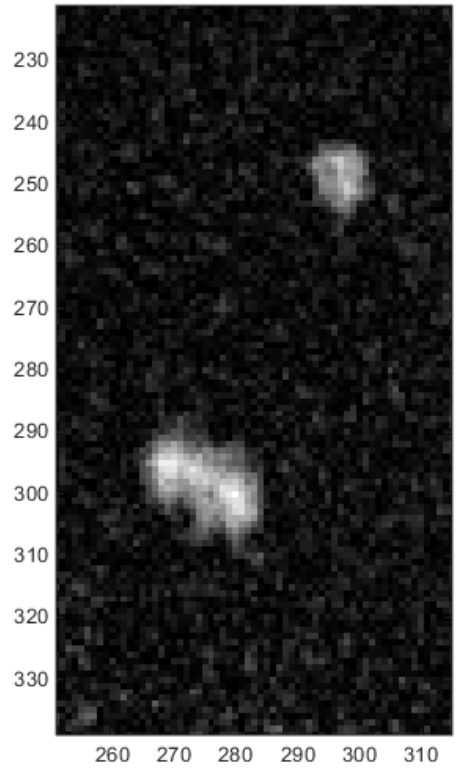

(a) Original image particles

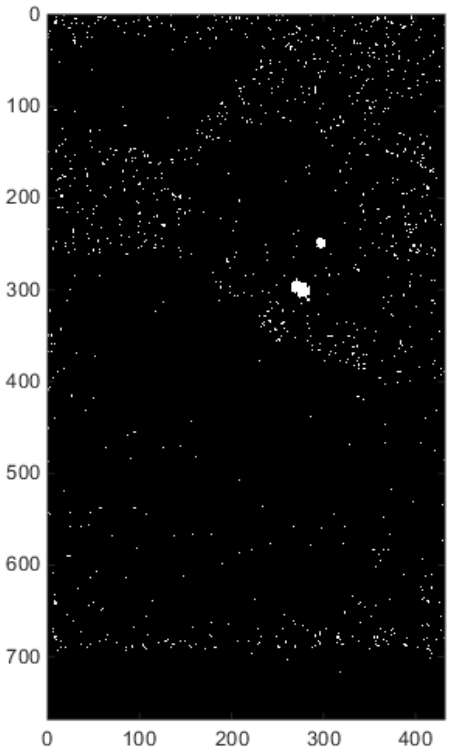

(b) Binarised image

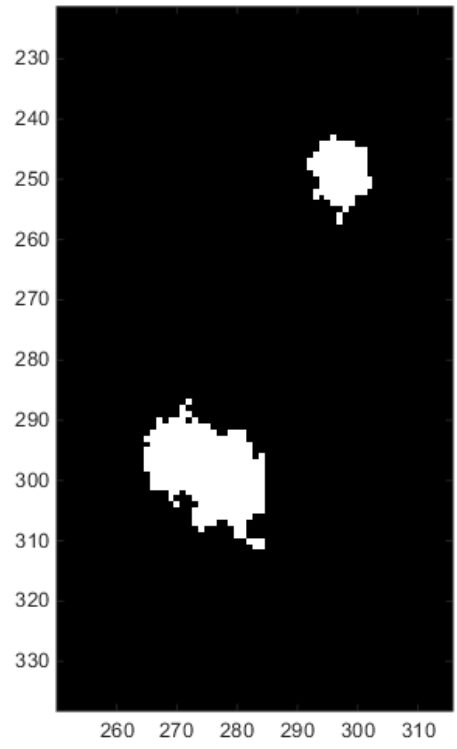

(c) Binarised particles

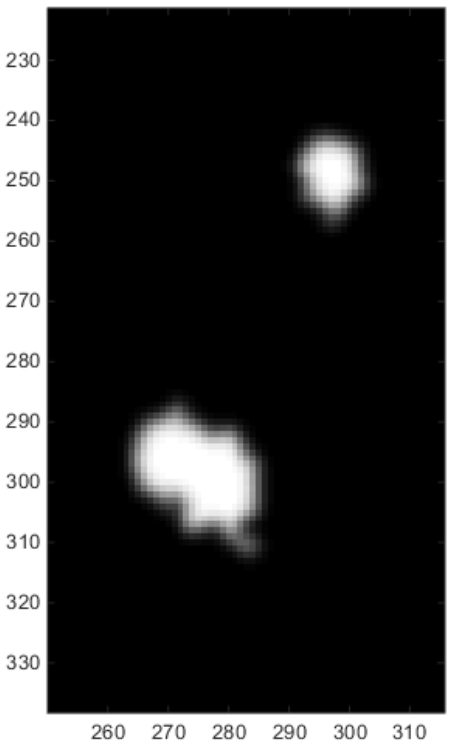

(d) Bandpass filtered particles

Figure 4.18: Binarisation and particle isolation

3D positions were then found using the method described in section 2.4.2. Figure 4.19 visualises the resulting line segments from the x-rays sources to the observed points on the detector screens for the two particles in the image presented in this section and the image from the second source/detector pair. Repeating this procedure for each time step thus allowed for determination of 3D particle positions over time, and individual particles could be tracked using a tracking algorithm. This was accomplished by use of the Hungarian method, implemented in Matlab by Tinevez [79].

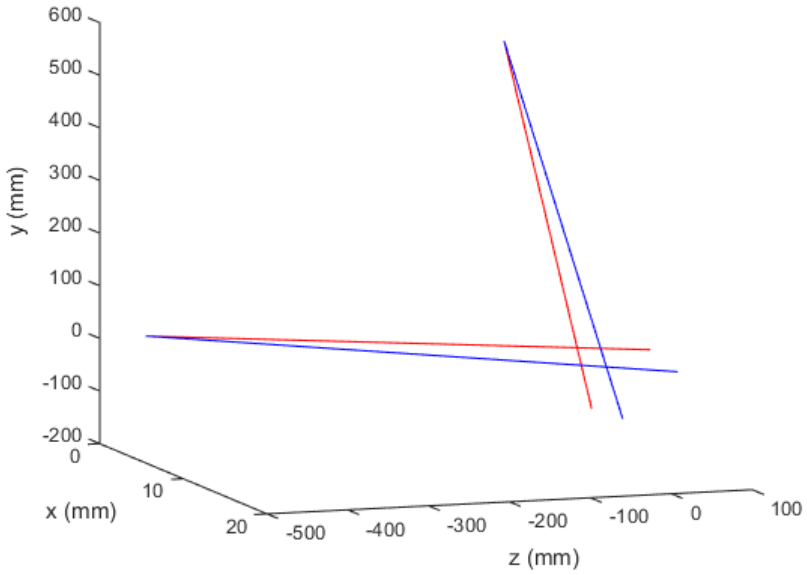

Figure 4.19: Determination of 3D positions visualised

4.3.2 Flow Visualisation and Characterisation: Model A

Figures 4.20 to 4.23 show a selection of pathlines resulting from PTV analysis through model A2 at various Reynolds numbers. Visually, the pathlines all followed similar patterns, with seemingly chaotic motion of the particles within the aneurysm sac, even at Re∼280. In general, velocities were substantially decreased as the flow entered the aneurysm sac relative to the parent artery velocities. Velocities decreased in line with the Reynolds numbers, indicating that the PTV analysis was successful and able to differentiate flows and flow patterns. At lower Re, discrepancies in the velocities can be seen, and errors in the PTV analysis are therefore further discussed in section 4.3.4.

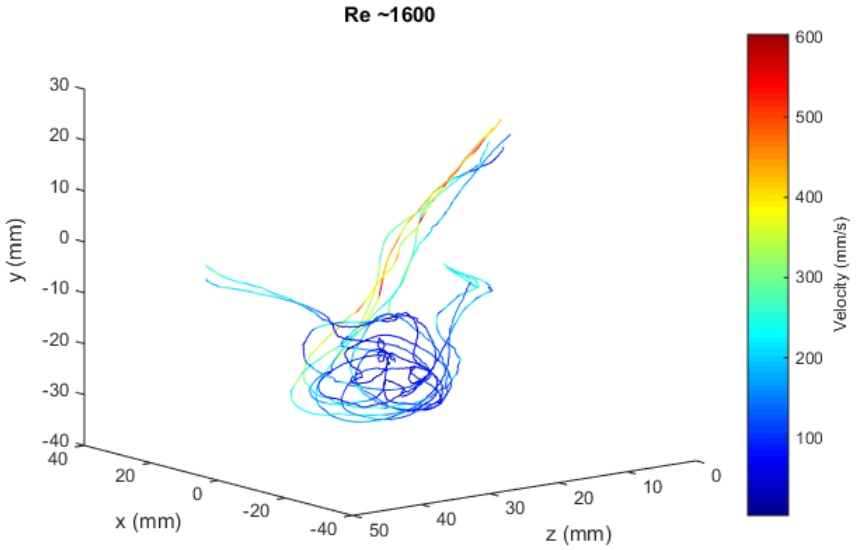

Figure 4.20: Pathlines of particles flowing through model A at Re∼1600

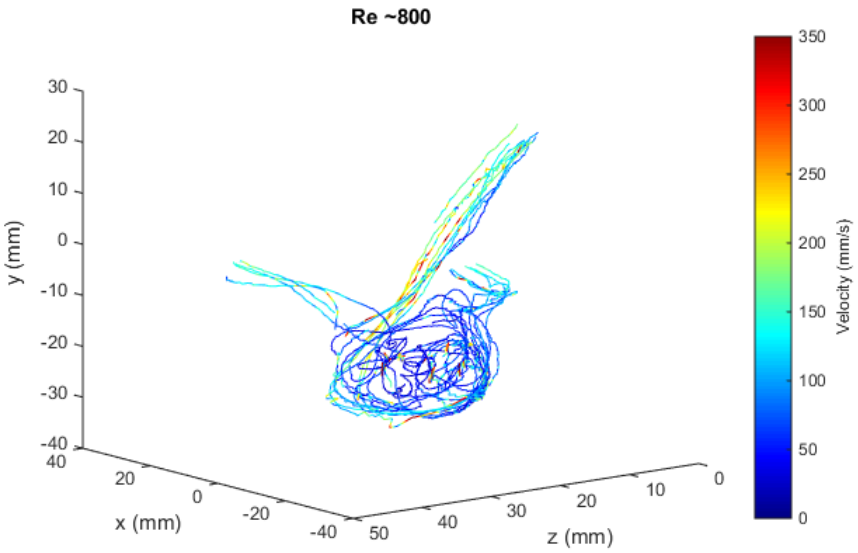

Figure 4.21: Pathlines of particles flowing through model A at Re∼800

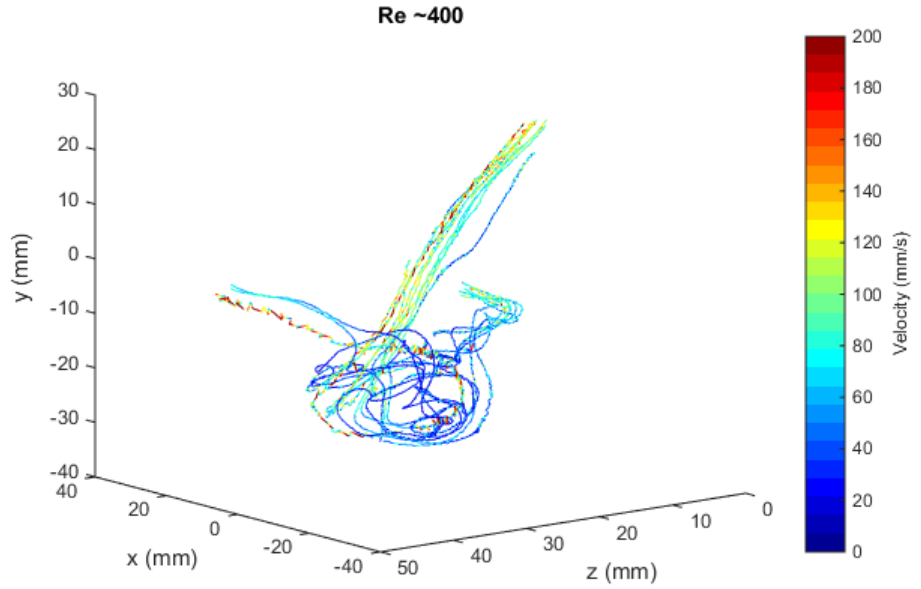

Figure 4.22: Pathlines of particles flowing through model A at Re∼400

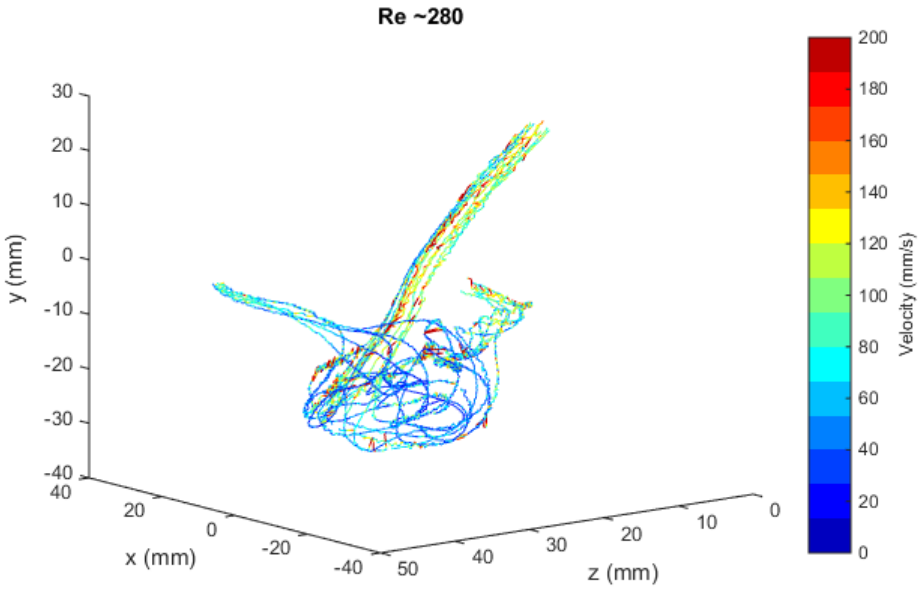

Figure 4.23: Pathlines of particles flowing through model A at Re∼280

At Re∼1600 the average velocity in the parent artery based on the measured mass flow was ∼0.225 m/s, or ∼225 mm/s. Assuming completely laminar flow in the parent artery, and an ideal cylindrical pipe, the maximum velocity is twice the average velocity; ∼450 mm/s [87]. This is roughly in line with the velocities measured using PTV through the parent artery, depending on the particle path. In some cases higher than expected velocities were measured, which may have been caused by errors in the PTV analysis, or may be physically correct, as the parent artery was in reality not an ideal pipe, and saw variations in diameter, and had some curvature. Within the sac, velocities were generally below the average parent artery velocity, and became almost stagnant in some cases, even at high parent artery Re.

Higher velocities were seen near the edge of the sac, and particles generally experienced small, random accelerations as they moved within, indicative of fluctuations and chaotic flow patterns. Circular motion indicative of vortices with diameters much smaller than the sac itself were also observed, and appeared to be somewhat localised. Figure 4.24 shows a comparison of pathlines at Re∼800 and ∼280 in the x-y plane. At higher Re the vortices were generally shifted towards the back of the sac, whereas at lower Re the vortices occurred earlier and at the front of the sac. Overall, the flow may therefore be viewed as jet like, as the flow from the parent artery entered a much larger space, although it was constricted by the aneurysm wall on one side. Jet like flows have a much smaller critical Reynolds number than flows in pipes, at roughly 500 [91]. This may therefore be a better indication of whether a flow can be assumed laminar in a numerical simulation, compared to simply the parent artery Reynolds number.

A more rigorous quantitative identification of flow fluctuations based on Lagrangian particle velocities is less straight forward than for Eulerian measurements methods such as PIV, where the velocity at a point is calculated for each time step. An equivalent analysis would require extrapolation of velocities onto a grid in order to quantify the velocity field, and is severely limited in cases of small numbers of particles as was the case for the experiments performed. A purely Lagrangian analysis therefore often relies on examining "random walks", i.e. pathlines of individual particles, as was the basis of the observations presented thus far. Further analysis may be performed, particularly based on the statistical properties of the flow. This may include Lagrangian autocorrelation analysis [52] and Lagrangian spectral analysis [42]. This analysis has not been performed as part of this thesis, and a more in-depth quantitative (Lagrangian) analysis of the particles motion and fluctuations would therefore be suitable for further investigation in the future. Elimination of the sources of error outlined in this thesis would be beneficial for this purpose, and a quantitative analysis would be further facilitated by the ability to have more particles present in the flow simultaneously. Additionally, improved control of the flow velocity would be advantageous so that particles moving through the model over time could be more accurately compared without being affected by a change in Re.

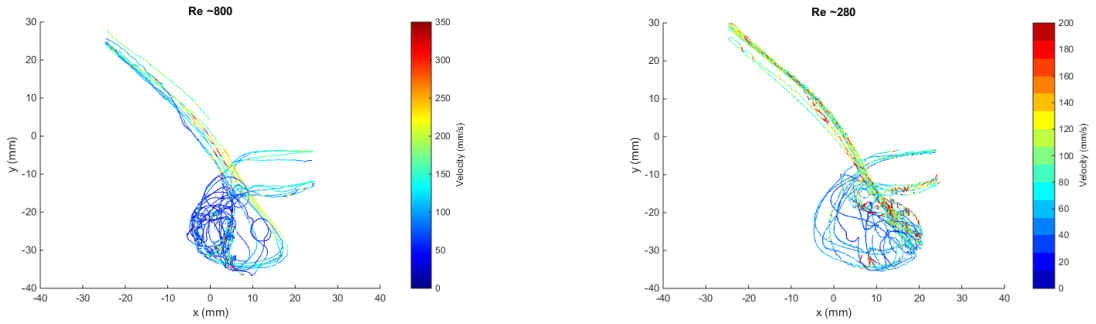

(a) Re∼800 (b) Re∼280

Figure 4.24: Localised vortices within the aneurysm sac

4.3.3 Flow Visualisation and Characterisation: Model B

Figures 4.25 to 4.27 show a selection of pathlines resulting from PTV analysis through model B1 at various Reynolds numbers. The smaller size of the aneurysm

sac resulted in generally cleaner pathlines and velocities compared to model A, due to less overlap of the particles, although small deviations in calculated velocities become more apparent at Re∼400 as the errors in position were proportionally larger relative to the displacement, as was also the case for model A. Using every other image (or less) for analysis could counter this, at the expense of some resolution in time, but has not been performed.

Throughout the non-aneurysmal blood vessels, velocities were observed to vary consistently depending on position and were related to the diameter of the vessel. This, combined with the general trend of a decrease in velocities as Re decreased, added validity to the PTV analysis. However, as the Reynolds number decreased, so did the ability of the particles to follow the flow into the aneurysm sac. This is further discussed in section 4.3.4.

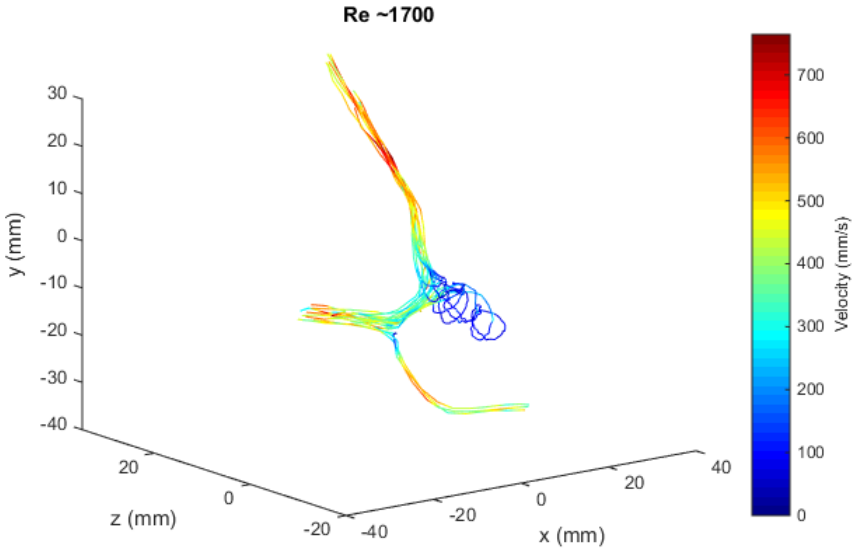

Figure 4.25: Pathlines of particles flowing through model B at Re∼1700

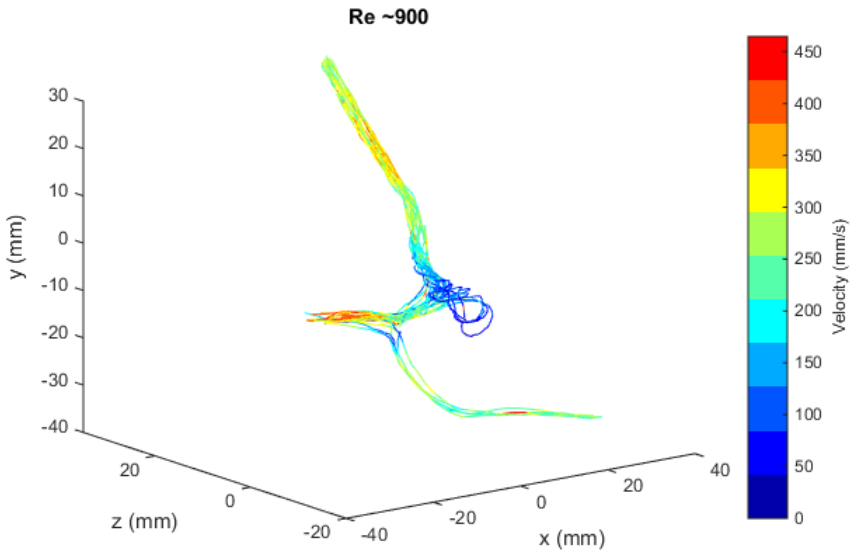

Figure 4.26: Pathlines of particles flowing through model B at Re∼900

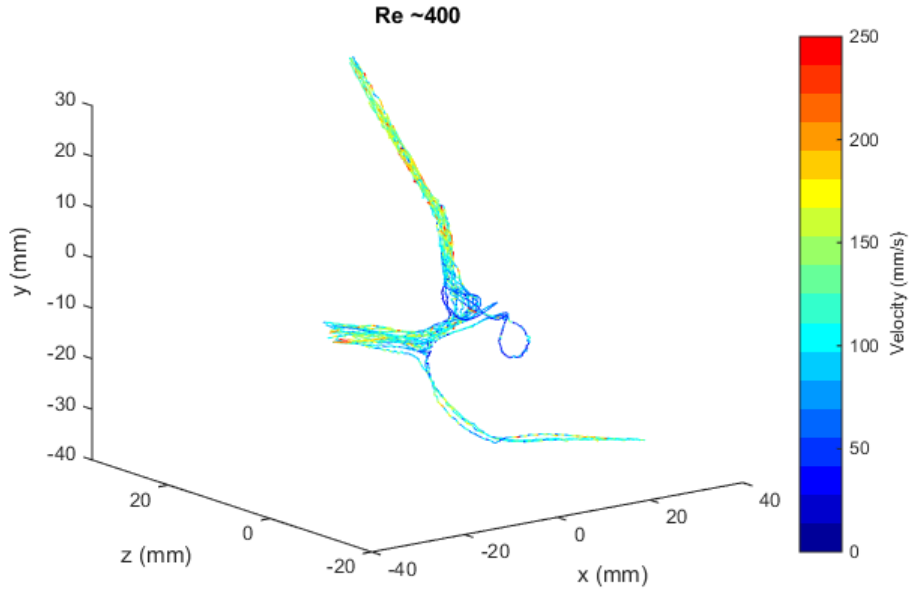

Figure 4.27: Pathlines of particles flowing through model B at Re∼400

Velocities inside the aneurysm sac decreased relative to the parent artery velocities, but appeared less chaotic than for model A. This was particularly apparent at Re∼900, where several particles appeared to have followed similar paths inside the aneurysm sac. In general particles tended to exhibit circular motions upon entering the sac, and often followed the sac edge. The particles frequently left via a route through the centre of the sac, typically following straighter lines, or displaying small circular motions. Many particles passed the aneurysm sac without entering, or only entered superficially, especially at lower Re. As mentioned, whether this was due to the particles ability to follow the flow, or was physically correct, is unclear. Tracking more particles through the aneurysm may have resulted in more particles entering deeply into the sac at low Re.

4.3.4 Error Analysis

The error associated with the three dimensional particle position was quantified by examination of the distance between the two source-detector line segments. Using image pairs in which only one particle was present[2] the mean length of the shortest line connecting the two line segments was found to be 1.6mm, a substantial error relative to the particle size and the displacement between images, implying an uncertainty of ±0.8mm in particle position. However, the standard deviation of the distances was much smaller, at 0.2mm (N=564), suggesting that the mean distance observed between the source-detector line segments was the result of a systematic error in the setup. The standard deviation implied 95% of the particles were within a random error of ±0.2mm from the calculated positions. A systematic error may have been caused by small misalignments in the source detector pairs, or by inaccuracies in the physical measurements of the setup and the assumptions made, i.e. the

[2]This ensured particles were not incorrectly matched in the 3D reconstruction, which would affect the average distance between the line segments, and prevented any outliers that would skew the mean. (The median could also be considered if this was an issue).

x-ray centrelines may not have hit the detectors perfectly centred, and the relative positions of the sources/detectors used for 3D reconstruction may have been slightly off. Further investigation into the source of this systematic error may therefore be worthwhile, and may be accomplished by imaging known, precise geometries, and/or by controlled translation of a geometry or small particle in order to find the x-ray centrelines. If more accurate positions of the sources and detectors are found, these can be used for 3D reconstruction in the future. In the case of small misalignments, defining the origin of the global coordinate system as one of the sources is a better alternative, since the centrelines emitted from the two x-ray sources may not cross and allow for the definition of a global origin as done currently. Errors may also have been caused by more complex mechanisms related to x-ray behaviour, production and detection.

The random deviations in determination of particle position were likely caused by the non-ideal shape and movement of the particles, and inaccuracy in the PTV analysis when particle positions were determined, both in 2D and in 3D. The 3D reconstruction method relied on correct matching of particles between the image pairs, and compared all the source-detector line segments before choosing the matched particles which minimised the distance between one line segment to another. However, the systematic error meant finding the minimum distance often resulted in inaccurate particle pairing. In order to counter this, particles were paired by matching the distance between the line segments to the systematic error of 1.6mm. This increased the accuracy and success of the PTV algorithm substantially, however in some cases particles were still mismatched as pairing with another nearby particle came closer to 1.6mm due to the random error. This resulted in discontinuities in the pathlines, and potentially wildly inaccurate velocities, and the effect was worsened the more particles were present. In some cases, particles were also lost in the two dimensional stage due to an inadequate thresholding value. The accuracy of the results could therefore likely be improved by developing the post-processing code further, or by using commercial/open-source software. In particular a more comprehensive particle detection algorithm could be used on the 2D level, including the use of several threshold values for binarisation. Using a single, set threshold value as was done for the current analysis was not without fault, especially when the model orientation resulted in areas of considerable overlap, and the relative intensity of the particle was weakened in these spots. An improved particle pairing algorithm between the two images could also be used when performing the 3D reconstruction, as the current method was too dependent on minimal random errors, which proved unobtainable in an experimental setting. Instead of considering individual particles, minimisation based on all the particles present would be preferential, similar to transient particle tracking algorithms.

Non-ideal motion of the particles was frequently spotted through visual inspection of the x-ray images, as particles were observed to spin, bounce against the walls, and get stuck inside the aneurysm models. The latter was particularly an issue at $Re<800$. These issues were likely caused by the inconsistent shape and varying densities of the particles, as some were large and cylindrical and some would sink and others float. Overall, this also appeared to affect the determination of 3D positions in the post-processing and the non-spherical shape of the particles meant determination of the centroid was not ideal. The particles covered large amounts of pixels, which meant small variations in the imaging or post-processing resulted in a

potential loss or gain of several pixels, which quickly resulted in decreased accuracy. Several particles also appeared to consist of two particles which had not been split in the production phase, which resulted in two nearby peaks when the position of the particle was determined. This therefore potentially increased the random error, especially if the particles spun and the centroids of the particle moved with it in the projection plane. Consequently, many of the pathlines displayed overly zig-zaggy behaviour, which made identification of real, small-scale fluctuations difficult.

The variance in size and density also affected the relaxation time of the different particles, and some were therefore better suited than others in terms of following the flow. For illustrative purposes the particles from the image in figure 4.17a can be considered. One particle is substantially larger than the other, which was indicative of the typical variation in particle size[3]. Using the pixel size, the two particles can be roughly approximated to have dimensions 0.6×0.6mm and 0.6×1.9mm in two dimensions[4]. One particle is therefore smaller and nearer to an ideal spherical shape, whereas the other is larger and elongated. Considering only the smaller, more ideal particle, and using a Kolmogorov timescale of 1/1000Hz this translated to a Stokes number of ∼20. This assumed a density equal to water, and greater deviations are therefore expected in reality due to density mismatch and non-spherical shape. The particles used therefore did not follow the flow down to the microscales.

The accuracy of the results was also inherently limited by the spatial and temporal resolution of the hardware used. A frame rate of 155 fps meant fluctuations with frequencies of 77.5 Hz and below could be theoretically identified, placing the resolution firmly in the integral scales of the flow. The spatial resolution was limited by the pixel size, as the particles had to be large enough to cover several pixels in order to achieve sub-pixel accuracy. Using particles which followed the flow down to the microscales would therefore be unnecessary, and a comparison with the theoretical resolution of the system is more relevant. Using a timescale of 1/75Hz resulted in a Stokes number of ∼1.5 for the best-case particle previously considered. This is indicative of a relatively decent ability to follow the flow, but is far from ideal, as a Stokes number <0.1 is required for tracing accuracy errors below 1% [81]. The majority of the particles were also less ideal in shape. This shows that the x-ray system is theoretically capable of greater accuracy than was achieved in the present measurements. Consequently future improvements appear to be highly reliant on using better suited particles, i.e. smaller, and more spherical, in order to achieve Stokes numbers $\ll 1$, whilst ensuring they can still be resolved by the x-ray imaging. Using a more robust PTV code, and better particles, a comprehensive validation of the setup can be performed in which results are compared to a known, exact solution, and the accuracy can be properly quantified.

4.3.5 Comparisons

The PTV results were generally in line with the acoustic and DNS results, and expected flow behaviour was observed. Model A appeared more chaotic, even at low Re, whilst the pathlines in model B appeared more orderly. Even at Re∼280

[3]Note that the difference in size was not caused by a difference in orientation of the two particles, although a similar effect could be observed if this were the case.

[4]Due to the small size of the particles, differences in the size due to conical projection effects are negligible for this estimation

the pathlines were highly chaotic in model A, a Reynolds number in which flow fluctuations were not observed acoustically. This may have been caused by the intensity of the fluctuations being too low for the microphone to pick up relative tot he background noise, or the chaotic behaviour may have been partly caused by the particles poor ability to follow the flow at low Re. It should also be noted that DNS found fluctuations as low as Re 250, and the chaotic flow pattern observed may therefore by physical. The localisation of the vortices at low Re agreed with the visualisation of turbulent kinetic energy presented by Valen et al. [83].

Assuming pressure fluctuations were mostly created within the aneurysm sac, the aneurysmal velocities for the two models were compared in order to verify the conclusion drawn from the acoustic measurements, i.e. that velocities within the sac had to be comparatively lower in model B, in order to account for the lower dissipation rate and larger Kolmogorv scales. A comparison of the parent artery flow for model A at Re$\sim$1600 shows a comparatively lower velocity than in model B at Re$\sim$1700, as expected not only because of the higher Re, but also due to the smaller diameter of the vessel in model B which further increased velocities. None the less, the velocities inside the aneurysm sac for model B were generally lower, or of similar magnitude to those in model A. The PTV results therefore support the findings from the acoustic measurements. Physically, this effect may be explained based on the geometry of the two aneurysm models. In model A, a bifurcation aneurysm, the flow from the parent artery was directed directly into the aneurysm sac where it experienced a significant deceleration. Not only did this deceleration induce flow separation, but the average velocities within the aneurysm remained large due to high velocities observed initially prior to deceleration. This was in contrast to model B, a sidewall aneurysm, in which only a fraction of the flow entered the aneurysm sac. Furthermore, flow velocities had already been significantly decreased due to the bifurcation of the parent artery prior to the aneurysm location. This also highlights the imprecision of using a parent artery Reynolds number as a classification of the flow, as the Reynolds number in the artery directly prior to the aneurysm likely differed from the Reynolds number prior to the bifurcation.

The results were also limited by the simplifications made relative to a biological, haemodynamic system, as outlined in section 2.2. The flow was not pulsatile, the aneurysm models were enlarged and made of different materials, water was used as the fluid, and the flow prior to the aneurysm may have differed. None the less, the visualised flows are likely to represent real, biological flows to a certain extent, although future experiments should aim to bridge the gap. One particular effect that may be of interest from a biological point of view was the particles tendency to get stuck at low (physiological) Reynolds numbers. Erythrocytes, or red blood cells (RBCs), are effectively small particles suspended in in a fluid (plasma) and have a higher density (plasma: $1025kg/m^3$, RBCs:$1125kg/m^3$ [6]). Given the low flow velocities in the body this density difference may therefore be important, as velocities were observed to significantly decrease within the aneurysms. This could potentially lead to build up of RBCs should they not follow the flow adequately at low velocities, which could have an important biological impact. RBCs facilitate platelet activation and adhesion which may result in thrombus formation [63, 1]. Compared to the particles used, RBCs are roughly 100 times smaller, with an average diameter and thickness of roughly 8 and 2μm respectively, and therefore likely follow the flow much better, although to what extent has not been investigated as part of this

thesis. Stagnation points within an aneurysm may, however, also result in a similar effect. Throughout the literature some research has been focused on these effects (e.g. [45, 46]), although further (experimental) investigations into RBC deposition and particle interaction may be beneficial in order to conclusively determine the effect of assuming a Newtonian fluid in numerical simulations, and whether or not gravity affects the flow substantially. Conversely, thrombus formation may also be caused by high wall shear stresses eliciting biological effects [85]. Thrombus formation in general must therefore be accounted for in a complete numerical model aiming to quantify the risk factor of an aneurysm, and correlating flow patterns with RBC behaviour may be an important part of this. The process is highly dynamic, and the formation of a thrombus may also affect the flow patterns. Further research into this aspect of aneurysm pathophysiology may therefore be useful and would require experimental results.

4.3.6 CO_2 Bubbles as Seeding Particles

Figure 4.28 shows an x-ray image of carbon dioxide bubbles generated by using carbonated water as the operating fluid through model A. The x-ray imaging was able to distinguish relatively small bubbles, and illustrates the possibility of using gas bubbles as seeding particles. The PTV code used was unable to successfully determine bubble locations, however this could likely be accomplished with only minor modifications, both in the code and in the settings used for the x-ray imaging. None the less, the present carbon dioxide bubbles were unsuited for the purpose of analysing flow through aneurysms, as they followed the flow poorly due to their size and low density. Other gases could be considered for use as seeding particles, such as hydrogen bubbles, which have been used successfully for other applications in the past. Bubbles which follow the flow, yet remain resolvable in x-ray imaging may therefore be found, and would be an alternative to the heavy metal particles currently used. The imaging of these bubbles also highlights the systems capability to analyse multiphase flows, which encompasses a wide variety of applications.

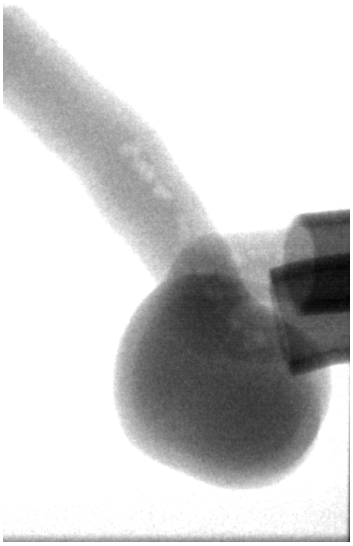

Figure 4.28: X-ray image of carbon dioxide bubbles

Chapter 5

Conclusions

The findings from this thesis are divided into conclusions related to the experimental methods, and conclusions made from their application to flow through intracranial aneurysm models. Overall, the results provided experimental indications of aneurysm specific fluctuating flows at physiological Reynolds numbers, and proved the two methods' efficacy and potential in measuring flows non-intrusively and accurately.

5.1 On the experimental methods

A gravity driven flow system was utilised which generated sufficiently high and steady flow for the intended purposes, however manual determination of the flow rate using a scale and a timer resulted in an estimated 10% uncertainty in Reynolds number. In general, both methods would benefit from increased control of the flow output and resulting flow rate determination. The simplest solution involves the use of a scale capable of automatic recording of the weight over time, or a flow meter, for the purpose of accurate calculation of the instantaneous flow rate. Future work could aim to develop a pump driven and potentially closed system, with an improved ability to control particle seeding for the PTV method. This may also facilitate investigation of pulsatile flows, and the use of blood as the operating fluid, both of which are key properties of biomedical flows.

5.1.1 The acoustic method

The acoustic method measured flow-associated fluctuations through the use of a contact microphone placed non-intrusively on the outer surface of a geometry. It relied on the principle that sounds, as percieved by the human ear, are fundamentally pressure fluctuations. Importantly, flow-induced pressure fluctuations are often divided into two categories: sound and pseudo-sound. The "normal" sound field radiates away from a source via compressible motion, and although this is what is typically associated with sound generation, only a small fraction of turbulent kinetic energy escapes this way. Pseudo-sound is an essentially local field independent of fluid compressibility and is what induces vibration on structures supporting turbulent boundary layers. The vibration of a structure may then further act as a source of sound generation in the surrounding medium. Pseudo-sound can be related to the flow field through a Poisson equation for pressure derived from the incompressible

Navier-Stokes equations, and is therefore related to velocity (and vorticity) fluctuations within the flow. The sound field is governed by the Lighthill equation, derived from the compressible N-S equations. The measured pressure is a non-local variable, in that it is a combined sum of fluctuations throughout the flow field. This complicates a physical interpretation of the results, and understanding the relationship between the measured pressure fluctuations and velocity fluctuations in the flow is therefore important, and may be worthy of further investigation, e.g. by measuring high frequency velocity and pressure fluctuations simultaneously.

The method excelled in temporal resolution, but was limited by the sensitivity of the microphone used and the amplitude of the fluctuations generated by the flow. Eliminating background noise is therefore exceedingly important if small fluctuations are to be recorded accurately, especially for flows in which the amplitudes of the fluctuations are small compared to the noise levels. The accuracy of the method was limited by uncertainty regarding the linearity of the microphone used, and therefore requires further validation. Alternatively, a microphone known to be linear over the required frequencies could be used in the future. Using a smaller microphone would also be beneficial in order to ensure a consistent area of contact on small geometries. Furthermore, a key issue for the acoustic method lies in the fact that the measured pressure fluctuations are not purely a product of the flow, but also depend on propagation and attenuation through the model geometry. Further investigation into this for any experimental geometry considered may therefore be necessary. An alternative approach is potentially to combine 3D printed, anatomically realistic aneurysm models with other manufacturing techniques, e.g. lost-wax casting, in order to obtain models made of materials with properties similar to blood vessels.

5.1.2 The 3D-XPTV method

The 3D-XPTV method combined stereographic x-ray radiography with particle tracking velocimetry, resulting in non-intrusive determination of Lagrangian velocities and accelerations of flows within opaque geometries. The method involved four key steps: x-ray imaging resulting in two 2D projections, determination of 2D particle positions, 3D reconstruction, and transient tracking of particles. The produced x-ray images were of high quality, and clearly identified the particles throughout the flow. The spatial resolution (pixel size 74.8 μm) was more than adequate for the particles used, even at 2×2 pixel binning. The accuracy of the results therefore largely depended on two parameters: the robustness of the PTV code used for determination of particle position and tracking, and the particles' ability to follow the flow. The PTV code used was a simple implementation of basic PTV principles, and improvements could therefore likely be made by using enhanced PTV algorithms and code, both for determination of 2D positions, and for 3D reconstruction. 3D positions were calculated based on the nearest point of intersection between two line segments formed between the sources and the detected positions of the particle in the projection planes. The minimum distance between the line segments served as a measure of the error in particle position, resulting in a mean distance of 1.6mm with standard deviation 0.2mm (N=564). This indicated a systematic error caused by small imperfections in the setup, or errors in the measurements of the geometry used for 3D reconstruction. The standard deviation implied 95% of the particles were within a random error of ±0.2mm from the calculated posi-

tions. Although small, this was significant relative to the particle displacement at low Reynold's numbers in the flows considered, given the temporal resolution of the system (155fps). The XPTV method therefore had significantly lower temporal resolution that the acoustic method, but was able to sufficiently resolve the integral scales of the flow, allowing for quantification of important flow patterns. The results were in reality much more limited by the particles' poor ability to follow the flow, and even the most ideal particles had Stokes numbers of $\sim$1.5 when compared to a time scale of 75Hz, much larger than required for negligible errors in flow tracing. Further work should therefore attempt to find better suited particles, which combined with improved PTV code should allow for high accuracy measurement of flows in which optical or intrusive access is unobtainable.

5.2 On flow patterns in cerebral aneurysms

Both methods were applied to steady flow through 3D printed, physiological cerebral aneurysm models for the purpose of investigating inceptive transitional behaviour and general description of flow patterns.

A spectral analysis on the pressure fluctuations obtained through the acoustic method was performed in order to quantify the flow. Welch's method was used to estimate the PSDs, and although it was shown to converge for 2^{18} data points, further investigations could be performed in order to determine the effect of changing the overlap percentage or the window function, or by using other methods. The emergence of transitional flow behaviour could be observed through an increase in magnitude in the PSDs as the parent artery Reynolds number was increased. Fluctuations clearly appeared at Re$\sim$400$\pm$10% for model A, whereas model B saw a later transition at Re$\sim$700$\pm$10%, supporting the notion that flow fluctuations may occur at physiological parent artery Reynolds numbers for cerebral aneurysms ($<$500), but are aneurysm specific. Indications of fluctuations were also found at slightly lower Reynolds numbers in both models. Mechanotransductional effects of fluctuating flows therefore likely need to be investigated comprehensively in order to understand how the haemodynamics within affect the pathophysiology of aneurysms, in addition to the purely mechanical effects on the vessel walls.

By assuming a direct relationship between the highest pressure fluctuation frequency and the highest velocity fluctuation frequency, the Kolmogorov time and length scales, τ and η, and turbulent kinetic energy dissipation rate, ε were estimated. For model A: $\tau \approx 1 \times 10^{-3} s$, $\eta \approx 31\ \mu m$ and $\varepsilon \approx 1\ J/(s \cdot kg)$. For model B: $\tau \approx 1.3 \times 10^{-3} s$, $\eta \approx 63\ \mu m$ and $\varepsilon \approx 0.64\ J/(s \cdot kg)$. Model B therefore displayed a lower dissipation rate, despite the smaller characteristic length scale, implying a comparatively larger reduction in the fluctuation velocities within the aneurysm sac. This was supported by the flow velocities and visualisations obtained through the 3D XPTV method. Both models displayed a significant reduction in flow velocity within the aneurysm sac, however model B displayed further deceleration prior to the aneurysm location due to a bifurcation in the parent artery, which resulted in lower velocities and a slower deceleration overall. This offers part of a possible explanation for the comparatively less chaotic flow patterns observed in model B versus model A. Model A displayed a jet like flow pattern, which is known to have a lower critical Reynolds number than conventional cylindrical pipe flows. Overall, using the parent artery Reynolds number in order to justify a laminar assumption

in numerical simulations appears far from ideal, as it potentially omits important aspects of the flow. Vortices were observed within the aneurysms, particularly for model A, and appeared to be highly localised. A definitive transition from a laminar flow regime could not be identified using the 3D-XPTV method, partly caused by the particles' poor ability to follow the flow which prevented PTV measurements at very low Re, and limitations on the number of particles tracked.

Both the critical Reynolds numbers and the location of the vortices were in line with DNS and CFD results obtained previously [31, 83].

Quantifying the flow in other ways using the acoustic method could be investigated in the future, e.g. by correlating properties of the power spectrum density to properties of the aneurysm, or by using several microphones to determine the location of fluctuations/vortices. With improved accuracy in the XPTV method further quantitative analysis could potentially be performed, e.g. Lagrangian spectral and autocorrelation analysis.

Appendix A

Acoustic Code

```
%Sample code for postprocessing of data files obtained using the acoustic
%method. in the data files column 1 contains time values. column 2 contains
%voltages

%sampling frequency
Fs=16384;
%load data file
data=load('datafile.lvm');
%separate the second column
data=data(:,2);
%cut off end points/choose the number of data points needed for analysis
data=data(100000:362143);
%welchs method with default values. 8 segments, 50% overlap, hamming window
[psi,freq]=pwelch(data,[],[],[],Fs); %if several trials psi can be averaged
%plotting
figure
loglog(freq,psi) %PSD
loglog(freq(700:5000),freq(700:5000).^-(7/3),'g') %-7/3 line for comparison
xlabel('Frequency(Hz)')
ylabel('Magnitude')
legend('Reynolds number','-7/3')
```

Appendix B

Photos of the models

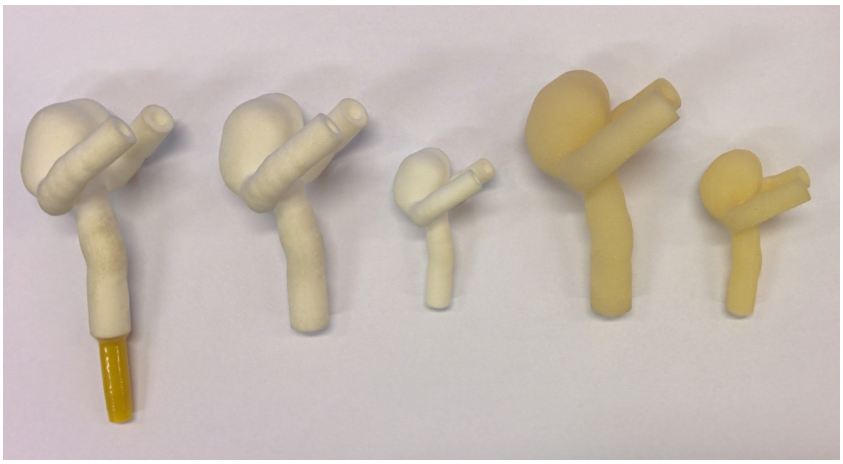

Figure B.1: Model A

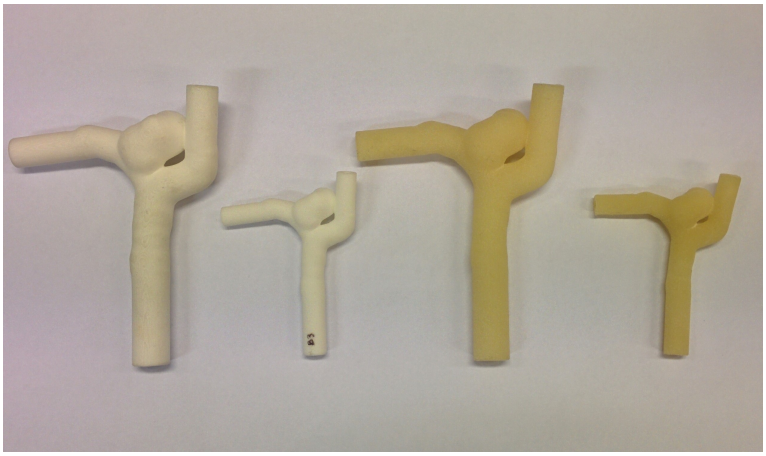

Figure B.2: Model B

B.1 Microphone positions

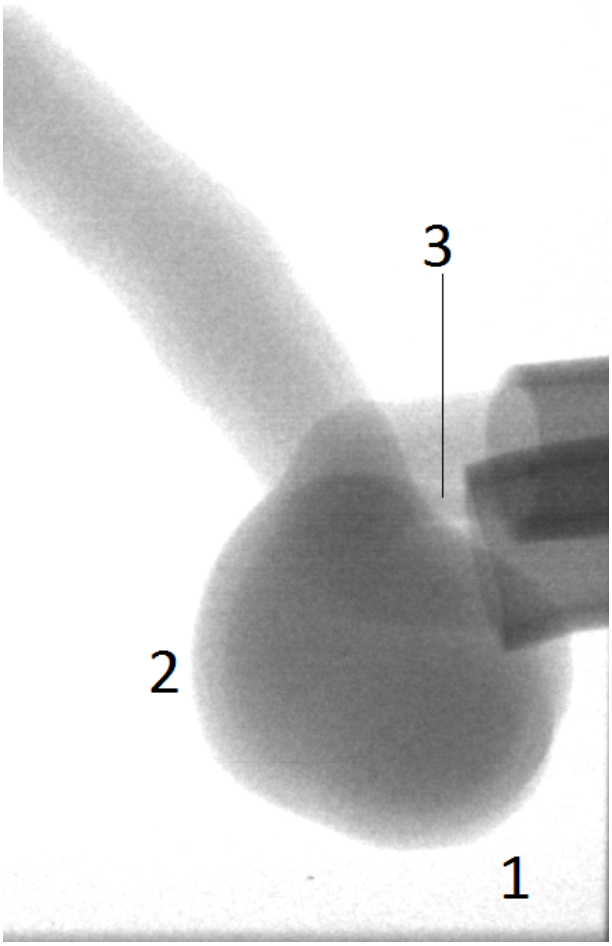

Figure B.3: Microphone positions

B.2 Connector types

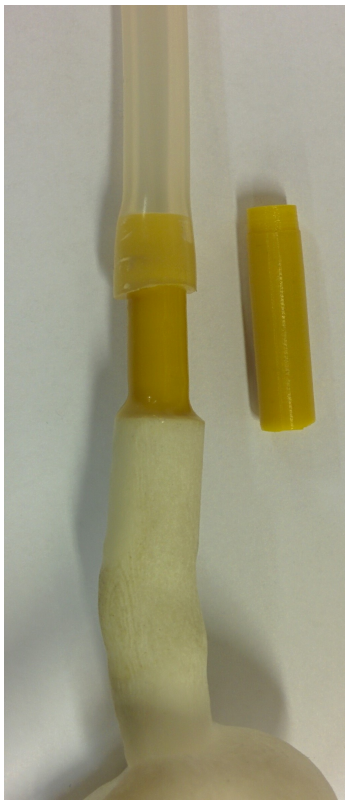

(a) Type 1: Thin, tapered 3D printed cylinder.

(b) Type 2: Large, tapered 3D printed cylinder.

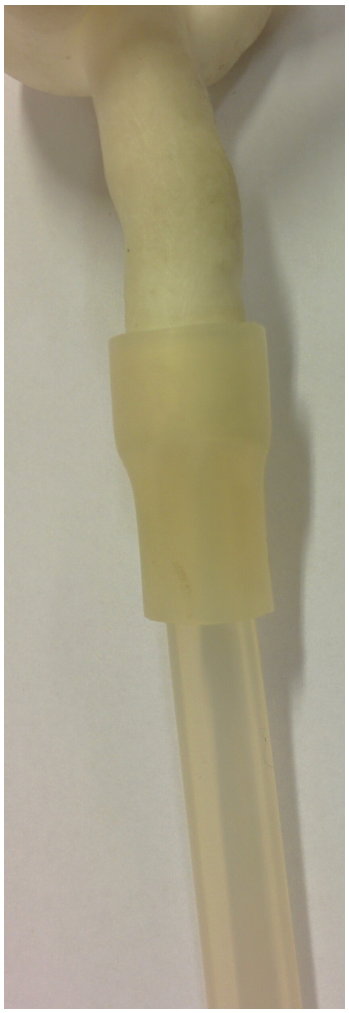

(c) Type 3: Tube only.

Figure B.4: The three types of connections investigated.

Appendix C

Labview

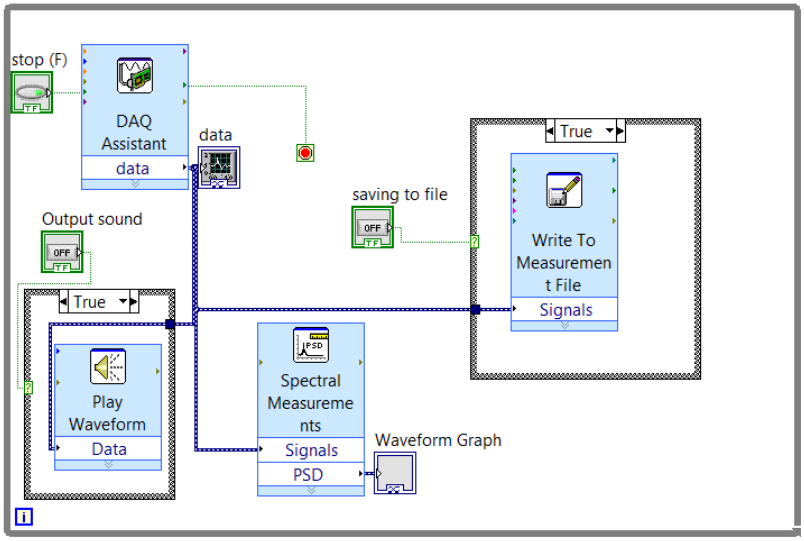

Figure C.1: Labview block diagram

Appendix D

PTV code

```
--------------------------------XPTV.m-------------------------------------
function [positions, adjacency_tracks, velocity, error]=XPTV(FolderLoc1,...
FolderLoc2, filterweak, plotpathonly, linkd, tracklength,syserror)

srcFiles1 = dir(strcat(FolderLoc1,'\*.jpg'));
srcFiles2 = dir(strcat(FolderLoc2,'\*.jpg'));
%series length
Num = length(srcFiles1);

%make the mean images
meanimage=MakeMeanImage(FolderLoc1);
meanimage_2=MakeMeanImage(FolderLoc2);

%pixel coordinates of where centreline xray hits the detector. assume
%perfectly centred
% for use in conversion to global coordinates. use pixel origin as upper
% left corner since that is what matlab uses
x0=864/2/2; %for 2x2 binning. remove one /2 for 1x1, add one /2 for 4x4
y0=1536/2/2; %these are in pixels

%detector plane coordinates
det1=-110; %y-coordinate in mm
det2=100; %z-coordinate in mm

%time step
%dt=1/155; %155 fps

%peak determination parameters
cam1int=9; %intensity threshold for binarisation chosen to ensure
cam2int=11; % the weakest blobs are picked up
blobsize=25; %minimum size of blobs to not be removed
peaksize1=15; %approx particle size when finding pos to pixel accuracy
peaksize2=10; %choose appropriately so peaks are found.
%implement a way of estimating the particle size before finding the peak?
peakintensity1=0.6; %intensity value of peaks after bpass filter is applied
```

```
peakintensity2=0.6; % choose appropriately to find peaks to pixel accuracy
cntsize1=5; %size parameter for finding particles to subpixel accuracy
cntsize2=5; %smaller than peaksize
cntbright1=21; %intensity value for filtering false peaks
cntbright2=21;

%predefine
poscam1=[];
poscam2=[];
%threedpos=[];
temp2=[];
temp3=[];
positions=cell(1,Num);
error=cell(1,Num);

%loop over images
for i=1:Num

%load images
imname = strcat(FolderLoc1,'\',srcFiles1(i).name);
image=double(imread(imname));
imname_2 = strcat(FolderLoc2,'\',srcFiles2(i).name);
image_2=double(imread(imname_2));

%subtract mean image
immean=image-meanimage;
immean_2=image_2-meanimage_2;

%binarise
imbw=(immean)>cam1int;
imbw_2=(immean_2)>cam2int;
%remove small binarised blobs that arent particles
imbw2=bwareaopen(imbw,blobsize);
imbw2_2=bwareaopen(imbw_2,blobsize);

%subpixel centroids can be found at this point using the built in
%matlab function regionprops. below uses code found online that gives a
%measure of the particle intensity which can be used for filtration of
%false particles that appear in some images (cam1 especially)

%bandpass filter. due to previous binarisation the primary purpose is
%to impose an artifical gradient on the blobs to allow for
%determination of sub pixel accuracy in the next step. makes blobs more
%realistic in shape as binarisation leaves/loses some unwanted pixels
%near the particle which messes up the shape and causes regionprops
%centroids to be less accurate (or so it seems)
imbp=bpass(imbw2,1,0); %1 indicates size of noise
imbp_2=bpass(imbw2_2,1,0);%0 indicates no further background subtraction
```

```
%find peaks to pixel accuracy
pk=pkfnd(imbp,peakintensity1,peaksize1);
pk_2=pkfnd(imbp_2,peakintensity2,peaksize2);

%subpixel accuracy
cnt=cntrd(imbp,pk,cntsize1);
cnt_2=cntrd(imbp_2,pk_2,cntsize2);
% OUTPUT:  an N x 4 array containing, x, y and brightness for each feature
%           cnt(:,1) is the x-coordinate
%           cnt(:,2) is the y-coordinate
%           cnt(:,3) is the brightness
%           cnt(:,4) is the square of the radius of gyration

%if no peaks are found then continue to the next image
if isempty(cnt) || isempty(cnt_2)
i
positions{i}=[-50,-50,-50]; %add a fake position far away from the
%rest that wont affect tracking.not needed?
continue
end
%     %if theres a different number of peaks in cnt and cnt_2 because of
%     %false peaks, or if some peaks have been lost this attempts to filter
%     %out false particle peaks based on brightness. need to be careful not
%     %to filter real particles. sometimes this works and sometimes it
%     doesnt. need a better filter based on positions. i.e. particle
%     positions either need to be near the inlet for new particles, or
%     within a certain distance of the old particle position.
if filterweak==1
if length(cnt(:,1))>length(cnt_2(:,1))
index=find(cnt(:,3)>cntbright1);
cnt=cnt(index,:);
end
if length(cnt(:,1))<length(cnt_2(:,1))
index=find(cnt_2(:,3)>cntbright2);
cnt_2=cnt_2(index,:);
end
end

%conversion to global coordinates
cnt(:,1)= cnt(:,1)-x0;
cnt(:,2)= y0-cnt(:,2);
cnt_2(:,1)= cnt_2(:,1)-x0;
cnt_2(:,2)= y0-cnt_2(:,2);

%conversion to mm
cnt(:,1)=cnt(:,1)*74.8*2/1000; %pixel size 74.8um. *2 for 2x2 binning
cnt(:,2)=cnt(:,2)*74.8*2/1000;
```

```
cnt_2(:,1)=cnt_2(:,1)*74.8*2/1000;
cnt_2(:,2)=cnt_2(:,2)*74.8*2/1000;

%add missing coordinate for 3D (detector plane coordinate)
poscam1(:,1)=cnt(:,1); %x-coordinate
poscam1(:,2)=det1; %y-coordinate (detector plane for detector 1)
poscam1(:,3)=cnt(:,2); %z-coordinate
poscam2(:,1)=cnt_2(:,1); %x-coordinate
poscam2(:,2)=cnt_2(:,2); %y-coordinate
poscam2(:,3)=det2;       %z-coordinate(detector plane for detector 2)

dist=[];
pos=cell(length(poscam1(:,1)),length(poscam2(:,1)));
%use NearestPoint.m to find 3d positions. in order to match particles
%correctly all combinations are tested and the minimums determined
for k=1:length(poscam1(:,1))
for l=1:length(poscam2(:,1))
temp=NearestPoint(poscam1(k,:),poscam2(l,:),0); %temp = [P,d]
%save distance in a matrix                        , P= [x y z]
dist(k,l)=temp(4);
%save 3d position in a matrix
pos{k,l}=temp(1:3);
end
end
%find the index of the minimum distance for each particle
%use the index to find the correct 3d pos for each particle
for m=1:length(dist(:,1))
index=find(abs(dist-syserror)==min(abs(dist(m,:)-syserror)));
%index of which particle pair had the minimum distance based on the
%comparisons made with particle m
%1.6 systematic error? compare with this instead of minimum
%need a better way of doing this. should compare all particles at
%the same time and choose the best overall fit. (similar to
%transient tracking of particles)

%store everything in one matrix [x,y,z,time(frame# track.m),distance]
%threedpos(size(threedpos,1)+1,:)=[pos{index},(i-1),dist(index)];
%track.m doesnt work. possibly because of negative coordinates

%try another tracking script: simpletracker.m
%need to save positions at each time step as a matrix
temp2(m,:)=pos{index};
temp3(m,:)=dist(index);
end

%then save the matrixes for each time step in in a cell
positions{i}=temp2;
error{i}=temp3;
```

```
%reset
temp2=[];
temp3=[];
poscam1=[];
poscam2=[];
end

%track particles from time step to time step
[tracks adjacency_tracks] = simpletracker(positions,'MaxLinkingDistance'...
,linkd,'MaxGapClosing',3);
%use the tracked particles to isolate the track positions
index=find(cellfun('length', adjacency_tracks)>tracklength);

all_points = vertcat(positions{:});
%colors = hsv(numel(tracks));
velocity=cell(1,numel(index));

count=1;
%loop over the track for each particle (from simpletracker package)
for i_track = index'

% We use the adjacency tracks to retrieve the points coordinates. It
% saves us a loop.
track = adjacency_tracks{i_track};
track_points = all_points(track, :);
figure(1)
hold on
velocity{count}=velocityandplot(track_points);

if plotpathonly==1
figure(2)
hold on
plot3(track_points(:,1),track_points(:,3), track_points(:, 2))
limits=[-40 40 0 50 -40 30]; %model a
view(-128,14) %model a
%limits=[-40 40 -20 35 -40 30]; %model b
%view(-37,18)                    %model b
axis(limits)
xlabel('x (mm)')
ylabel('z (mm)')
zlabel('y (mm)')
end
count=count+1;

end
```

----------velocityandplot.m----------

```
function [velocity]=velocityandplot(threedpos)

%plot pathline with colour depending on velocity

%how far does the particle move
a=length(threedpos(:,1));
dist=zeros(1,a);
for j=1:a-1
%compare particle with old position
dist(j+1)=((threedpos(j+1,1)-threedpos(j,1))^2 +...
(threedpos(j+1,2)-threedpos(j,2))^2+(threedpos(j+1,3)...
-threedpos(j,3))^2)^0.5;
end
dist=dist';
%calculate velocity
velocity=dist*155; %mm/s. for m/s divide by 1000
velocity(1)=velocity(2);

maxvel=max(velocity)
minvel=min(velocity)
meanvel=mean(velocity)

x = threedpos(:,1);
y = threedpos(:,2);
z = threedpos(:,3);
c = velocity;      %# colors

%note: to make it look right in matlab switch y and z coordinates but label
%the axis correspondingly
h = surface([x(:), x(:)], [z(:), z(:)], [y(:), y(:)], ...
[c(:), c(:)], 'EdgeColor','interp', 'FaceColor','none');%,'linew',2
colormap( jet(numel(velocity)) )

limits=[-40 40 0 50 -40 30];   %model a
view(-128,14) %view(-48,16)    %model a
%limits=[-40 40 -20 35 -40 30]; %model b
%view(-37,18)                    %model b
axis(limits)
xlabel('x (mm)')
ylabel('z (mm)')
zlabel('y (mm)')
col = colorbar;
col.Label.String = 'Velocity (mm/s)';
%title('Re ~1600')

% saveas(h,'3D.jpg')
% view(0,90)
% saveas(h,'x-zplane.jpg')
```

```
% view(0,0)
% saveas(h, 'x-yplane.jpg')

%figure(2)
%movie
% for k=1:a
%   clf
%   fig=plot3(x(1:k),z(1:k),y(1:k))
%
%  h = surface([x(1:k), x(1:k)], [z(1:k), z(1:k)], [y(1:k), y(1:k)], ...
%     [c(1:k), c(1:k)], 'EdgeColor','flat', 'FaceColor','none');
%   colormap(jet(numel(velocity)));
%   caxis([0 200]) %choose velocity range to ensure colours arent scaled
%   xlabel('x (mm)')
%   ylabel('z (mm)')
%   zlabel('y (mm)')
%   title('Re ~1600')
%   view(48,-16)
%   axis(limits)
%
%   saveas(fig,['savedfigs/test',num2str(k),'.jpg']) %or save h
%
% end

end

------------------------nearestpoint.m---------------------------------------
function out=NearestPoint(m1,m2,plot)
%given two detected particle coordinates m1,m2 in global coordinates (mm)
%format:
%m1 = [x,-110,z] %y coordinate dependent on detector plane
%m2 = [x,y,100]; %z coordinate dependent on detector plane
%rewrite so this function does all conversion and adds the detector
%plane???

%source coordinates are defined here
s1 = [0,526,0];     %x-ray source 1
s2 = [0,0,-442];    %x-ray source 2
%plot can either be 1 or 0 for plotting or no plotting of the rays
%if plotting open a figure in the main program before calling this function
% and put hold on if you want several plots on the same figure before
% calling this function repeatedly with different points

%calculate nearest point on the lines to the other line
%(use dot product method instead????faster???)
U=m1-s1;
V=m2-s2;
W=cross(U,V);
```

```
P1=s1 + dot(cross(s2-s1,V),W)/dot(W,W)*U; %point on line s1m1
P2=s2 + dot(cross(s2-s1,U),W)/dot(W,W)*V; %point on line s2m2
d=norm(P2-P1); %distance between the points.

%use midpoint between the closest points on the lines as actual position
P=(P1+P2)/2;

out=[P,d];

if plot==1
pts = [s1; m1];
pts2 = [s2; m2];
plot3(pts(:,1), pts(:,3), pts(:,2))
hold on
plot3(pts2(:,1), pts2(:,3), pts2(:,2))

end
end

---------------MakeMeanImage.m-----------------------------------------
function out=MakeMeanImage(FolderName)

%series length
srcFiles = dir(strcat(FolderName,'\*.jpg'));
Num = length(srcFiles);

%add images
for i=1:Num

imname = strcat(FolderName,'\',srcFiles(i).name);

image=double(imread(imname));
if i==1
A=image;
else
A=A+image;
end
end
%find average
out=A/(Num);

%invert if not already done
%out=imcomplement(out);
end
```

Bibliography

[1] Taha M Alkhamis, Richard L Beissinger, and Juan R Chediak. "Red Blood Cell Effect on Platelet Adhesion and Aggregation in Low-Stress Shear Flow: Myth or Fact?." In: *ASAIO Journal* 34.3 (1988), pp. 868–873.

[2] Luca Antiga and David A Steinman. "Rethinking turbulence in blood". In: *Biorheology* 46.2 (2009), pp. 77–81.

[3] Elizabeth Antoine et al. "Flow measurements in a blood-perfused collagen vessel using X-ray micro-particle image velocimetry". In: *PloS one* 8.11 (2013), e81198.

[4] Charles F Babbs. "The origin of Korotkoff sounds and the accuracy of auscultatory blood pressure measurements". In: *Journal of the American Society of Hypertension* 9.12 (2015), pp. 935–950.

[5] GK Batchelor. "Pressure fluctuations in isotropic turbulence". In: *Mathematical Proceedings of the Cambridge Philosophical Society*. Vol. 47. 02. Cambridge Univ Press. 1951, pp. 359–374.

[6] Katherine Benson. "MCAT review". In: *Emory University* (1999).

[7] SA Berger, L Talbot, and LS Yao. "Flow in curved pipes". In: *Annual review of fluid mechanics* 15.1 (1983), pp. 461–512.

[8] Daniel Blair and Eric Dufresne. *The Matlab Particle Tracking Code Repository*. URL: `http://site.physics.georgetown.edu/matlab/index.html`.

[9] D Bluestein et al. "Steady flow in an aneurysm model: correlation between fluid dynamics and blood platelet deposition". In: *Journal of biomechanical engineering* 118.3 (1996), pp. 280–286.

[10] Nathan J de Boer, Simone FC Knaap, and Annemarie de Zoete. "Clinical detection of abdominal aortic aneurysm in a 74-year-old man in chiropractic practice". In: *Journal of chiropractic medicine* 9.1 (2010), pp. 38–41.

[11] Sebastian Burgmann et al. "Analysis of tracer particle characteristics for micro PIV in wall-bounded gas flows". In: *La houille blanche* 4 (2011), pp. 55–61.

[12] Flow Capture. *REX-CELL XPTV 2014-15*. 2015. URL: `http://www.flowcapture.com/rexcellxptv.html`.

[13] Samjin Choi and Zhongwei Jiang. "Cardiac sound murmurs classification with autoregressive spectral analysis and multi-support vector machine technique". In: *Computers in biology and medicine* 40.1 (2010), pp. 8–20.

[14] Vivian L Clark and James A Kruse. *Clinical methods: the history, physical, and laboratory examinations*. Vol. 264. 21. American Medical Association, 1990, pp. 2808–2809.

[15] Wikimedia Commons. *CPT-sound-nyquist-thereom-1.5percycle.svg*. 2012. URL: https://commons.wikimedia.org/wiki/File:CPT-sound-nyquist-thereom-1.5percycle.svg.

[16] Clayton T Crowe et al. *Multiphase flows with droplets and particles*. CRC press, 2011.

[17] Peter F Davies et al. "Turbulent fluid shear stress induces vascular endothelial cell turnover in vitro". In: *Proceedings of the National Academy of Sciences* 83.7 (1986), pp. 2114–2117.

[18] SJ Dhawan and R Narasimha. "Some properties of boundary layer flow during the transition from laminar to turbulent motion". In: *Journal of Fluid Mechanics* 3.04 (1958), pp. 418–436.

[19] Edward Raymond Doering. "Three-dimensional flaw reconstruction using a real-time X-ray imaging system". In: (1992).

[20] Bruno Eckhardt et al. "Turbulence transition in pipe flow". In: *Annu. Rev. Fluid Mech.* 39 (2007), pp. 447–468.

[21] Gary G Ferguson. "Turbulence in human intracranial saccular aneurysms". In: *Journal of neurosurgery* 33.5 (1970), pp. 485–497.

[22] Matthew D Ford et al. "PIV-measured versus CFD-predicted flow dynamics in anatomically realistic cerebral aneurysm models". In: *Journal of biomechanical engineering* 130.2 (2008), p. 021015.

[23] Andreas Fouras et al. "The past, present, and future of x-ray technology for in vivo imaging of function and form". In: *Journal of Applied Physics* 105.10 (2009), p. 102009.

[24] Yuan-cheng Fung. *Biomechanics: circulation*. Springer Science & Business Media, 2013.

[25] William K George. "Lectures in Turbulence for the 21st Century". In: *Chalmers University of Technology* (2009).

[26] William K George, Paul D Beuther, and Roger EA Arndt. "Pressure spectra in turbulent free shear flows". In: *Journal of Fluid Mechanics* 148 (1984), pp. 155–191.

[27] Monson H Hayes. *Statistical digital signal processing and modeling John Wiley & Sons*. 1996.

[28] Theodore J Heindel. "A review of X-ray flow visualization with applications to multiphase flows". In: *Journal of Fluids Engineering* 133.7 (2011), p. 074001.

[29] Theodore J Heindel, Joseph N Gray, and Terrence C Jensen. "An X-ray system for visualizing fluid flows". In: *Flow Measurement and Instrumentation* 19.2 (2008), pp. 67–78.

[30] Yiemeng Hoi et al. "Validation of CFD simulations of cerebral aneurysms with implication of geometric variations". In: *Journal of biomechanical engineering* 128.6 (2006), pp. 844–851.

[31] Kartik Jain, Sabine Roller, and Kent-André Mardal. "Transitional flow in intracranial aneurysms–A space and time refinement study below the Kolmogorov scales using Lattice Boltzmann Method". In: *Computers and Fluids* 127 (2016), pp. 36–46.

[32] Sung Yong Jung et al. "In vivo measurements of blood flow in a rat using X-ray imaging technique". In: *The international journal of cardiovascular imaging* 28.8 (2012), pp. 1853–1858.

[33] Daniel Juvé, Marion Berton, and Edouard Salze. "Spectral Properties of Wall-Pressure Fluctuations and Their Estimation from Computational Fluid Dynamics". In: *Flinovia-Flow Induced Noise and Vibration Issues and Aspects*. Springer, 2015, pp. 27–46.

[34] Athanasia Kalpakli. "Experimental study of turbulent flows through pipe bends". In: (2012).

[35] HT Kim, SJ Kline, and WC Reynolds. "The production of turbulence near a smooth wall in a turbulent boundary layer". In: *J. Fluid Mech* 50.1 (1971), pp. 133–160.

[36] John Kim. "On the structure of pressure fluctuations in simulated turbulent channel flow". In: *Journal of Fluid Mechanics* 205 (1989), pp. 421–451.

[37] NS Korotkoff. "On methods of studying blood pressure". In: *Bull Imperial Mil Med Acad* 11 (1905), pp. 365–367.

[38] David N Ku. "Blood flow in arteries". In: *Annual Review of Fluid Mechanics* 29.1 (1997), pp. 399–434.

[39] Yasushi Kurokawa, Seisho Abiko, and Kohsaku Watanabe. "Noninvasive detection of intracranial vascular lesions by recording blood flow sounds." In: *Stroke* 25.2 (1994), pp. 397–402.

[40] Robert S Lees. "Phonoangiography: qualitative and quantitative". In: *Annals of biomedical engineering* 12.1 (1984), pp. 55–62.

[41] Robert S Lees and C Forbes Dewey. "Phonoangiography: a new noninvasive diagnostic method for studying arterial disease". In: *Proceedings of the National Academy of Sciences* 67.2 (1970), pp. 935–942.

[42] Ren-Chieh Lien, ERIC A D'ASARO, and Geoffrey T Dairiki. "Lagrangian frequency spectra of vertical velocity and vorticity in high-Reynolds-number oceanic turbulence". In: *Journal of Fluid Mechanics* 362 (1998), pp. 177–198.

[43] Michael J Lighthill. "On sound generated aerodynamically. I. General theory". In: *Proceedings of the Royal Society of London A: Mathematical, Physical and Engineering Sciences*. Vol. 211. 1107. The Royal Society. 1952, pp. 564–587.

[44] Michael James Lighthill. "On sound generated aerodynamically. II. Turbulence as a source of sound". In: *Proceedings of the Royal Society of London A: Mathematical, Physical and Engineering Sciences*. Vol. 222. 1148. The Royal Society. 1954, pp. 1–32.

[45] P Worth Longest and Clement Kleinstreuer. "Comparison of blood particle deposition models for non-parallel flow domains". In: *Journal of Biomechanics* 36.3 (2003), pp. 421–430.

[46] P Worth Longest and Clement Kleinstreuer. "Particle-hemodynamics modeling of the distal end-to-side femoral bypass: effects of graft caliber and graft-end cut". In: *Medical engineering & physics* 25.10 (2003), pp. 843–858.

[47] A Mahabuba, J Vijay Ramnath, and G Anil. "Analysis of heart sounds and cardiac murmurs for detecting cardiac disorders using phonocardiography". In: *Journal of the Instrumentation Society of India* 39 (2009), pp. 38–41.

[48] Graeme McRae. *Equation of Lines in 3D - distance between two skew lines, and closest points.* URL: `http://2000clicks.com/mathhelp/GeometryPointsAndLines3D.aspx`.

[49] A Melling. "Tracer particles and seeding for particle image velocimetry". In: *Measurement Science and Technology* 8.12 (1997), p. 1406.

[50] Lewis F Moody. "Friction factors for pipe flow". In: *Trans. Asme* 66.8 (1944), pp. 671–684.

[51] Umberto Morbiducci et al. "Mechanistic insight into the physiological relevance of helical blood flow in the human aorta: an in vivo study". In: *Biomechanics and modeling in mechanobiology* 10.3 (2011), pp. 339–355.

[52] N Mordant et al. "Lagrangian velocity fluctuations in fully developed turbulence: scaling, intermittency, and dynamics". In: *Journal of Statistical Physics* 113.5-6 (2003), pp. 701–717.

[53] Carlos Gavilán Moreno. *Turbulence, Vibrations, Noise and Fluid Instabilities. Practical Approach.* INTECH Open Access Publisher, 2010.

[54] Timothy B Morgan et al. "A high-speed X-ray detector system for noninvasive fluid flow measurements". In: *ASME 2013 Fluids Engineering Division Summer Meeting.* American Society of Mechanical Engineers. 2013, V01CT24A004–V01CT24A004.

[55] Khandakar Niaz Morshed et al. "Theory to Predict Shear Stress on Cells in Turbulent Blood Flow". In: *PloS one* 9.8 (2014), e105357.

[56] K Naugolnykh and L Ostrovsky. *Nonlinear wave processes in acoustics.* Cambridge University Press, 1998.

[57] Henry G Nepomuceno and Richard M Lueptow. "Pressure and shear stress measurements at the wall in a turbulent boundary layer on a cylinder". In: *Physics of Fluids (1994-present)* 9.9 (1997), pp. 2732–2739.

[58] Hanwook Park et al. "Measurement of real pulsatile blood flow using X-ray PIV technique with CO2 microbubbles". In: *Scientific reports* 5 (2015).

[59] J Peacock et al. "The onset of turbulence in physiological pulsatile flow in a straight tube". In: *Experiments in fluids* 24.1 (1998), pp. 1–9.

[60] Stephen B Pope. *Turbulent flows.* 2001.

[61] K Narahari Rao, R Narasimha, and MA Badri Narayanan. "The 'bursting' phenomenon in a turbulent boundary layer". In: *Journal of Fluid Mechanics* 48.02 (1971), pp. 339–352.

[62] Margot R Roach, Susan Scott, and Gary G Ferguson. "The hemodynamic importance of the geometry of bifurcations in the circle of Willis (glass model studies)". In: *Stroke* 3.3 (1972), pp. 255–267.

[63] Bianca Rocca and Garret A FitzGerald. "Simply Read: Erythrocytes Modulate Platelet Function Should We Rethink the Way We Give Aspirin?" In: *Circulation* 95.1 (1997), pp. 11–13.

[64] Todd D Rozen and Douglas Quint. "Unilateral orbital bruit in an adolescent with daily persistent headache". In: *Headache: The Journal of Head and Face Pain* 46.2 (2006), pp. 335–336.

[65] Chander Sadasivan et al. "Physical factors effecting cerebral aneurysm pathophysiology". In: *Annals of biomedical engineering* 41.7 (2013), pp. 1347–1365.

[66] Gary E Saito and Terry J Vander Werff. "The importance of viscoelasticity in arterial blood flow models". In: *Journal of biomechanics* 8.3 (1975), pp. 237–245.

[67] Ronald W Schafer. "What is a Savitzky-Golay filter?[lecture notes]". In: *Signal Processing Magazine, IEEE* 28.4 (2011), pp. 111–117.

[68] GB Schubauer. "Laminar boundary-layer oscillations and stability of laminar flow". In: *Journal of the Aeronautical Sciences* (1947).

[69] A Seeger et al. "Assessment of flow structures in bubble columns by X-ray based particle tracking velocimetry". In: *4th International Symposium on Particle Image Velocimetry, Gottingen, Germany*. 2001.

[70] Jung Hee Seo and Rajat Mittal. "A coupled flow-acoustic computational study of bruits from a modeled stenosed artery". In: *Medical & biological engineering & computing* 50.10 (2012), pp. 1025–1035.

[71] Daniel M Sforza, Christopher M Putman, and Juan Raul Cebral. "Hemodynamics of cerebral aneurysms". In: *Annual review of fluid mechanics* 41 (2009), p. 91.

[72] Otis M Solomon Jr. *PSD computations using Welch's method.[Power Spectral Density (PSD)]*. Tech. rep. Sandia National Labs., Albuquerque, NM (United States), 1991.

[73] Volker Springel. "High performance computing and numerical modelling". In: *Star Formation in Galaxy Evolution: Connecting Numerical Models to Reality*. Springer, 2016, pp. 251–358.

[74] Robert Stafford. *Intersection of two straight lines in 3D space*. 2009. URL: `https://se.mathworks.com/matlabcentral/newsreader/view_thread/246420`.

[75] Paul D Stein and Hani N Sabbah. "Turbulent blood flow in the ascending aorta of humans with normal and diseased aortic valves." In: *Circulation research* 39.1 (1976), pp. 58–65.

[76] Dan Sunday. *Distance between 3D lines and segments*. 2012. URL: `http://geomalgorithms.com/a07-_distance.html`.

[77] J Kristian Sveen and Edwin A Cowen. "Quantitative imaging techniques and their application to wavy flows". In: *Advances in Coastal and Ocean Engineering* 9 (2004), p. 1.

[78] George B Thurston. "Viscoelasticity of human blood". In: *Biophysical journal* 12.9 (1972), p. 1205.

[79] Jean-Yves Tinevez. *Simple Tracker*. 2016. URL: `http://www.mathworks.com/matlabcentral/fileexchange/34040-simple-tracker`.

[80] Khanh Tuoc Trinh. "On the critical Reynolds number for transition from laminar to turbulent flow". In: *arXiv preprint arXiv:1007.0810* (2010).

[81] Cameron Tropea, Alexander L Yarin, and John F Foss. *Springer handbook of experimental fluid mechanics*. Vol. 1. Springer Science & Business Media, 2007.

[82] International Study of Unruptured Intracranial Aneurysms Investigators et al. "Unruptured intracranial aneurysms: risk of rupture and risks of surgical intervention". In: *N Engl J Med* 339 (1998), pp. 1725–1733.

[83] Kristian Valen-Sendstad, Kent-André Mardal, and David A Steinman. "High-resolution CFD detects high-frequency velocity fluctuations in bifurcation, but not sidewall, aneurysms". In: *Journal of biomechanics* 46.2 (2013), pp. 402–407.

[84] Charles Van Loan. *Computational frameworks for the fast Fourier transform*. Vol. 10. Siam, 1992.

[85] BCH Verbiest. "Thrombus formation in aneurysms: An experimental study". In: *Division of Cardiovascular Biomechanics, Eindhoven University of Technology, MSc thesis* (2008).

[86] Peter D Welch. "The use of fast Fourier transform for the estimation of power spectra: A method based on time averaging over short, modified periodograms". In: *IEEE Transactions on audio and electroacoustics* 15.2 (1967), pp. 70–73.

[87] Frank M White and Isla Corfield. *Viscous fluid flow*. Vol. 3. McGraw-Hill New York, 2006.

[88] JE Ffowcs Williams. "Hydrodynamic noise". In: *Annual Review of Fluid Mechanics* 1.1 (1969), pp. 197–222.

[89] J Xu, LG Durand, and P Pibarot. "A new, simple, and accurate method for non-invasive estimation of pulmonary arterial pressure". In: *Heart* 88.1 (2002), pp. 76–80.

[90] Lily Xu. "Lyden av turbulens". Master's Thesis. University of Oslo, 2015.

[91] Takanobu Yagi et al. "Experimental insights into flow impingement in cerebral aneurysm by stereoscopic particle image velocimetry: transition from a laminar regime". In: *Journal of The Royal Society Interface* 10.82 (2013), p. 20121031.